UNIVERSIDAD NACIONAL DEL LITORAL

Fluid Structure Interaction using an Arbitrary Lagrangian Eulerian Formulation

Luciano Garelli

FICH
FACULTAD DE INGENIERIA
Y CIENCIAS HIDRICAS

INTEC
INSTITUTO DE DESARROLLO TECNOLOGICO
PARA LA INDUSTRIA QUIMICA

Tesis de Doctorado **2011**

FLUID STRUCTURE INTERACTION USING AN ARBITRARY LAGRANGIAN EULERIAN FORMULATION

by

Luciano Garelli

Dissertation submitted to the Postgraduate Department of the

FACULTAD DE INGENIERÍA Y CIENCIAS HÍDRICAS

of the

UNIVERSIDAD NACIONAL DEL LITORAL

in partial fulfillment of the requirements for the degree of

Doctor en Ingeniería - Mención Mecánica Computacional

2011

Author Legal Declaration

This dissertation have been submitted to the Postgraduate Department of the *Facultad de Ingeniería y Ciencias Hídricas* in partial fulfillment of the requirements the degree of *Doctor en Ingeniería - Mención Mecánica Computacional* of the *Universidad Nacional del Litoral*. A copy of this document will be available at the University Library and it will be subjected to the Library's legal normative. Some parts of the work presented in this thesis have been published in the following journals: Computer & Fluids, International Journal for Numerical Methods in Fluids and Computer Methods in Biomechanics and Biomedical Engineering.

Luciano Garelli

A la memoria de mis abuelos
Enrique y Rubén.

FLUID STRUCTURE INTERACTION USING AN ARBITRARY LAGRANGIAN EULERIAN FORMULATION

Thesis advisors:

Mario A. Storti	INTEC (CONICET-UNL)
	Facultad de Ingeniería y Ciencias Hídricas - UNL
Rodrigo R. Paz	INTEC (CONICET-UNL)
	Facultad de Ingeniería y Ciencias Hídricas - UNL

Evaluation committee members:

Dra. Marcela Cruchaga	Universidad de Santiago de Chile.
Dr. Carlos Sacco	Instituto Universitario Aeronáutico.
Dr. Axel Larreteguy	Universidad Argentina de la Empresa.
Dr. Sergio Idelsohn	INTEC (CONICET-UNL)
	Facultad de Ingeniería y Ciencias Hídricas-UNL.

FACULTAD DE INGENIERÍA Y CIENCIAS HÍDRICAS

UNIVERSIDAD NACIONAL DEL LITORAL

2011

Acknowledgements

This thesis has received financial support from *Consejo Nacional de Investigaciones Científicas y Técnicas* (CONICET), *Universidad Nacional del Litoral* (UNL), and *Agencia Nacional de Promoción Científica y Tecnológica* (ANPCyT). The research work was carried out at the *Centro Internacional de Métodos Computacionales en Ingeniería* (CIMEC) of the *Instituto de Desarrollo Tecnológico para la Industria Química* (INTEC), dependent of UNL and CONICET.

Abstract

Multidisciplinary and Multiphysics coupled problems represent nowadays a challenging field when studying even more complex phenomena that appear in nature and in new technologies (e.g. Magneto-Hydrodynamics, Micro-Electro-Mechanics, Thermo-Mechanics, Fluid-Structure Interaction, etc.). Particularly, when dealing with Fluid-Structure Interaction problems several questions arise, namely the coupling algorithm, the mesh moving strategy, the Galilean Invariance of the scheme, the compliance with the Discrete Geometric Conservation Law (DGCL), etc. Therefore, the aim of this thesis is the development and implementation of a coupling algorithm for existing modules or subsystems, in order to carry out FSI simulations with the focus on distributed memory parallel platforms. Regarding the coupling techniques, some results on the convergence of the strong coupling Gauss-Seidel iteration are presented. Also, the precision of different predictor schemes for the structural system and the influence of the partitioned coupling on stability are discussed. Another key point when solving FSI problems is the use of the ''Arbitrary Lagrangian Eulerian formulation'' (ALE), which allows the use of moving meshes. As the ALE contributions affect the advective terms, some modifications on the stabilizing and the shock-capturing terms, are needed. Also, the movements of the fluid mesh produces a volume change in time of the elements, which adds to the fluid formulation an extra conservation law to be satisfied. The law is known as the Discrete Geometric Conservation Law (DGCL). In this thesis a new and original methodology for developing DGCL compliant formulations based on an Averaged ALE Jacobians Formulation (AJF) is presented.

Contents

List of Abbreviations

AAA: Abdominal Aortic Aneurysm.
AJF: Averaged Jacobians Formulation.
ALE: Arbitrary Lagrangian Eulerian.
BDF: Backward Differential Formula.
BE: Backward Euler time integration method ($\theta = 1$).
CFD: Computational Fluid Dynamics.
CN: Crank-Nicolson time integration method ($\theta = 0.5$).
CSD: Computational Structural Dynamics.
DGCL: Discrete Geometric Conservation Law.
FDM: Finite Difference Method.
FEM: Finite Element Method.
FSI: Fluid Structure Interaction.
FVM: Finite Volume Method.
GA: Galerking time integration method ($\theta = 2/3$).
GCL: Geometric Conservation Law.
GDD: Glaucoma Drainage Device.
IOP: Intraocular Pressure.
MPI: Message Passing Interface.
NS: Navier-Stokes equations.
OOP: Object Oriented Programming.
PETSc: Portable, Extensible Toolkit for Scientific Computation.
SC: Shock capturing.
SUPG: Streamline Upwind Petrov-Galerkin.

List of Symbols

a_s: discrete structure acceleration.

c: speed of sound.

c_s: solid wave speed Cp: pressure coefficient.

C_v: specific heat at constant volume.

d_s: discrete structure displacement.

D: damping matrix.

e: specific internal energy.

E: total specific internal energy.

E_s: structure energy.

E: modulus of elasticity.

$\bar{\bar{\mathcal{E}}}$: Green-Lagrange strain tensor.

d_0: Amplitude of the motion of the internal cylinder.

$\bar{\bar{F}}$: deformation gradient tensor.

$\mathcal{F}^c$: convective fluxes.

$\mathcal{F}^d$: diffusive fluxes.

g_k: averaged interpolation function gradient.

h: specific enthalpy.

h: element size.

h_j: characteristic element length.

H: total specific enthalpy.

$\bar{\bar{I}}$: Kronecker isotropic tensor of rank 2.

J: Jacobian of the transformation.

K: stiffness matrix.

m: dimension of the state vector.

M: mass matrix.

n: number of integration points.
n_d: number of spatial dimensions.
n_{el}: total number of elements.
n_k: k-th component of the unit normal vector.
p: pressure.
p_{ref}: reference pressure.
$\mathcal{P}_a$: perturbation funtion.
$\widetilde{\mathcal{P}}_a$: transformed perturbation funtion.
$\bar{\bar{P}}$: first Piola-Kirchhoff stress tensor.
R_1: Radius of the internal cylinder.
R_2: Radius of the external cylinder.
s: order of the polynomial used to represent the time evolution of the nodal displacement.
$\bar{\bar{S}}$: second Piola-Kirchhoff stress tensor.
t: time.
T: absolute temperature.
T_0: reference temperature.
u: scalar field.
$\mathbf{u}$: velocity vector.
$\mathbf{U}$: state vector.
U_j: j-th component of state vector.
v_k^*: k-th component of the mesh velocity.
$\mathbf{v}_s$: discrete structure velocity.
$\mathbf{x}$: fluid mesh node positions.
w: weighting function.
w_{fs}: frequency of the coupled system.
$\mathbf{w}$: fluid state vector.
$\mathbf{z}$: structure displacement.
α_0: predictor parameter.
α_1: predictor parameter.
$\boldsymbol{\beta}$: viscous τ_d parameter.
β_n: Newmark parameter.
δ_{SC}: shock capturing parameter.

Δ: Laplacian operator.
Δt: time step.
$\varepsilon_{ij}(\mathbf{u})$: strain rate tensor.
γ_n: Newmark parameter.
γ: ratio of specific heats.
Γ^t: boundary of the domain.
$\Gamma_{f/s}$: interface between the fluid and the structure.
λ: Stoke's hypothesis for stresses.
λ_s: Lamé constant.
μ: dynamic viscosity.
μ_0: dynamic viscosity for a reference temperature.
μ_s: Lamé constant.
ω: angular frequency.
Ω: spatial domain.
Ω_s: structure domain.
Ω^t: time-dependent domain.
Ω_k^t: discrete fluid time-dependent domain.
Ω_{sk}^t: discrete structure domain.
Ω^ξ: reference domain.
θ: parameter of the trapezoidal time integrator.
$\boldsymbol{\xi}$: coordinate in the reference domain.
$\boldsymbol{\chi}(\boldsymbol{\xi}, t)$: map between the current domain and a reference domain.
ρ: density of the fluid.
ρ_s: density of the solid.
$\bar{\bar{\tau}}$: viscous stress tensor.
τ_{SUPG}: SUPG stabilization parameter.
κ: thermal conductivity.
∇: Nabla operator.
$\bar{\bar{\sigma}}_s$: Cauchy stress tensor.
ζ: mass ratio between the fluid and the structure.

List of Figures

List of Tables

Chapter 1

Introduction

This chapter is intended to provide an introduction to the Fluid-Structure Interaction (FSI) analyses, as well as the techniques, methodologies and algorithms used to perform the corresponding numerical simulations. Also, the motivations that acted as driving force for the execution of this research work are exposed, together with the scope and objectives of this thesis. Finally, the state of the art is reviewed and some related work are mentioned, to help the reader to understand the context of the present proposal.

1.1 Motivation

The interaction of a fluid with some movable or deformable structure has a historical and practical importance, and it has to be considered in the design of many engineering systems. In aeronautical or aerospace engineering, a high velocity and high pressure fluid flow can cause deformation of the structure, as can be seen in the sequence of images showed in Fig.(1.1), which were taken by NASA in 2010 during the liftoff of Space Shuttle. But, when the FSI is strong enough can produce the instability system, which is known as flutter and it can result in the failure of the structure or the system. In civil engineering the wind induced vibrations can cause the collapse of the construction, being the most studied example the Tacoma Narrows Bridge, which collapsed under 64 [km/h] wind conditions in November 7, 1940.

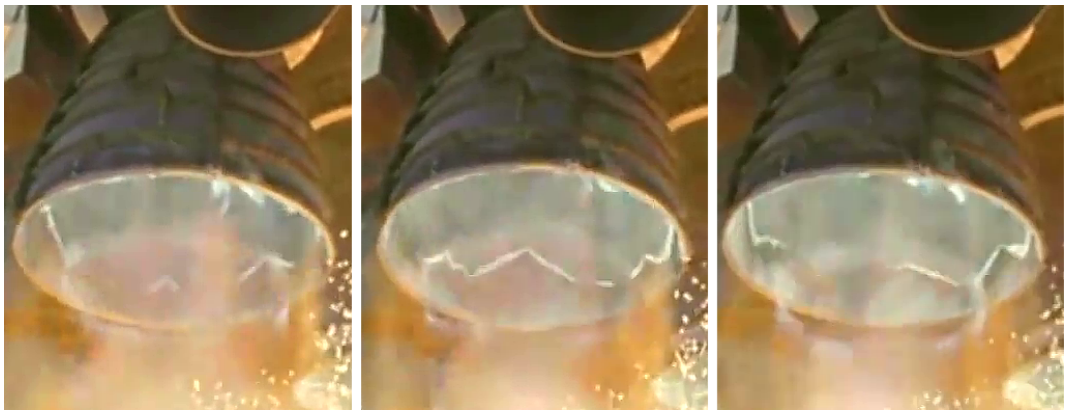

Figure 1.1: Space Shuttle Main Engine during start-up (NASA 2010).

Other important areas in which FSI plays a fundamental role are, for instance, in biomedical engineering, where the pulsating blood flow can cause the rupture of an abdominal aortic (AAA) or cerebral aneurysm, implying a great risk for the patient.

In the above mentioned cases it is very difficult to determine a priori the effects of the fluid over the structure, being these detected during the testing or use period. When the interaction is known to be strong enough to produce important deformation on the structure, intensives experimental tests are carried out. The setup process for an experimental test are time consuming due to the fact that it has to reproduce the flight conditions in the case of the wing flutter or the environmental condition in the case of a bridge and some cases are impossible to reproduce in a wind tunnel.

Figure 1.2: Collapse of the Tacoma Narrows Bridge (1940).

In this context is where the possibility to perform a numerical simulation of the whole system has a significant importance, allowing to test a wide number

of design parameters and having as result a detailed description of the fluid (velocities, pressure, turbulence intensity, etc.) and the structure (stress, strain, displacements, etc.). But, previous to perform any numerical simulation, a set of governing equations are needed. These equations describes the underlying physics and are generally expressed in terms of partial differential equations. On one hand there are the equations for the fluid, in general the Navier-Stokes (NS) equations (Batchelor, 1967; Acheson, 1990), and on the other hand there are the equations for the structure, derived from the general theory of elasticity (Timoshenko, 1970; Atkin and Fox, 2005). In some cases these equations are simplified with the use of models (e.g., turbulence models, wall functions, linear elastic material etc.) or hypothesis (e.g., incompressible fluid, inviscid fluid, small strain, etc.) in order to reduce the complexity of the equations to be solved.

These equations must be both spatially and temporally discretized using methods like as Finite Element (FEM), Finite Volume (FVM) or Finite Difference (FDM) and hence obtain a system of discrete equations to be solved in a computer or computer cluster. The numerical treatment of the fluid mechanics and elasticity equations are known as Computational Fluid Dynamics (CFD) and Computational Structural Dynamics (CSD), respectively. Both areas have evolved enough in the last decades to address the resolution of coupled problems, like FSI problems. But, this kind of problems brings new complications and complexities to be considered, such as the coupling techniques, the dynamic interaction, the different length and time scales of the subsystems, making the resolution of FSI problems much more difficult than the computation of the fluid and the structure separately. With this in mind, and due to the challenge that it represents, the contributions to this area are growing at a great rate nowadays, being in the objective of this thesis to contribute to the expansion of knowledge of this specific area.

1.2 Scope and objectives

In recent years, a substantial effort has been put into solving this kind of multiphysics systems, because it presents a great challenge to be tackled. So,

one of the objectives of this thesis is the development and implementation of a coupling algorithm for existing modules or subsystems, in order to carry out FSI simulations with the focus on distributed memory parallel platforms.

An important consideration to be taken into account when simulating FSI problems, is the choice of the kinematical description of the flow field in order to allow for the presence of mobile or deforming boundaries. In general, in fluid flow problems solved on fixed meshes an Eulerian description is used for its description. This facilitates the treatments of large distortion in the fluid motion and the simulation of turbulent flows, but its drawback is the difficult to follow an interface between different media (e.g., fluid-solid interfaces). An alternative is to use a Lagrangian description, in which each node of the mesh follows an associated material particle during the motion. This description allows the tracking of interfaces between different media, but the weakness is the treatment of large distortions of the computational mesh. An alternate choice is the Arbitrary Lagrangian Eulerian (ALE) description of the fluid field, which can handle problems with large distortions in presence of mobile boundaries. The idea behind the ALE formulation is the introduction of a computational mesh which moves with a velocity independent of the velocity of the material particles. The ALE formulation together with the governing equations are presented in Chapter (2) and the coupling of the sub-systems is presented in Chapter (3).

When an ALE formulation is used, additional terms related to the mesh velocity and position, are introduced. Also, the movements of the fluid mesh cause a volume change in time of the elements, which adds to the fluid formulation an extra conservation law to be satisfied. The law is known as the Discrete Geometric Conservation Law (DGCL). There is an extensive literature devoted to the impact of DGCL compliance on the stability of the numerical scheme and the precision of time integration methods. In those articles it has been proved that satisfying the DGCL is a necessary and sufficient condition for any ALE scheme to maintain on moving grids the nonlinear stability properties of its fixed-grid counterpart. However, only very few works propose a methodology for obtaining a DGCL compliant scheme, without changing the time integration method.

In this thesis a new and original methodology for developing DGCL compliant formulations based on an Averaged ALE Jacobians Formulation (AJF) is presented in Chapter (4) . It is carried out in the context of the FEM for general advective-diffusive systems on moving domains using an ALE scheme and a θ-family time integration scheme. The methodology is extended to the three point Backward Differential Formula (BDF), giving a wide range of possible applications.

In Chapter (5) are performed a set of numerical test in order to validate the numerical solvers and the coupling algorithm. Finally, the interaction between the fluid and the structure during the start-up process of a rocket engine nozzle is carried out. In Chapter (6) an alternative use of the FSI code developed in previous sections is shown. The simulation of FSI problems assuming incompressible viscous flows opens a wide range of problems that can be addressed. Finally, the original contributions and the research activities carried out during the course of this thesis are presented in Chapter (7). Also, a brief discussion about the performed simulations and its results are exposed.

The implementations are carried out in PETSc-FEM (Storti et al., 2010), which is a general purpose, parallel, multiphysics FEM program for CFD applications based on PETSc (Balay et al., 2011). It is written in the C++ language with an OOP (Object Oriented Programming) philosophy, keeping in mind the scope of efficiency. PETSc-FEM can run in parallel using the Message Passing Interface (MPI) standard, allowing the solution of large systems of non-linear equations.

1.3 Related work

Multiphysics coupled problems represent nowadays a paradigm when analyzing even more complex phenomena that appear in nature and in new technologies. There exists a great number of problems where different physical processes (or models) converge, interacting in a strong or weak fashion. In the FSI area, the dynamic interaction between an elastic structure and a compressible or incompressible fluid has been subject of intensive investigations in the last years. In civil engineering, wind flow may lead to aeroelastic instabilities due

to the structural motion on long-span bridges, high-rise buildings, light-weight roof structures and flexible silos, these problems have been addressed in works like, Koh et al. (1998) and Dooms (2009). In biomechanical applications, the blood flow interacts with thin vascular walls, so it is important to know the hemodynamics and wall shear stress to understand the mechanisms leading to various complications in cardiovascular function, like aneurysms; these problems have been addressed in works like, Nobile (2001); Hron and Turek (2006); Tezduyar et al. (2009). In aeronautical engineering (Piperno and Farhat, 2001; Gnesin and Rzadkowski, 2005) it is essential to understand the interaction between a high Mach number fluid with an elastic structure, like the aircraft wing, to predict the flutter velocity and avoid this flight condition. Other processes like the start up of a rocket engine (Lefrancois et al., 1999; Ludeke et al., 2006; Garelli et al., 2008, 2010) has been widely studied considering the interaction between the fluid and the nozzle.

In general, when solving FSI problems, the characteristic time and space scales vary widely, so the simulations tend to be arduous in the coupling process and time-consuming in the solution process, because the whole coupled problem is characterized by the smaller time scale to simulate. However, there exists a great interest in solving coupled multiphysics problems, with the aim to obtain reliable predictions of the system behavior. This interest has been accompanied by the increase in computer power in terms of CPU and memory, allowing to obtain results in reasonable time.

Nowadays, the methodologies and techniques behind each discipline involved in FSI problems (e.g., CFD, CSD, etc.) have been developed enough to allow the reliable simulation of a great variety of problems. These advances in the numerical simulation have been implemented in specialized codes. Therefore, an option is to couple these specialized codes with the objective of solving FSI problems, but in this case new questions arise, such as the coupling techniques, addressed in Cebral (1996); Lohner et al. (1998); Felippa C.A. Park (1999); Park and Felippa (2000); Piperno and Farhat (2001); Storti et al. (2009) and the motion of the fluid mesh addressed in López et al. (2007). Another possibility for solving FSI problems is to combine in a single formulation the fluid and the structural governing equations as it was done in the works of Michler

et al. (2004) and Idelsohn et al. (2006), but this monolithic scheme may be mathematically unmanageable or its implementation can be a laborious task. Furthermore, the monolithic coupled formulation would change significantly if different fluid and/or structure models were considered.

This thesis has the focus on using specialized existing codes in order to obtain reliable predictions in FSI problems, considering a staggered fluid-structure coupling algorithm. In this approach, we have to solve a large system of non-linear equations, having the possibility of using (iterative) specifics solvers for each subsystem. Usually, this is done with Block-Jacobi, Block-Gauss-Seidel or related relaxation methods (Codina and Cervera, 1995; Artlich and Mackens, 1995). When a partitioned coupling technique is used, like in this thesis, a three-field system is involved in the analysis: the structure, the fluid and the moving mesh solver. The governing equations of the fluid are written, in general, in an Eulerian framework so it must be rewritten to allow the motion of the mesh using an ALE formulation. The ALE method was first proposed by Noh (1964); Hirt et al. (1974) in the context of finite differences, then it was extended to Finite Elements (Hughes et al., 1978; Donea, 1983) and to Finite Volumes (Trepanier et al., 1991). Also, the movement of the fluid mesh produces a volume change of the elements in time, being in this context where the DGCL arises, as was mentioned previously. This law was first introduced in (Thomas and Lombard, 1979) and it is a consistency criterion in which the numerical method must be able to reproduce exactly a constant solution on a moving domain (Boffi and Gastaldi, 2004; Étienne et al., 2009; Garelli et al., 2009). The impact of the DGCL on the stability and precision of the numerical methods is still unclear, but there is a general consensus in the development of schemes that satisfy the DGCL, in particular for FSI problems as mentioned in (Lesoinne and Farhat, 1996; Nobile, 2001; Farhat et al., 2001; Mavriplis and Yang, 2005; Ahn and Kallinderis, 2006).

Regarding the mesh movement, it can be performed using strategies like re-meshing or using a nodal relocation, maintaining the topology unchanged. To perform the nodal relocation of the mesh there exist several strategies, some of them use a tension or torsion spring system (Yang and Mavriplis, 2005) to propagate the boundary motion into the volume mesh and others solve a

linear elastic or pseudo-elastic problem (Johnson and Tezduyar, 1994; Xu and Accorsi, 2004; Stein et al., 2004) to deform the mesh. A more sophisticated strategy to produce the mesh motion is solving an optimization problem. This strategy may be classified as a particular case of an elastic problem where the material constitutive law is defined in terms of the minimization of certain energy functional that takes into account the degree of element distortion (López et al., 2007, 2008).

Chapter 2

Governing equations and solvers

In this chapter the governing equations for the fluid dynamics, the structural dynamics and the mesh dynamics are presented. These equations are implemented in PETSc-FEM and the objective of this chapter is to give an introduction to these modules and to the underlying physics. For the fluid dynamics equations a detailed description about the transformation from an Eulerian reference frame to an ALE reference frame is presented. Also, the used strategy to perform the mesh movement and some variants are presented.

2.1 Fluid dynamics

The dynamic behavior of a fluid flow is governed by the Navier-Stokes equations, which are set of coupled conservation laws. It can be enumerated as

- Conservation of mass,
- Conservation of momentum,
- Conservation of energy.

Another conservation law must be added to these conservation laws if an ALE framework is considered.

- Geometric Conservation Law.

The Navier-Stokes equations can also be simplified in order to reproduce some particular kind of flows, as example if the viscosity is assumed to be zero, the fluid is treated as inviscid (e.g., supersonic flows over an airfoil or inside of a rocket nozzle) and is treated as incompressible if the density variations with respect to the reference density is negligible (e.g., water flow in a pipe or duct). These approximations are made based on the characteristics of the flow (very thin boundary layer) or based on the properties of the fluid (high water's bulk modulus). In this thesis a compressible, viscous flow is considered and is described as a general advective-diffusive system in order to simplify its interpretation.

2.1.1 General advective-diffusive system

Let us start with the derivation of the ALE formulation for a general advective-diffusive system (Donea, 1983; Lesoinne and Farhat, 1996; Donea and Huerta, 2003), which can represent from a simple linear 1D advective-diffusive problem to a 3D compressible Navier-Stokes problem.

The governing equation to be expressed in an ALE framework can be written in a compact form as

$$\mathcal{R}(\mathbf{U}) \equiv \frac{\partial U_j}{\partial t} + \left(\mathcal{F}^c_{jk}(\mathbf{U}) - \mathcal{F}^d_{jk}(\mathbf{U}, \nabla\mathbf{U})\right)_{,k} = 0, \quad \text{in } \Omega^t \quad \forall t \in (0, \mathcal{T}) \tag{2.1}$$

where $1 \leq k \leq n_d$, n_d is the number of spatial dimensions, $1 \leq j \leq m$, m is the dimension of the state vector (e.g. $m = n_d + 2$ for compressible flow), t is time, $(\ )_{,k}$ denotes derivative with respect to the k-th spatial dimension, $\mathbf{U} = (\rho, \rho\mathbf{u}, \rho e)^t \in \mathbb{R}^{n_d}$ is the unknown state vector expressed in conservative variable. Where ρ , $\mathbf{u}$ and e represents the density, the velocity vector and the specific total energy respectively, and $\mathcal{F}^{c,d}_{jk} \in \mathbb{R}^{m \times n_d}$ are the convective and diffusive fluxes. Appropriate Dirichlet and Neumann conditions at the boundary and initial conditions must be imposed.

The differential equation (2.1) can be written in an integral form

$$\frac{\partial}{\partial t}\int_\Omega \begin{pmatrix} \rho \\ \rho\mathbf{u} \\ \rho E \end{pmatrix} d\Omega \; + \; \int_\Omega \begin{pmatrix} \rho\mathbf{u} \\ \rho\mathbf{u}\otimes\mathbf{u} + p\bar{\bar{I}} - \bar{\bar{\tau}} \\ \rho\mathbf{u}H - \bar{\bar{\tau}}\cdot\mathbf{u} - \kappa\nabla T \end{pmatrix}_{,k} d\Omega = 0, \tag{2.2}$$

where H is the total specific enthalpy

$$H = e + p/\rho + 1/2|\mathbf{u}|^2 = E + p/\rho \tag{2.3}$$

defined in terms of the specific internal energy ($\mathrm{h} = \mathrm{e} + \mathrm{p}/\rho$) and the specific kinetic energy, respectively.

This set of equations are closed by an equation of state, being for a polytropic gas

$$p = (\gamma - 1)[\rho e - \frac{1}{2}\rho||\mathbf{u}||^2], \tag{2.4a}$$

$$T = C_v[e - \frac{1}{2}\rho||\mathbf{u}||^2], \tag{2.4b}$$

where γ is ratio of specific heats and C_v is the specific heat at constant volume. In viscous fluxes, the stress tensor $\bar{\bar{\tau}}$ is defined for Newtonian flows as

$$\tau_{ij} = 2\mu\varepsilon_{ij}(\mathbf{u}) + \lambda(\nabla\cdot\mathbf{u})\delta_{ij}, \tag{2.5}$$

where the Stoke's hypothesis is

$$\lambda = -\frac{2}{3}\mu, \tag{2.6}$$

and the strain rate tensor is

$$\varepsilon_{ij}(\mathbf{u}) = \frac{1}{2}\left(\frac{\partial u_i}{\partial x_j} + \frac{\partial u_j}{\partial x_i}\right). \tag{2.7}$$

Finally, the dynamic viscosity is assumed to be given by the Sutherland's law, which gives for an ideal gas the viscosity as function of the temperature,

$$\mu = \mu_0 \left(\frac{T}{T_0}\right)^{3/2} \frac{T_0 + 110}{T + 110}, \tag{2.8}$$

where μ_0 is the viscosity at the reference temperature T_0.

In order to write the semi-discrete form of the compressible Navier-Stokes equations, it is convenient to write (2.1) in a quasi-linear form as described in Hughes (1987b); Tezduyar (2001); Donea and Huerta (2003).

$$\frac{\partial \mathbf{U}}{\partial t} + \mathbf{A}_k \frac{\partial \mathbf{U}}{\partial x_k} - \frac{\partial}{\partial x_k}\left(\mathbf{K}_{ki}\frac{\partial \mathbf{U}}{\partial x_i}\right) = 0, \quad \text{in } \Omega^t \quad \forall t \in (0, \mathcal{T}) \tag{2.9}$$

where

$$\frac{\partial \mathcal{F}^c}{\partial x_k} = \frac{\partial \mathcal{F}^c}{\partial \mathbf{U}}\frac{\partial \mathbf{U}}{\partial x_k} = \mathbf{A}_k \frac{\partial \mathbf{U}}{\partial x_k}, \tag{2.10a}$$

$$\frac{\partial \mathcal{F}^d}{\partial x_k} = \frac{\partial \mathcal{F}^d}{\partial \mathbf{U}}\frac{\partial \mathbf{U}}{\partial x_k} = \mathbf{K}_{ki} \frac{\partial \mathbf{U}}{\partial x_k}, \tag{2.10b}$$

and $\mathbf{A}_k$ are the Jacobians of advective fluxes and $\mathbf{K}_{ki}$ are the Jacobians of diffusive fluxes.

2.1.2 Variational Formulation and ALE mapping

Previous to addressing the variational formulation of the governing equation, it is necessary to define the mapping process to solve problems in an ALE framework. As the problem is posed in a time-dependent domain Ω^t, it can not be solved with standard fixed-domain methods, so that it is assumed that there is an inversible and continuously differentiable map $\mathbf{x} = \boldsymbol{\chi}(\boldsymbol{\xi}, t)$ between the current domain Ω^t and a reference domain Ω^ξ, which may be for instance the initial domain $\Omega^\xi = \Omega^{t=0}$, and $\boldsymbol{\xi}$ is the coordinate in the reference domain.

The Jacobian of the transformation is

$$J = \left|\frac{\partial x_j}{\partial \xi_k}\right|, \tag{2.11}$$

and satisfies the following volume balance equation

$$\left.\frac{\partial J}{\partial t}\right|_{\boldsymbol{\xi}} = J\frac{\partial v_k^*}{\partial x_k}, \tag{2.12}$$

where

$$v_k^* = \left.\frac{\partial x_k}{\partial t}\right|_{\boldsymbol{\xi}}, \tag{2.13}$$

are the components of the mesh velocity, which are then used in the variational formulation to obtain the ALE form of the governing equations.

Now, the variational formulation of the general advective-diffusive system (2.1) using FEM is obtained. Multiplying equation (2.1) with a weighting function $w(\mathbf{x},t) = w(\boldsymbol{\chi}(\mathbf{x},t))$ and integrating over the current domain Ω^t, we obtain

$$\int_{\Omega^t} w\,\frac{\partial U_j}{\partial t}\,\mathrm{d}\Omega^t + \int_{\Omega^t}\left[\mathcal{F}^c_{jk} - \mathcal{F}^d_{jk}\right]_{,k} w\,\mathrm{d}\Omega^t = 0. \tag{2.14}$$

The integrals are brought to the reference domain Ω^ξ

$$\int_{\Omega^\xi} w\,\frac{\partial U_j}{\partial t} J\,\mathrm{d}\Omega^\xi + \int_{\Omega^\xi}\left[\mathcal{F}^c_{jk} - \mathcal{F}^d_{jk}\right]_{,k} wJ\,\mathrm{d}\Omega^\xi = 0, \tag{2.15}$$

and the temporal derivative term can be converted to the reference mesh by noting that the partial derivative of U_j is in fact a partial derivative at $\mathbf{x} =$ constant, and then can be converted to a partial derivative at $\boldsymbol{\xi} =$ constant with the relation

$$\left.\frac{\partial U_j}{\partial t}\right|_{\mathbf{x}} = \left.\frac{\partial U_j}{\partial t}\right|_{\boldsymbol{\xi}} - v_k^*\frac{\partial U_j}{\partial x_k}. \tag{2.16}$$

So the temporal derivative term in (2.15) can be transformed, using (2.12), as follows

$$\begin{aligned} J\left.\frac{\partial U_j}{\partial t}\right|_{\mathbf{x}} &= J\left.\frac{\partial U_j}{\partial t}\right|_{\boldsymbol{\xi}} - Jv_k^*\frac{\partial U_j}{\partial x_k}, \\ &= \left.\frac{\partial (JU_j)}{\partial t}\right|_{\boldsymbol{\xi}} - JU_j\frac{\partial v_k^*}{\partial x_k} - Jv_k^*\frac{\partial U_j}{\partial x_k}, \\ &= \left.\frac{\partial (JU_j)}{\partial t}\right|_{\boldsymbol{\xi}} - J\frac{\partial (U_j v_k^*)}{\partial x_k}. \end{aligned} \tag{2.17}$$

Replacing (2.17) in (2.15), we get

$$\int_{\Omega^\xi} w(\boldsymbol{\xi}) \left.\frac{\partial}{\partial t}(JU_j)\right|_{\boldsymbol{\xi}} \mathrm{d}\Omega^\xi + \int_{\Omega^\xi} \left(\mathcal{F}^c_{jk} - v^*_k U_j - \mathcal{F}^d_{jk}\right)_{,k} w(\boldsymbol{\xi}) J \,\mathrm{d}\Omega^\xi = 0. \quad (2.18)$$

The temporal derivative can be commuted with the integral and the weighting function since both do not depend on time, so that

$$\frac{\mathrm{d}}{\mathrm{d}t}\left(\int_{\Omega^\xi} w\, JU_j \,\mathrm{d}\Omega^\xi\right) + \int_{\Omega^\xi} \left(\mathcal{F}^c_{jk} - v^*_k U_j - \mathcal{F}^d_{jk}\right)_{,k} wJ \,\mathrm{d}\Omega^\xi = 0, \quad (2.19)$$

and the integrals can be brought back to the Ω^t domain

$$\frac{\mathrm{d}}{\mathrm{d}t}\left(\int_{\Omega^t} w\, U_j \,\mathrm{d}\Omega^t\right) + \int_{\Omega^t} \left(\mathcal{F}^c_{jk} - v^*_k U_j - \mathcal{F}^d_{jk}\right)_{,k} w \,\mathrm{d}\Omega^t = 0. \quad (2.20)$$

The variational formulation can be obtained by integrating by parts, so that

$$\frac{\mathrm{d}}{\mathrm{d}t}\left(H(w, \mathbf{U})\right) + F(w, \mathbf{U}) = 0, \quad (2.21)$$

where

$$\begin{aligned} H(w, \mathbf{U}) &= \int_{\Omega^t} w\, U_j \,\mathrm{d}\Omega^t, \\ F(w, \mathbf{U}) &= A(w, \mathbf{U}) + B(w, \mathbf{U}), \\ A(w, \mathbf{U}) &= -\int_{\Omega^t} \left(\mathcal{F}^c_{jk} - v^*_k U_j - \mathcal{F}^d_{jk}\right) w_{,k} \,\mathrm{d}\Omega^t, \\ B(w, \mathbf{U}) &= \int_{\Gamma^t} \left(\mathcal{F}^c_{jk} - v^*_k U_j - \mathcal{F}^d_{jk}\right) n_k w \,\mathrm{d}\Gamma^t. \end{aligned} \quad (2.22)$$

Γ^t is the boundary of Ω^t, and n_k is its unit normal vector pointing to the exterior of Ω^t.

A consistent stabilization term $S(w, \mathbf{U})$, like proposed in references Brooks and Hughes (1982); Franca et al. (1992); Aliabadi and Tezduyar (1993); Aliabadi et al. (1993); Tezduyar and Senga (2006), is included to Eq.(2.22) in order to avoid numerical oscillations in advection dominated problems.

$$S(w, \mathbf{U}) = \int_{\Omega^t} \mathcal{P}_{(w)} \cdot \mathcal{R}(\mathbf{U}) \,\mathrm{d}\Omega^t. \quad (2.23)$$

This term includes a Streamline Upwind Petrov-Galerkin (SUPG) operator and a Shock Capturing (SC) operator. When an ALE formulation is used, some extra consideration must be taken into account in order to add the correct amount of stabilization, due to mesh movement.

The stabilization of the compressible Navier-Stokes equations in Eulerian reference frames, is carried out by weighting the residual with the following perturbation function

$$\mathcal{P}_{(w)} = \tau_{SUPG} \cdot \mathbf{A} \cdot \nabla w, \tag{2.24}$$

but, when an ALE reference frame is used, the advective jacobians must be transformed to

$$\widetilde{\mathcal{P}}_{(w)} = \tau_{SUPG} \cdot [\mathbf{A} - \mathbf{v}^* \mathbf{I}] \cdot \nabla w. \tag{2.25}$$

where $\mathbf{A}$ is the Jacobians of advective fluxes defined in (2.9).

With this transformation we ensure that discrete formulation is ‘‘ALE invariant’’, in other words, for a given problem the same solution is obtained regardless of the mesh velocity, as stated in Storti et al. (2006); Garelli et al. (2011).

Having the variational formulation of the governing equations (2.1) in an ALE framework, the discretization using the FEM is carried out. The domain Ω^t is discretized into Ω_k^t non-overlapping elements, with $\mathcal{K} = 1, ..., n_{el}$. We define an appropriate finite-dimensional space function, with $\mathcal{S}^h$ and $\mathcal{V}^h$ corresponding to the trial solutions and weighting functions, respectively. So, the finite element formulation in a quasi-linear form of (2.22) is written as

follows

$$\begin{aligned}
&\frac{\mathrm{d}}{\mathrm{d}t}\int_{\Omega^t} w^h\, U_j^h \,\mathrm{d}\Omega^t - \int_{\Omega^t}\left(\mathbf{A}_k^h U_j^h - v_k^{*h} U_j^h - \mathbf{K}_{ki}^h \frac{\partial U^h}{\partial x_i}\right) w_{,k}^h \,\mathrm{d}\Omega^t \\
&+ \int_{\Gamma^t}\left(\mathbf{A}_k^h U_j^h - v_k^{*h} U_j^h - \mathbf{K}_{ki}^h \frac{\partial U^h}{\partial x_i}\right) n_k^h w^h \,\mathrm{d}\Gamma^t \\
&+ \sum_{e=1}^{nel}\int_{\Omega_e^t} \tau_{SUPG}\; w_{,i}^h \cdot [\mathbf{A}_i^h - v^*{}_i \mathbf{I}]\left[\frac{\partial U_j^h}{\partial t} + \mathbf{A}_k^h \frac{\partial U_j^h}{\partial x_k} - \frac{\partial}{\partial x_k}\left(\mathbf{K}_{ki}^h \frac{\partial U_j^h}{\partial x_i}\right)\right] \mathrm{d}\Omega^t \\
&+ \sum_{e=1}^{nel}\int_{\Omega_e^t} \delta_{SC}\; w_{,i}^h \cdot \frac{\partial U_j^h}{\partial x_k} \,\mathrm{d}\Omega^t
\end{aligned} \tag{2.26}$$

In equation (2.26) the first three integrals correspond to the Galerkin formulation of equation (2.22). The two series of element level integrals correspond to the SUPG stabilization and shock capturing, respectively. These terms are added in order to prevent spatial oscillation in advective dominant problems and suppress overshoot and undershoot effects in the region of discontinuity (e.g., shock waves, etc).

There exist several ways to compute the stabilization parameter τ_{SUPG} and shock capturing term δ_{SC}. Only in simple cases (1D), optimal definitions of the coefficient matrix τ_{SUPG} can be found, which should be symmetric, positive definite, have dimensions of time and scale linearly with the mesh size. In multiple dimension problems, the numerical dissipation should be only added in the characteristic direction and not in the transverse one, i.e. it must be the ‘‘streamline’’. This is not trivial, because the advective jacobian matrices for compressible flow are not simultaneously diagonalizable in multidimensional equations.

In this thesis the standard SUPG formulation presented in Aliabadi et al. (1993) is adopted. The τ_{SUPG} matrix is defined as

$$\tau_{SUPG} = \max[0, \tau_a - \tau_d - \tau_\delta], \tag{2.27}$$

where τ_a,τ_d,τ_δ are the stabilization matrix due to the advection and diffusion terms and the matrix subtracted due to the presence of the shock-capturing

term, respectively. These matrices are defines as

$$\tau_a = \frac{h}{2(c + |\mathbf{u} - \mathbf{v}^*|)}\mathbf{I}, \tag{2.28a}$$

$$\tau_d = \frac{\sum_{j=1}^{n_d} \beta_j^2 \mathrm{diag}(\mathbf{K}_{\mathrm{jj}})}{(c + |\mathbf{u} - \mathbf{v}^*|)^2}\mathbf{I}, \tag{2.28b}$$

$$\tau_\delta = \frac{\delta_{SC}}{(c + |\mathbf{u} - \mathbf{v}^*|)^2}\mathbf{I}, \tag{2.28c}$$

where c is the speed of sound, and $h = 2(\sum_{a=1}^{n_{en}} |\mathbf{u} \cdot \nabla w|)^{-1}$ is the element size projected in the direction of the streamline, and $\boldsymbol{\beta}$ is compute as

$$\boldsymbol{\beta} = \frac{\nabla ||\mathbf{U}||_*^2}{||\nabla ||\mathbf{U}||_*^2||}, \tag{2.29}$$

and

$$||\cdot||_* = ||\cdot||_2. \tag{2.30}$$

The shock capturing operator used here is that proposed by Tezduyar and Senga (2004). To define the operator an unit vector oriented with the density gradient $\mathbf{j} = \nabla\rho^h/|\nabla\rho^h|$ and a characteristic length $h_j = 2(\sum_{a=1}^{n_{en}} |\mathbf{j} \cdot \nabla w_a|)^{-1}$ are needed. Thereby, the isotropic shock capturing factor is defined as

$$\delta_{SC} = \frac{h_j}{2}(|\mathbf{u} - \mathbf{v}^*| + c)\left(\frac{|\nabla\rho^h|h_j}{\rho_{ref}}\right), \tag{2.31}$$

Finally, the semi-discrete system (2.26) is discretized in time with the trapezoidal rule, where

$$\begin{aligned} H(w, \mathbf{U}^{n+1}) - H(w, \mathbf{U}^n) &= -\int_{t^n}^{t^{n+1}} F(w, \mathbf{U}^{t'})\, \mathrm{d}t', \\ &\approx -\Delta t\, F(w, \mathbf{U}^{n+\theta}). \end{aligned} \tag{2.32}$$

with $0 \leq \theta \leq 1$ and being $\mathbf{U}^{n+\theta}$ defined as

$$\mathbf{U}^{n+\theta} = (1 - \theta)\mathbf{U}_n + \theta\mathbf{U}^{n+1}. \tag{2.33}$$

And during the time step it is assumed that the nodal points move with constant

velocity, i.e.

$$\left.\begin{aligned} v_k^*(\boldsymbol{\xi}) &= \frac{x_k(\boldsymbol{\xi}, t^{n+1}) - x_k(\boldsymbol{\xi}, t^n)}{\Delta t}, \\ x_k(\boldsymbol{\xi}, t) &= x_k(\boldsymbol{\xi}, t^n) + (t - t^n) v_k^*(\boldsymbol{\xi}), \end{aligned}\right\}, \qquad \text{for } t^n \leq t \leq t^{n+1}. \tag{2.34}$$

This assumption is directly related with the DGCL, as will see in Chapter 4.

2.2 Structural dynamics

In this section an introduction to the structural continuum equations and its discretization in space and time are given. The focus of this work is on FSI, thus the structural part is briefly covered in this section. More detailed explanations about structural continuum equations can be found in works like Marsden and Hughes (1983); Landau et al. (1986) and about numerical approximations of theses equations can be found in Hughes (1987a); Zienkiewicz and Taylor (2005).

The structural dynamics is governed by the conservation of linear momentum, a constitutive equation which relates stress with strain and some kinematic relations. As one of the goals of this thesis is to solve a wide variety of FSI problems, therefore a model that admits large structural deformations is needed, thus a geometrically nonlinear description of the kinematics is required. However, a linear elastic constitutive law for the material is assumed. The latter can be changed without a great effort, enabling the code to simulate another material behavior.

The structure is described by the displacement vector $\mathbf{z}$, the material velocity field $\mathbf{v}_s = \frac{\mathrm{d}\mathbf{z}}{\mathrm{dt}}$, the density of the material ρ_s, the specific structural body force $\mathbf{b}$ and the Cauchy stress tensor $\bar{\bar{\sigma}}_s$, written in a Lagrangian description, with respect to the initial state Ω_s^0, so we have

$$\rho_s \frac{\mathrm{d}^2\mathbf{z}}{\mathrm{dt}^2} - \nabla \cdot \bar{\bar{P}} = \rho_s \mathbf{b} \quad \text{in} \quad \Omega_\mathrm{s}^0 \quad \forall \quad \mathrm{t} \in (0, \mathcal{T}), \tag{2.35}$$

where the tensor

$$\bar{\bar{P}} = J\bar{\bar{\sigma}}_s \bar{\bar{F}}^{-T}, \tag{2.36}$$

is called the first Piola-Kirchhoff tensor and

$$\bar{\bar{F}} = \bar{\bar{I}} + \nabla \mathbf{z}, \tag{2.37}$$

is the deformation gradient tensor and J is the Jacobian determinant.

For a convenient specification of the constitutive equation, the second Piola-Kirchhoff stress tensor $\bar{\bar{S}}$ is introduced and it is related to the first Piola-Kirchhoff stress tensor by $\bar{\bar{S}} = \bar{\bar{F}}^{-1}\bar{\bar{P}}$. For an isotropic linear-elastic material, the constitutive equation can be stated as

$$\bar{\bar{S}} = \lambda_s (\mathrm{tr}\bar{\bar{\mathcal{E}}})\bar{\bar{\mathrm{I}}} + 2\mu_s \bar{\bar{\mathcal{E}}}, \tag{2.38}$$

which relates the second Piola-Kirchhoff stress tensor with the Green-Lagrange strain tensor $\bar{\bar{\mathcal{E}}}$ by means of the Lamé constants λ_s and μ_s. The Green-Lagrange strain tensor is defined as

$$\bar{\bar{\mathcal{E}}} = \frac{1}{2}\left(\nabla \mathbf{z} + \nabla \mathbf{z}^T + \nabla \mathbf{z} \cdot \nabla \mathbf{z}^T\right) \tag{2.39}$$

which also can be written as

$$\bar{\bar{\mathcal{E}}} = \frac{1}{2}\left(\bar{\bar{F}}^T \bar{\bar{F}} - \bar{\bar{I}}\right) \tag{2.40}$$

These set of equations are complemented with the displacement and velocity field at $t = 0$ which represent the initial conditions

$$\mathbf{z}_{t=0} = \mathbf{z}_0, \quad \left.\frac{\mathrm{d}\mathbf{z}}{\mathrm{dt}}\right|_{t=0} = \dot{\mathbf{z}}_0 \ \text{ in } \ \Omega_{\mathrm{s}}^0 \tag{2.41}$$

and to complete the description of the initial boundary value problem for the structure, a displacement field on Dirichlet boundaries is prescribed

$$\mathbf{z}_t = \widetilde{\mathbf{z}} \ \text{ in } \ \Gamma_{\mathrm{s}}^{\mathrm{D}}, \tag{2.42}$$

and traction field on Neumann boundaries

$$\tilde{\mathbf{f}}_t = J\bar{\bar{\sigma}}_s \bar{\bar{F}}^{-T} \cdot \tilde{\mathbf{n}}, \quad \text{in} \quad \Gamma_{\mathrm{s}}^{\mathrm{N}} \tag{2.43}$$

In FSI problems a portion of the Neumann boundary is the interface with the fluid, which transfers the pressure of the fluid to a load in the structure.

2.2.1 Variational Formulation

Having derived the governing equations for the structure, the next step is to obtain the variational formulation (weak form). Using the principle of virtual work, where a virtual displacement $\delta\mathbf{z}$ is applied to equation (2.35) and integrating the result over the domain Ω_s^0 gives

$$\int_{\Omega_s^0} \delta\mathbf{z} \left(\rho_s \frac{\mathrm{d}^2\mathbf{z}}{\mathrm{dt}^2} - \nabla \cdot \bar{\bar{P}} - \rho_s \mathbf{b} \right) \mathrm{d}\Omega_{\mathrm{s}}^0 \ = 0. \tag{2.44}$$

As the stress depends on strains which are derivatives of displacements, the equation (2.44) requires the computation of second derivatives of the displacement. But, this second derivatives can be reduced by performing an integration by parts of equation (2.44), obtaining the following weak form

$$\int_{\Omega_s^0} \delta\mathbf{z}^T \ \rho_s \ \ddot{\mathbf{z}} \ \mathrm{d}\Omega_{\mathrm{s}}^0 + \int_{\Omega_{\mathrm{s}}^0} \delta\boldsymbol{\varepsilon}^{\mathrm{T}} \ \bar{\bar{\mathrm{S}}} \ \mathrm{d}\Omega_{\mathrm{s}}^0 - \int_{\Omega_{\mathrm{s}}^0} \delta\mathbf{z}^{\mathrm{T}} \ \mathbf{b} \ \mathrm{d}\Omega_{\mathrm{s}}^0 - \int_{\Gamma_{\mathrm{s}}^0} \delta\mathbf{z}^{\mathrm{T}} \ \tilde{\mathbf{f}} \ \mathrm{d}\Gamma_{\mathrm{s}}^0 \ = 0, \tag{2.45}$$

where $\delta\boldsymbol{\varepsilon}$ represents the variation of the strain tensor $\bar{\bar{\mathcal{E}}}$ due to a variation $\delta\mathbf{z}$ of the displacement field. Now, the discretization in space of the weak form (2.45) is carried out by means of FEM, obtaining a semi-discrete system. The domain Ω_s is discretized into Ω_{sk} non-overlapping elements, with $\mathcal{K}_s = 1, ..., n_{el}$ and the continuous unknown displacement field $\mathbf{z}$ is approximated by

$$\mathbf{z}^h = \mathbf{w}\mathbf{z}, \qquad \delta\mathbf{z}^h = \mathbf{w}\delta\mathbf{z}, \qquad \ddot{\mathbf{z}}^h = \mathbf{w}\ddot{\mathbf{z}}. \tag{2.46}$$

where $\mathbf{w}$ is the matrix of shape functions.

Substituting the above approximations into the weak form (2.45) gives, for

a single element

$$\delta(\mathbf{z}^h)^T \left[\int_{\Omega^0_{sk}} \mathbf{w}^T \rho_s \mathbf{w} \; \mathrm{d}\Omega^0_{\mathrm{sk}} \; \ddot{\mathbf{z}}^{\mathrm{h}} + \int_{\Omega^0_{\mathrm{sk}}} \mathbf{B}^{\mathrm{T}} \; \bar{\bar{\mathrm{S}}} \; \mathrm{d}\Omega^0_{\mathrm{sk}} - \int_{\Omega^0_{\mathrm{sk}}} \mathbf{w}^{\mathrm{T}} \mathbf{b} \mathrm{d}\Omega^0_{\mathrm{sk}} - \int_{\Gamma^0_{\mathrm{sk}}} \mathbf{w}^{\mathrm{T}} \; \tilde{\mathbf{f}} \; \mathrm{d}\Gamma^0_{\mathrm{sk}} \right] \quad (2.47)$$

Noting that the virtual displacements are arbitrary, the sum over all elements is performed obtaining the following semi discrete system.

$$\mathbf{M}\ddot{\mathbf{z}}^h + \mathbf{F}_{int}(\dot{\mathbf{z}}^h, \mathbf{z}^h) = \mathbf{F}_{ext}, \quad (2.48)$$

where

$$\begin{aligned} \mathbf{M} &= \sum_k \mathbf{M}_k = \sum_k \int_{\Omega^0_{sk}} \mathbf{w}^T \rho_s \mathbf{w} \; \mathrm{d}\Omega^0_{\mathrm{sk}}, \\ \mathbf{F}_{int}(\mathbf{z}^h) &= \sum_k \mathbf{F}_{int}(\mathbf{z}^h)_k = \sum_k \int_{\Omega^0_{sk}} \mathbf{B}^T \; \bar{\bar{S}} \; \mathrm{d}\Omega^0_{\mathrm{sk}}, \\ \mathbf{F}_{ext} &= \sum_k \mathbf{F}_{ext_k} = \sum_k \int_{\Omega^0_{sk}} \mathbf{w}^T \mathbf{b} \; \mathrm{d}\Omega^0_{\mathrm{sk}} + \sum_{\mathrm{k}} \int_{\Gamma^0_{\mathrm{sk}}} \mathbf{w}^{\mathrm{T}} \; \tilde{\mathbf{f}} \; \mathrm{d}\Gamma^0_{\mathrm{sk}}. \end{aligned} \quad (2.49)$$

Finally, the semi discrete system (2.48) is discretized in time using the Newmark-β scheme proposed by Newmark (1959). This method is widely used in numerical evaluation of the dynamic response of structures and a general overview about this scheme and other can be found in Hughes (1987a).

The discrete position $\mathbf{z}^h = \mathbf{d}_s$ and velocity $\dot{\mathbf{z}}^h = \mathbf{v}_s$ are written in terms of the accelerations $\ddot{\mathbf{z}}^h = \mathbf{a}_s$, wherewith

$$\begin{aligned} &\mathbf{M}\mathbf{a}_s^{n+1} + \mathbf{F}_{int}(\mathbf{v}_s^{n+1}, \mathbf{d}_s^{n+1}) = \mathbf{F}_{ext}^{n+1}, \\ &\mathbf{v}_s^{n+1} = \mathbf{v}_s^n + \Delta t((1-\gamma_n)\mathbf{a}_s^n + \gamma_n \mathbf{a}_s^{n+1}), \\ &\mathbf{d}_s^{n+1} = \mathbf{d}_s^n + \Delta t \mathbf{v}_s^n + \frac{1}{2}\Delta t^2((1-2\beta_n)\mathbf{a}_s^n + 2\beta_n \mathbf{a}_s^{n+1}). \end{aligned} \quad (2.50)$$

is obtained a displacement based formulation.

Both parameters γ_n and β_n determine the stability and accuracy characteristics of the scheme. Several works have been carried out to determine these properties for different value of γ_n and β_n, which are summarized in the Table (2.1). The stability is based upon the undamped case and a second order

Table 2.1: Numerical properties of some Newmark-β schemes.

Method	β_n	γ_n	Stability	Order of accuracy
Average Acceleration	1/4	1/2	Unconditional	2
Linear Acceleration	1/6	1/2	Conditional	2
Fox-Goodwing	1/12	1/2	Conditional	2

of accuracy is achieved if and only if ($\gamma_n = 1/2$), otherwise if ($\gamma_n > 1/2$) a numerical damping proportional to ($\gamma_n - 1/2$) is introduced. The unconditional stability is achieved for ($2\beta_n \geq \gamma_n \geq 1/2$). So, the average acceleration method is one of the most widely used in structural dynamics due to it is unconditionally stable without the introduction of numerical damping.

2.3 Mesh dynamics

In this section a brief introduction to the moving mesh techniques is given. As was mentioned in previous sections, in FSI problems the fluid interacts with a structure which deforms due to the forces exerted by the fluid, producing a change in the fluid domain, since the fluid-structure interface follows the structure displacement. In the discrete fluid flow problem, the change of the domain must be followed by a change in the discretization. The discretization of the new domain can be obtained through a re-meshing process or through a nodal relocation process.

In general, the re-meshing process is undesirable because of the need of a projection of the flow field from the old to the new mesh, with the consequent loss of conservativity, possible addition of numerical diffusion and additional computational cost. In this work, a relocation technique is used to update the nodal coordinates of the fluid mesh in response to the domain deformation, while keeping the topology unchanged.

There exists several techniques to produce the nodal relocation and the choice of one of these depends on how important is the deformation of the structure and its impact on the fluid domain. The simplest one is the Laplacian method which consists in solving the Laplace equation to update the node

positions. Also, some modifications have been proposed to the Laplacian operators (Löhner and Yang, 1996; Longatte et al., 2003) for special treatment of near wall regions. Other technique is the spring analogy, where the mesh nodes are connected through tension springs, where the stiffness is related to the length of the edge. This approach tends to produce highly deformed meshes with collapsed or negative volume and is incapable of reproducing solid body rotation. The tension spring model has been improved by Murayama et al. (2002) attaching torsion springs to each vertex where the stiffness is related to the angle. In the work of Farhat et al. (1998) tension and torsion spring to produce the mesh movement are used, with good results.

A more robust alternative is the linear elasticity approach, where fluid mesh obey the linear elasticity equation (Stein et al., 2004) to obtain a smooth displacement field, setting as boundary condition the displacement of the interface. The equations describing the elastic medium under the hypothesis of small deformations without external forces are

$$\nabla \cdot \bar{\bar{\sigma}} = 0, \tag{2.51a}$$

$$\bar{\bar{\sigma}} = \lambda_s(\mathrm{tr}\bar{\bar{\mathrm{E}}})\bar{\bar{\mathrm{I}}} + 2\mu_s\bar{\bar{\mathrm{E}}}, \tag{2.51b}$$

$$\bar{\bar{E}} = \frac{1}{2}\left(\nabla\mathbf{x} + \nabla\mathbf{x}^T\right), \tag{2.51c}$$

where $\mathbf{x}$ is the displacement field and for constants λ_s and μ_s can be written as

$$\mu_s\nabla^2\mathbf{x} + (\lambda_s + \mu_s)\nabla(\nabla \cdot \mathbf{x}) = 0. \tag{2.52}$$

In this approach the Lamé constants depend on the Young's modulus and Poisson ratio, so a variable Young's modulus can be used in order to avoid severe mesh deformation in critical regions, like boundary layers, trailing-edge airfoil, relegating the mesh deformation to areas where the mesh is coarse. Exist other alternatives, like employing a distribution which is inversely proportional to the element volume, in order to deal with severe fluid mesh deformations. These strategies, together with others are mentioned in Löhner (2008) and can be used to admit large mesh movement while maintaining good mesh qualities.

This method with a variable modulus of elasticity is used in most of the numerical examples of this thesis. But additionally, the moving mesh module of PETSc-FEM has implemented a robust method proposed by Lopez et al. (2007), where the mesh motion strategy is defined as an optimization problem. By its definition this strategy may be classified as a particular case of an elastostatic problem where the material constitutive law is defined in terms of the minimization of certain energy functional that takes into account the degree of element distortion. Some advantages of this strategy is its natural tendency to high quality meshes and its robustness. This strategy is used in the problem presented in (5.5.1)

With the aim of showing the robustness of the different alternatives implemented in PETSc-FEM, a very simple test is carried out. A NACA-0012 airfoil is forced to rotate as a rigid solid around its quarter chord from 0° to 30° of angle of attack. The nodes at the external boundary are fixed, while the nodes on the airfoil are moved as a rigid solid. The computational domain and the dimensions are shown in Figure(2.1).

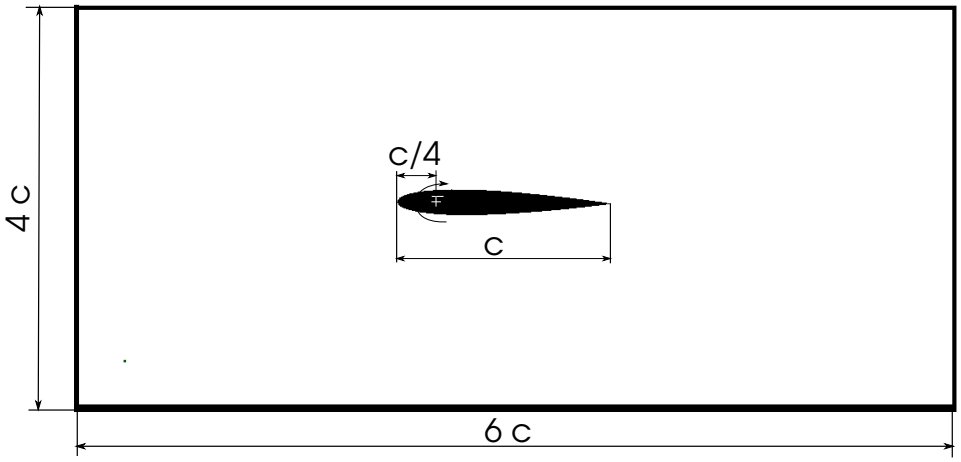

Figure 2.1: Dimensions of the computational domain.

The domain is discretized with 2057 linear triangular elements and has the histogram of element quality showed in Fig.(2.2). In the following tests the Scaled Jacobian metric defined in the work of Knupp (2000) is used as element quality indicator, where the quality range goes from 1 to -1 (best element, worst

element). This metric is independent of the element volume and rotation.

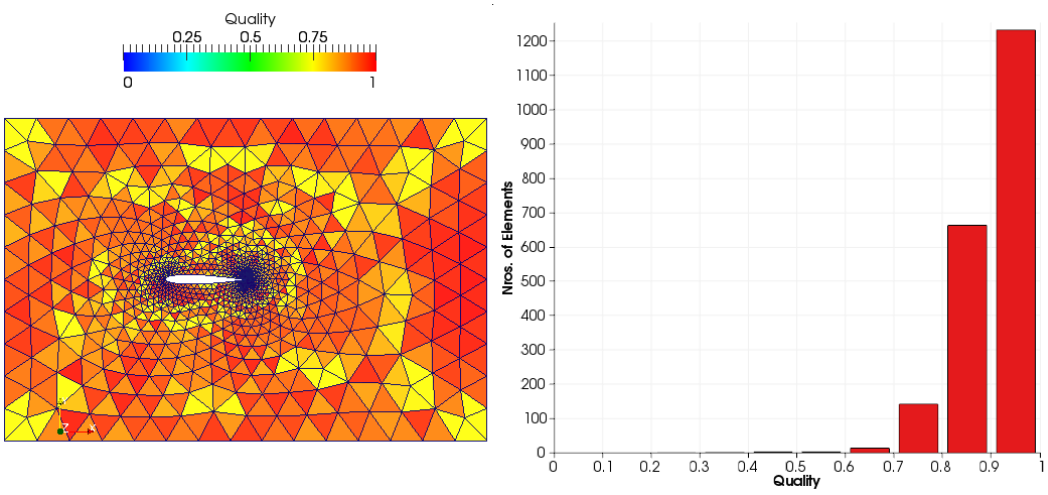

Figure 2.2: Triangular mesh and histogram of the Scaled Jacobian quality.

From the histogram can be determined that over the 98% of the elements has a quality greater than 0.7. Now the airfoil is gradually rotated to an angle of attack of 30°. In the first test, the mesh is deformed according to the linear elasticity approach, using an uniform Young's modulus of 1 and a Poisson's ratio of 0.4. With this strategy we only can reach a maximum angle of attack of 14° before some elements are inverted in the region of the trailing edge, as can be seen in Figures (2.3) and (2.4)

In the next test, the same strategy is used with the difference that in the region near the airfoil the Young's modulus is increased 1000 times, reaching the desired 30° of angle of attack, but the overall quality of the mesh is deteriorated mainly in the transition region,as can be seen in Figure (2.5).

This technique of mesh movement is cheaper from the computational point of view, but the user is responsible for the specification of the Young's modulus variations in the different regions of the domain.

The last test is carried out using the strategy proposed in Lopez et al. (2007); López et al. (2008), where the mesh motion is defined as an optimization problem. This is more expensive in computational terms, but maintains 98% of the elements with a quality above 0.7, like in the original mesh. This approach must be used in cases with severe deformations of the structure,

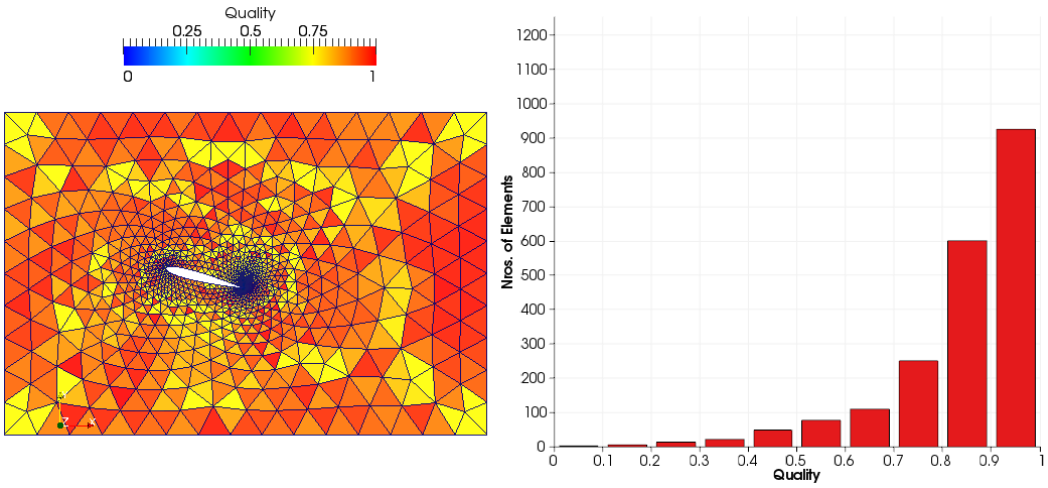

Figure 2.3: Linear elasticity approach with uniform Young's modulus.

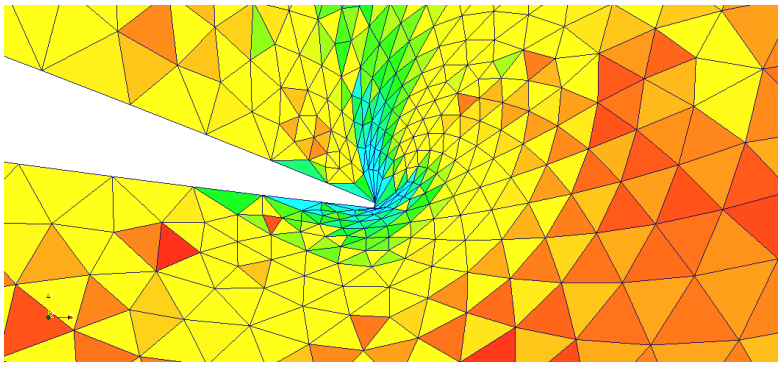

Figure 2.4: Trailing edge region.

while maintaining a good quality of the mesh. Additionally, in the work of Mavriplis and Yang (2005) a detailed analysis comparing different mesh movement strategies is carried out.

These examples show that PETSc-FEM has several alternatives in order to produce the mesh movement. The method to be selected by the user will depend on the problem to be solved and how important is the distortion of the mesh. Also, the computational cost will differ from one method to another.

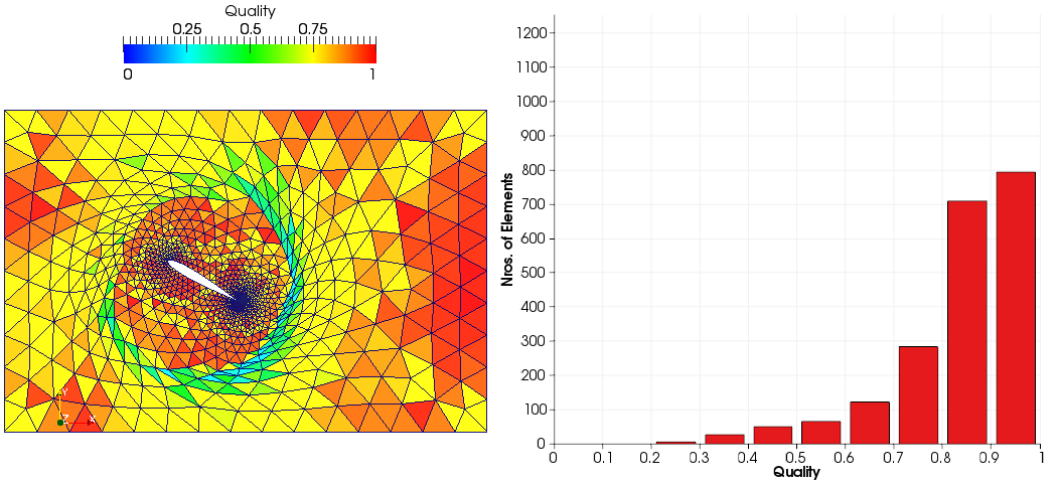

Figure 2.5: Linear elasticity approach with variable Young's modulus.

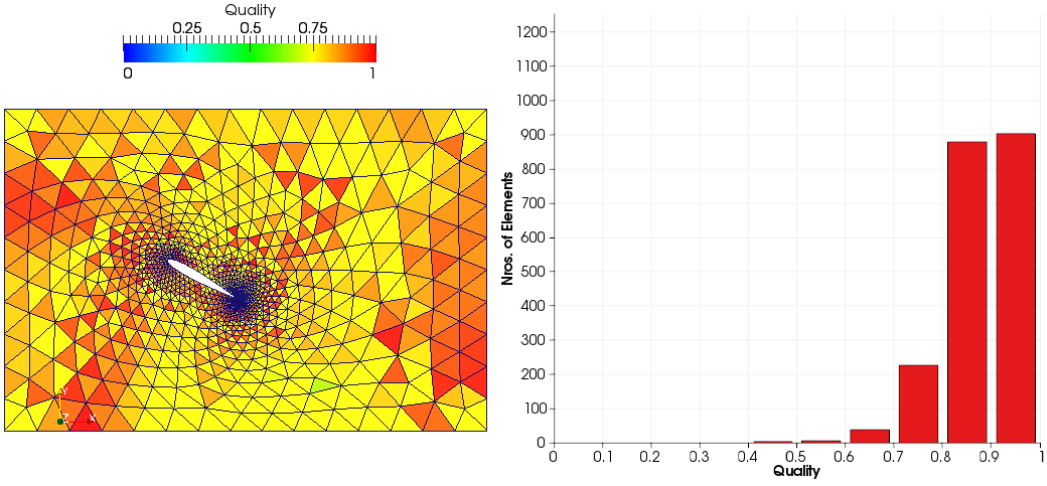

Figure 2.6: Optimization approach.

Chapter 3

Coupling strategies for FSI

In this chapter the strategy used to couple the structural dynamics and the mesh dynamics problems the fluid dynamics is described and analyzed. To carry out this task, different alternatives can be chosen , each with its pros and cons. Also, the arguments for choosing a partitioned treatment will be exposed in this chapter.

3.1 Partitioned and monolithic coupling strategies

With the increase of multi-physics problems to be solved, both in industry and research, a wide variety of coupling strategies has been proposed, which can be found in different books like, Bungartz et al. (2006); Ohayon and Kvamsdal (2006); Galdi and Rannacher (2010); Bazilevs et al. (2011) and classified in the following groups (See Figure (3.1)).

In the monolithic treatment the equations governing the fluid flow and the displacement of the structure are solved simultaneously, with a single solver (Michler et al., 2004; Idelsohn et al., 2009; Ryzhakov et al., 2010). The advantage of this treatment is its accuracy and robustness since all components are advanced simultaneously in time and ensure energy conservation, but the numerical solution of the discrete system requires sophisticated solvers of nonlinear systems and fast solvers for very large linear systems, as mentioned

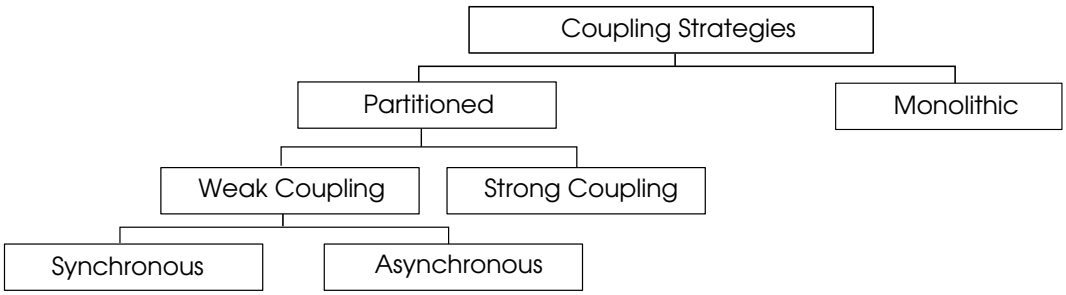

Figure 3.1: Coupling strategies.

in Hron and Turek (2006). Also, the inability to couple existing fluid and structural solver is an important drawback, because it requires the development and implementation of the overall code.

In the partitioned treatment two independent solvers are used to deal with each problem (fluid and structure). The interaction process is carried out trough the exchange of information at the fluid/structure interface in a staggered way. The structural solver establishes the position and velocity of the interface, while the fluid solver establishes the pressure and shear stresses on the interface. The principal advantage of the partitioned treatment, an the reason because it became so popular is that existing optimized solvers can be reused and coupled. The systems to be solved are smaller and better conditioned than in the monolithic case. However the disadvantage of this approach is that it requires a careful implementation in order to avoid serious degradation of the stability and accuracy. From this basic approach a weak (Explicit) scheme can be developed, with either synchronous or asynchronous time coupling, or either a strong (Implicit) time coupling scheme. Each one of these schemes will be described and analyzed in next section.

3.2 Weak and Strong coupling strategies

In this section the possible temporal algorithms that performs the coupling between the structure and the fluid codes are described. In its general form, the time coupling scheme can be viewed as a fixed point iteration scheme over the variables of both fluid and structure systems. During the iterative process

three codes CFD (Computational Fluid Dynamics), CSD (Computational Structure Dynamics) and CMD (Computational Mesh Dynamics) are running simultaneously. For simplicity, the basic algorithm can be described as if there were no concurrence between the codes, i.e. at a given time only one of them is running.

The basic scheme proceeds as follows:

i) Transfer the motion of the wet boundary (interface) of the solid to the fluid problem.

ii) Update the position of the fluid boundary and the bulk fluid mesh accordingly.

iii) Advance the fluid system and compute new pressures.

iv) Convert the new fluid pressure (and stress field) into a structural load.

v) Advance the structural system under the flow loads.

From this basic description two different coupling schemes can be derived depending on how the prediction of the structural displacement for updating the position of the fluid boundary and compute new pressures is made. In all cases, both fluid and structure partitions are integrated with the trapezoidal algorithm (with trapezoidal parameter $0 < \theta \leq 1$) but another integration scheme could be used, such as linear multisteps methods, depending on the particular application (Mavriplis and Yang, 2005). To proceed with the description of the scheme we define $\mathbf{w}^n$ to be the fluid state vector $(\rho, \mathbf{v}, p)$, $\mathbf{z}^n$ to be the displacement vector (structure state vector), $\dot{\mathbf{z}}^n$ the structure velocities and $\mathbf{x}^n$ the fluid mesh node positions at time t_n.

In the weak (explicit) synchronous coupling (See Figure (3.2)) the fluid is first advanced using the previously computed structure state $\mathbf{z}^n$ and a current estimated value $\mathbf{z}_p^{n+1}$. In this way, a new estimation for the fluid state $\mathbf{w}^{n+1}$ is computed. Next the structure is updated using the forces of the fluid from states $\mathbf{w}^n$ and $\mathbf{w}^{n+1}$. The estimated state $\mathbf{z}_p^{n+1}$ is predicted using a second or higher order approximation (3.1), were α_0 and α_1 are two real constants. The predictor (3.1) is trivial if $\alpha_0 = \alpha_1 = 0$, first-order time-accurate if $\alpha_0 = 1$ and

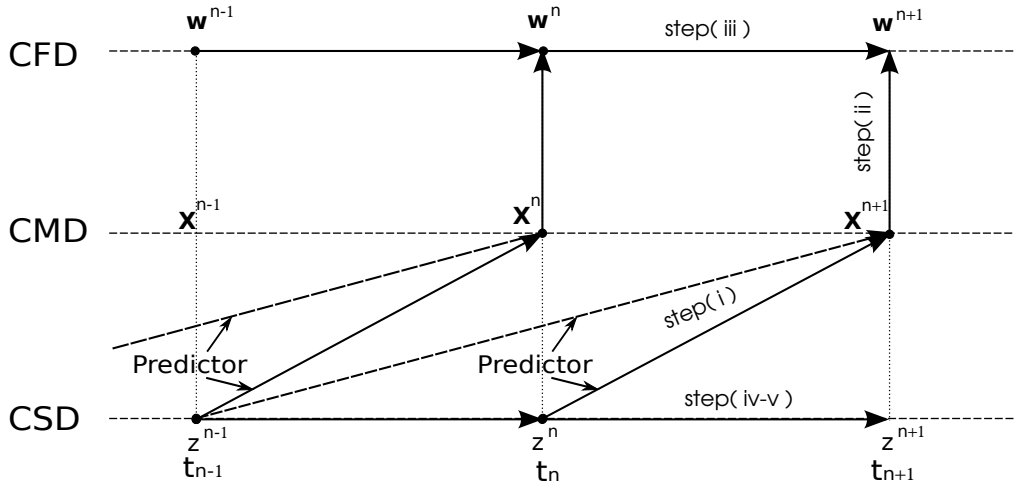

Figure 3.2: Weak synchronous coupling scheme.

second-order time-accurate if $\alpha_0 = 1$ and $\alpha_1 = 1/2$. This coupling scheme has been proposed in Farhat et al. (1995); Piperno (1997), with good results in the resolution of aeroelastic problems. Also, Piperno and Farhat (2001) gives a description about the use of the predictor (3.1) on FSI problems and the energy transfer between the fluid and the structure.

$$\mathbf{z}_p^{(n+1)} = \mathbf{z}^n + \alpha_0 \Delta t \dot{\mathbf{z}}^n + \alpha_1 \Delta t (\dot{\mathbf{z}}^n - \dot{\mathbf{z}}^{n-1}). \tag{3.1}$$

Once the coordinates of the structure are known, the coordinates of the fluid mesh nodes are computed by a CMD code, which is symbolized as:

$$\mathbf{x}^{n+1} = \mathrm{CMD}(\mathbf{z}^{n+1}). \tag{3.2}$$

In Longatte et al. (2009) the advantage of using this coupling algorithm is highlighted, but also the difficulty of satisfying the geometric conservation law is mentioned. Therefore, in this thesis a new methodology in order to satisfy the geometric conservation law is proposed in Chapter 4 in order to avoid the introduction of a numerical error due to mesh movement.

For the case of weak (explicit) asynchronous coupling, which will not be addressed in this thesis, fluid and structure problems are not solved at the same time, in general the fluid computations are expressed at time $t_{n+1/2}$, while the

structure computations are expressed at t_{n+1}, obtaining a first-order accurate coupling scheme which is a disadvantage from the point of view of stability, but this scheme has an improvement in terms of parallelism, as mentioned in Farhat et al. (1995).

Finally, the third scheme is the strong (implicit) synchronous coupling, which have benefits is term of stability and is comparable with a monolithic coupling. It was proved (Michler et al., 2004) that monolithic schemes and strongly-coupled staggered schemes conserves energy transfer at the fluid-structure interface boundary, whereas weak coupled algorithms introduce after a certain amount of time t an artificial energy $E = \mathcal{O}(\Delta t^p)$, where p will depend on the order of the prediction and the time integration methods used in the fluid and structure solver, as mentioned in Farhat et al. (2006).

In the strong synchronous coupling algorithm, the time step loop is equipped with an inner loop called ‘‘stage’’, so if the ‘‘stage loop’’ converges, then a ‘‘strongly coupled’’ algorithm is obtained. A schematic diagram is shown in Figure (3.3). With this coupling strategy the computational cost increases

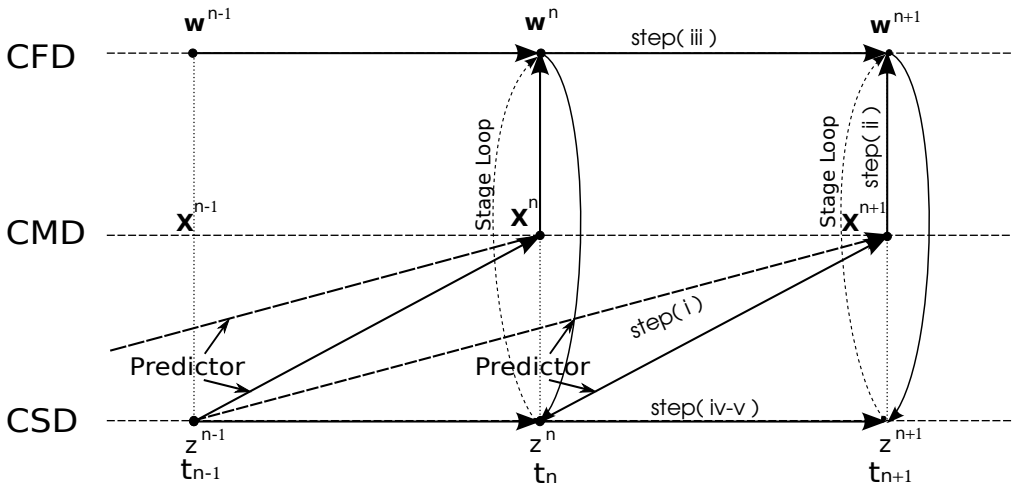

Figure 3.3: Strong synchronous coupling scheme.

proportionally to the number of stages needed to achieve the desired error, but also it allows to use large time steps.

At the beginning of each fluid stage there is a computation of skin normals and velocities. This is necessary due to the time dependent slip boundary

condition for the inviscid case, $((\mathbf{v}|_\Gamma - \dot{\mathbf{z}}|_\Gamma) \cdot \hat{\mathbf{n}} = 0)$ and also when using a non-slip boundary condition, where the fluid interface has the velocity of the moving solid wall, i.e., $\mathbf{v}|_\Gamma = \dot{\mathbf{z}}|_\Gamma$.

3.3 Energy conservation of the coupled system

When FSI problems are solved using a partitioned coupling scheme, some additional issues must be taken into account in order to obtain reliable simulations. One of these issues is the energy transfer through the interface from one system to the other. The firsts research work carried out to solve aeroelastic problems, used the simplest partitioning scheme (Borland and Rizzetta, 1982; Shankar and Ide, 1988), where the structure is deformed under the pressure load, then the mesh fluid is updated under the new structure configuration and finally the new pressure distribution over the structure is computed. Then, with the aim to improve the accuracy and stability of this scheme the use of a predictor was introduced, specially when the fluid governing equations are nonlinear and solved implicitly. As shown by Farhat et al. (1995), the loss in accuracy and stability of the partitioned treatment arises from a violation of the energy conservation at the interface, wherewith the coupling scheme only satisfies the energy conservation in an asymptotic way, i.e., reducing the time step and mesh. In general, the energy of the system increases, turning the system numerically unstable (Piperno and Farhat, 2001; Michler et al., 2004).

With the aim to perform a simplified analysis of the energy transfer we consider the one-dimensional inviscid case, where the interface is represented with a single node of unit area, defined as $\Gamma_{f/s}$ (See Figure 3.4). So, viewed from the fluid the energy transferred through the interface during a time step can be expressed with the following equation

$$\Delta E_f^{n+1} = -\int_{t_n}^{t_{n+1}} p(t)\dot{x}(t)\, dt = -F_f^{n+1^T}(\mathbf{x}^{n+1} - \mathbf{x}^n), \tag{3.3}$$

where F_f^{n+1} is the force applied by the fluid on $\Gamma_{f/s}$ and it depends on the time

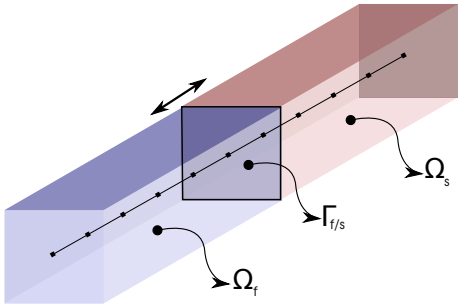

Figure 3.4: Sketch of 1D fluid-structure coupling.

integrator used in the flow solver to compute the fluxes across $\Gamma_{f/s}$. As stated in Eq.(2.32), the semi-discrete flow equations are discretized in time using the trapezoidal rule, obtaining the following values of F_f^{n+1} as a function of θ.

- $\theta = 0$ (Forward-Euler) $\rightarrow F_f^{n+1} = F^n$,
- $\theta = 0.5$ (Crank-Nicolson) $\rightarrow F_f^{n+1} = (F^n + F^{n+1})/2$,
- $\theta = 1$ (Backward-Euler) $\rightarrow F_f^{n+1} = F^{n+1}$.

Now, the energy transfer through the interface is viewed from the structure. The structural dynamics can be modeled using the following equation for displacement

$$\mathbf{M}\ddot{\mathbf{z}}^{n+1} + \mathbf{D}\dot{\mathbf{z}}^{n+1} + \mathbf{K}\mathbf{z}^{n+1} = \mathbf{F}_{ext}^{n+1}, \tag{3.4}$$

where $\mathbf{M}$,$\mathbf{D}$,$\mathbf{K}$ are the mass, damping and stiffness matrices respectively and $\ddot{\mathbf{z}}$,$\dot{\mathbf{z}}$,$\mathbf{z}$ are the acceleration, velocity and displacement vectors respectively. $\mathbf{F}_{ext}$ is the external force applied to the structure, in this case only the force exerted by the fluid on the structure is considered. The velocities and displacements are estimated using a midpoint integration rule

$$\begin{aligned} \dot{\mathbf{z}}^{n+1} &= \dot{\mathbf{z}}^n + \Delta t(\ddot{\mathbf{z}}^{n+1} + \ddot{\mathbf{z}}^n)/2, \\ \mathbf{z}^{n+1} &= \mathbf{z}^n + \Delta t(\dot{\mathbf{z}}^{n+1} + \dot{\mathbf{z}}^n)/2. \end{aligned} \tag{3.5}$$

The energy of the structure is composed of the kinetic and potential energies

$$E_s = \frac{1}{2}\dot{\mathbf{z}}^T\mathbf{M}\dot{\mathbf{z}} + \frac{1}{2}\mathbf{z}^T\mathbf{K}\mathbf{z}, \tag{3.6}$$

thus the structural energy variation during a time step due to the energy transferred from the fluid to the structure (code coupling) is given by

$$\Delta E_s^{n+1} = \frac{1}{2}(F_s^{n+1} + F_s^n)^T(\mathbf{z}^{n+1} - \mathbf{z}^n). \tag{3.7}$$

At this point we can state that a partitioned FSI coupling conserves energy if an only if it satisfies the following relation

$$\Delta E_s^{n+1} = \frac{1}{2}(F_s^{n+1} + F_s^n)^T(\mathbf{z}^{n+1} - \mathbf{z}^n) = -F_f^{n+1^T}(\mathbf{x}^{n+1} - \mathbf{x}^n) = \Delta E_f^{n+1}, \tag{3.8}$$

but it is important to note that $\mathbf{x}^{n+1}$, which represents the fluid mesh displacement at t^{n+1} is not known when the fluid state is advanced from $\mathbf{w}^n$ to $\mathbf{w}^{n+1}$, as can be viewed in Figure (3.2) and F_f^{n+1} will depend on the adopted value for the θ parameter, wherewith $\mathbf{w}^{n+1}$ and F_f^{n+1} must be chosen so as to minimize the energy imbalance.

In the case of weak coupling without structural predictor, the structural displacement $\mathbf{z}^{n+1}$ is inferred from the fluid force F_f^n and the mesh displacement $\mathbf{x}^n$. In this thesis the structural predictor described in Eq.(3.1) proposed by Piperno and Farhat (2001) is used in order to improve the energy conservation and hence the stability of the system without increasing the computational costs. When a first order predictor, setting on Eq.(3.1) $\alpha_0 = 1$ and $\alpha_1 = 0$ and a second order flow solver is used, the coupling algorithm become second order energy accurate. Another alternative is to use a second order predictor, setting on Eq.(3.1) $\alpha_0 = 1$ and $\alpha_1 = 1/2$ where the coupling algorithm become third order energy accurate.

But in some particular cases, like the flutter of a flat plate or finding the instability velocity of a wing, the introduction of artificial energy in the system can lead to an erroneous result. In those cases a strong coupling algorithm is needed, where k stages are performed until the error becomes lower than a critical value

$$\frac{|(F_f^{n+1})^{k+1} - (F_f^{n+1})^k|}{|(F_f^{n+1})^0|} < \varepsilon, \tag{3.9}$$

and them the system is advanced in time.

Chapter 4

Geometric Conservation Law

In this section a new methodology for developing DGCL (Discrete Geometric Conservation Law) compliant formulations is presented. It is carried out in the context of the FEM for general advective-diffusive systems (2.1) on moving domains using an Arbitrary Lagrangian Eulerian (ALE) scheme given in (2.20). There is an extensive literature about the impact of DGCL compliance on the stability and precision of time integration methods. In those articles it has been proved that satisfying the DGCL is a necessary and sufficient condition for any ALE scheme to maintain on moving grids the nonlinear stability properties of its fixed-grid counterpart. However, only a few works propose a methodology for obtaining a compliant scheme (Storti et al., 2011). In this thesis, a DGCL compliant scheme based on an Averaged ALE Jacobians Formulation (AJF) is obtained. This new formulation is applied to the θ-family of time integration methods. In addition, an extension to the three-point Backward Difference Formula (BDF) is given.

4.1 The role of GCL

When dealing with partial differential equations that need to be solved on moving domains, like in FSI (Lefrancois et al., 1999; Tezduyar et al., 2008; Storti et al., 2009; Garelli et al., 2010), one of the most used technique is transform the equations in a ALE framework, as in this thesis. When an ALE

formulation is used, the governing equations are written in a moving domain and additional terms related to the mesh velocity and position, are introduced. The reformulated equations must be integrated in time. The common way to proceed is to use a classical time advancing scheme like the θ-family or the BDF's family. In this context the DGCL arises and it is directly related to the evolution of the mesh velocity and the elements volume change. This law was introduced by Thomas and Lombard (1979) and it is a consistency criterion in which the numerical method must be able to reproduce exactly a constant solution on a moving domain. As noted by Étienne et al. (2009) the effect of the DGCL on the stability of ALE schemes is still unclear and somewhat contradictory. In the work by Guillard and Farhat (2000), it has been observed that the movement of the domain can degrade the accuracy and stability of the numerical scheme with respect to their counterpart on fixed domains. In this direction, many researchers have been working with the aim of linking the accuracy and the stability of numerical schemes on an ALE framework with the discrete version of the Geometric Conservation Law (Guillard and Farhat, 2000; Boffi and Gastaldi, 2004; Formaggia and Nobile, 2004; Étienne et al., 2009). In the article of Geuzaine et al. (2003) it has been shown that satisfying the DGCL is neither necessary nor sufficient condition for an ALE scheme to preserve on moving grids its time-accuracy established on fixed grids. In the work presented by Farhat et al. (2001) it was proved that for nonlinear scalar problems the DGCL requirement is a necessary and sufficient condition for an ALE time-integrator to preserve the nonlinear stability properties of its fixed-grid counterpart. Meanwhile, Boffi and Gastaldi (2004) and Formaggia and Nobile (2004) have shown that it is neither necessary nor sufficient condition for stability, except for the Backward Euler scheme. While the impact of the DGCL on the stability and precision of the time integration methods is controversial, there is a general consensus in the development of schemes that satisfy the DGCL, in particular for FSI problems (Lesoinne and Farhat, 1996; Nobile, 2001; Mavriplis and Yang, 2005; Ahn and Kallinderis, 2006). A straightforward way to satisfy the DGCL is to use a time integration rule with degree of precision $n_d \cdot s - 1$, where n_d is the spatial dimension and s is the order of the polynomial used to represent the time evolution of the

nodal displacement within each time step (See Eq.(2.34)). For example, in 3D problems with a linear in time reconstruction a rule with degree of precision 2 should be used. Alternatively, the methodology proposed by Farhat and Geuzaine (2004) to obtain an ALE extension for a given time-integrator in fixed meshes, could be used. In this work a new methodology, which is based on averaged ALE Jacobians is proposed to obtain DGCL compliant FEM formulations. It is applied to the θ-family of time integration methods in general nonlinear advective-diffusive problems. In addition, an extension to the three-point BDF is given. In a previous work (Farhat and Geuzaine, 2004) averaged coefficients are obtained by starting with a general integration scheme with a series of unknown parameters, which are then adjusted in order to preserve DGCL compliance, and the temporal accuracy of the fixed mesh counterpart. In contrast, in this work the geometric coefficients are obtained by averaging them over the time step, so that precision is preserved and the DGCL is satisfied in a natural way.

To validate the AJF a set of numerical tests are performed. This includes 2D/3D diffusion problems on moving meshes and 2D compressible Navier-Stokes equations.

4.2 Average Jacobian Formulation

A discrete formulation is said to satisfy the DGCL condition if it solves exactly a constant state regime, i.e. not depending on space or time, for a general mesh movement $\mathbf{x}(\boldsymbol{\xi}, t)$. As was mentioned in §4.1 the effect of the DGCL in the precision and numerical stability of the scheme is an open discussion, but in several works (Guillard and Farhat, 2000; Formaggia and Nobile, 2004) it is recommended to employ numerical schemes that satisfy the DGCL. This may help in improve the precision and the stability.

By replacing U_j = constant in Eq.(2.26) and after some manipulations it can be shown that the DGCL is satisfied if

$$\int_{\Omega^{n+1}} w \, \mathrm{d}\Omega - \int_{\Omega^n} w \, \mathrm{d}\Omega = \Delta t \int_{\Omega^{n+\theta}} v_k^* \, w_{,k} \, \mathrm{d}\Omega. \tag{4.1}$$

A similar restriction holds for the boundary term. The stabilization term $S(w,U)$ normally satisfies automatically the DGCL since it involves gradients of the state, and then it is null for a constant state.

Note that this previous equation holds if the right hand side is evaluated as an integral instead of being evaluated at $t^{n+\theta}$, i.e. the DGCL error comes from the approximation that was made in (2.32), i.e. it is always true that

$$\int_{\Omega^{n+1}} w \,\mathrm{d}\Omega - \int_{\Omega^n} w \,\mathrm{d}\Omega = \int_{t^n}^{t^{n+1}} \left\{ \int_{\Omega^t} v_k^* \, w_{,k} \,\mathrm{d}\Omega \right\} \mathrm{d}t. \tag{4.2}$$

Consider the integrand in the right hand side. Transforming to the reference domain Ω^ξ we obtain

$$\begin{aligned}
\int_{t^n}^{t^{n+1}} \left\{ \int_{\Omega^t} v_k^* \, w_{,k} \,\mathrm{d}\Omega \right\} \mathrm{d}t &= \int_{t^n}^{t^{n+1}} \left\{ \int_{\Omega^\xi} v_k^* \frac{\partial w}{\partial \xi_l} \frac{\partial \xi_l}{\partial x_k} J \;\mathrm{d}\Omega^\xi \right\} \mathrm{d}t, \\
&= \int_{\Omega^\xi} v_k^* \frac{\partial w}{\partial \xi_l} \int_{t^n}^{t^{n+1}} \left(\frac{\partial \xi_l}{\partial x_k} J \right)^t \mathrm{d}t \;\mathrm{d}\Omega^\xi, \\
&= \int_{\Omega^\xi} v_k^* g_k^{n+\theta} J^{n+\theta} \;\mathrm{d}\Omega^\xi, \\
&= \int_{\Omega^{n+\theta}} v_k^* g_k^{n+\theta} \;\mathrm{d}\Omega,
\end{aligned} \tag{4.3}$$

where g_k is an *averaged interpolation function gradient* and θ is the parameter of the trapezoidal time integrator.

$$\begin{aligned}
g_k^{n+\theta} &= (J^{n+\theta})^{-1} \bar{Q}_{lk}^{n+1/2} \frac{\partial w}{\partial \xi_l}, \\
\bar{Q}_{lk}^{n+1/2} &= \int_{t^n}^{t^{n+1}} Q_{lk}^t \,\mathrm{d}t, \\
Q_{lk}^t &= \left(J \frac{\partial \xi_l}{\partial x_k} \right)^t.
\end{aligned} \tag{4.4}$$

The proposed scheme is then to replace the $A(w,U^{n+\theta})$ operator in (2.22) by

$$A^{\mathrm{GCL}}(w,U^{n+\theta}) = -\int_{\Omega^{n+\theta}} \left[\mathcal{F}_{jk}^c - v_k^* U_j - \mathcal{F}_{jk}^d \right]\Big|_{t^{n+\theta}} \; g_k^{n+\theta} \,\mathrm{d}\Omega, \tag{4.5}$$

A similar modification must be introduced in the boundary term $B(w,U)$, this will be explained later in Section §4.2.2 . It is easy to check that with this modification the scheme is DGCL compliant for all θ.

4.2.1 Evaluation of the average interpolation function gradient

Due to (2.34) each component x_k is a linear function of time inside the time step, then the spatial derivatives $(\partial x_k/\partial \xi_l)$ are also linear functions, and the determinant J is a polynomial of degree n_d. Also, the components of the inverse transformation $\boldsymbol{\xi} \rightarrow \mathbf{x}$ can be determined from the inverse of the direct transformation $\mathbf{x} \rightarrow \boldsymbol{\xi}$ as

$$\begin{aligned} \frac{\partial \xi_l}{\partial x_k} &= \left(\frac{\partial \mathbf{x}}{\partial \boldsymbol{\xi}}\right)^{-1}_{lk}, \\ J\frac{\partial \xi_l}{\partial x_k} &= (-1)^{k+l}\,\text{minor}\left(\frac{\partial \mathbf{x}}{\partial \boldsymbol{\xi}}\right)_{kl}, \end{aligned} \tag{4.6}$$

where $\text{minor}(\mathbf{A})_{ij}$ is the determinant of the submatrix of $\mathbf{A}$ when row i and column j have been eliminated. Then, the minors are polynomials of order $n_d - 1$ and so are the entries of $J\frac{\partial \xi_l}{\partial x_k}$ that are the integrands in (4.4).

As a check, well known results about the compliance of the DGCL with the trapezoidal rule will be verified. The DGCL is satisfied if the integration rule used to approximate the time integral in (4.4) is exact, for instance $\theta = 1/2$ satisfies the DGCL in 2D, since the integrand is linear and the trapezoidal rule reduces to the midpoint rule. In addition, DGCL is satisfied in 1D for any $0 \leq \theta \leq 1$, and for none in 3D. The point is that using $\theta = 1/2$ (Crank-Nicolson) is restrictive, and there is no θ that satisfies the DGCL in 3D. To overcome these inconveniences a high order time integration methodology is proposed for (4.4), hence the DGCL is satisfied for an arbitrary θ in any dimension. The method can be extended easily to other temporal integration schemes (see Section §4.3).

For instance, the Gauss integration method can be used. Normally the Jacobians and determinants are known at t^n and t^{n+1} since they are needed for

the computation of the temporal term (the right hand side in (2.32)), so perhaps it is better to use the Gauss-Lobatto version which includes the extremes of the interval. The Gauss-Lobatto method integrates exactly polynomials of up to degree $2n-3$ where n is the number of integration points, so that it suffices to use the extreme points for simplices in $n_d = 2$ and to add a point at the center of the interval for $n_d = 3$, i.e.

$$g_k^{n+\theta} = \begin{cases} \dfrac{\Delta t}{2J^{n+\theta}} \left[Q_{lk}^n + Q_{lk}^{n+1} \right] \dfrac{\partial w}{\partial \xi_l}, & \text{in 2D,} \\ \dfrac{\Delta t}{6J^{n+\theta}} \left[Q_{lk}^n + 4Q_{lk}^{n+1/2} + Q_{lk}^{n+1} \right] \dfrac{\partial w}{\partial \xi_l}, & \text{in 3D,} \end{cases} \tag{4.7}$$

being Q_{lk}^t defined in (4.4).

The implementation of the AJF only involves a few changes at the elemental routine level and the added cost is negligible. This is a key point in the presented methodology.

4.2.2 The boundary term

The boundary term in (2.22) can be brought to the reference domain as follows

$$\begin{aligned} B(w,U) &= \int_{\partial\Gamma^t} \left[\mathcal{F}_{jk}^c - v_k^* U_j - \mathcal{F}_{jk}^d \right] w n_k \, \mathrm{d}\Gamma, \\ &= \int_{\partial\Gamma^\xi} \left[\mathcal{F}_{jk}^c - v_k^* U_j - \mathcal{F}_{jk}^d \right] w n_k J_\Gamma \, \mathrm{d}\Gamma^\xi, \end{aligned} \tag{4.8}$$

where J_Γ is the Jacobian of the transformation between a surface element in Γ^t and Γ^ξ. The DGCL is satisfied if the averaged normal vector is used, i.e.

$$\begin{aligned} B^{\mathrm{GCL}}(w,U) &= \int_{\partial\Gamma^t} \left[\mathcal{F}_{jk}^c - v_k^* U_j - \mathcal{F}_{jk}^d \right] w \bar{n}_k \, \mathrm{d}\Gamma, \\ \bar{n}_k &= \frac{1}{J_\Gamma^\theta} \eta_k, \\ \eta_k &= \frac{1}{\Delta t} \int_{t^n}^{t^{n+1}} n_k J_\Gamma \, \mathrm{d}t. \end{aligned} \tag{4.9}$$

Regarding the evaluation of the integral for computing η_k, the considerations

are very similar to those given in §4.2.1. The components of $n_k J_\Gamma$ are also polynomials of degree $n_d - 1$ in time. For instance in 3D, if $\mathbf{x}_1, \mathbf{x}_2, \mathbf{x}_3$ are the nodes at the vertices of a triangle element (ordered counter-clockwise when viewed from the exterior of the fluid) on the surface Γ^t, then

$$\mathbf{n} J_\Gamma = \frac{(\mathbf{x}_2 - \mathbf{x}_1) \times (\mathbf{x}_3 - \mathbf{x}_1)}{2|\Gamma^\xi|}, \tag{4.10}$$

where $\times$ denotes the vector cross product and $|\Gamma^\xi|$ is the area of the triangle in the reference coordinates. As the coordinates of the nodes are linear in time and $|\Gamma^\xi|$ is constant, the components of $n_k J_\Gamma$ are quadratic polynomials.

Then, the considerations about the number of points for the Gauss-Lobatto integration are the same as discussed before, i.e. two integration points are enough to compute the integral in (4.9), and three are needed in 3D.

4.3 Application to the Backward difference formula

The Backward Differentiation Formula is another popular method for the integration of the system of ordinary differential equations (Boffi and Gastaldi, 2004; Formaggia and Nobile, 2004; Ascher, 2008). Applied to (2.21) gives

$$\frac{1}{\Delta t}\left(\tfrac{3}{2} H^{n+1} - 2H^n + \tfrac{1}{2} H^{n-1}\right) = F(w, U^{n+1}). \tag{4.11}$$

In order to apply the Averaged Jacobian Formulation, the right hand side of (4.11) must be rewritten as an integral over time. For this, note that, for any differentiable function $X(t)$ we have

$$\begin{aligned} \tfrac{3}{2} X^{n+1} - 2X^n + \tfrac{1}{2} X^{n-1} &= \tfrac{3}{2}(X^{n+1} - X^n) - \tfrac{1}{2}(X^n - X^{n-1}), \\ &= \tfrac{3}{2} \int_{t^n}^{t^{n+1}} \dot{X} \, \mathrm{d}t - \tfrac{1}{2} \int_{t^n - 1}^{t^n} \dot{X} \, \mathrm{d}t. \end{aligned} \tag{4.12}$$

If this relation is applied with the semidiscrete equations (2.21) with $X = H$

and $\dot{X} = -F$, then the following relation is obtained

$$\tfrac{3}{2}H^{n+1} - 2H^n + \tfrac{1}{2}H^{n-1} = -\tfrac{3}{2}\int_{t^n}^{t^{n+1}} F(w, U^{t'})\,\mathrm{d}t' + \tfrac{1}{2}\int_{t^{n-1}}^{t^n} F(w, U^{t'})\,\mathrm{d}t'. \tag{4.13}$$

The BDF integration method is obtained if the right hand side in (4.13) is replaced by the value of the integrand at t^{n+1}. The proposed method in order to satisfy the DGCL is to assume that the state in (4.13) remains constant ($U(t) = U^{n+1}$) but the geometric quantities v_k^* and $w_{,k}$ not, therefore these quantities must be averaged over time and some additional terms must be computed, so that

$$\tfrac{3}{2}H^{n+1} - 2H^n + \tfrac{1}{2}H^{n-1} = -\Delta t F^{\mathrm{BDF}}(w, U^{n+1}), \tag{4.14}$$

where

$$\begin{aligned}
F^{\mathrm{BDF}}(w, U^{n+1}) &= A^{\mathrm{BDF}}(w, U^{n+1}) + B^{\mathrm{BDF}}(w, U^{n+1}) + S(w, U^{n+1}),\\
A^{\mathrm{BDF}}(w, U^{n+1}) &= -\int_{\Omega^{n+1}} \left[(\mathcal{F}^c_{jk} - \mathcal{F}^d_{jk})^{n+1} g_k^{n+1} - U_j^{n+1} r^{n+1}\right]\,\mathrm{d}\Omega,\\
B^{\mathrm{BDF}}(w, U^{n+1}) &= \int_{\partial\Gamma^t} \left[(\mathcal{F}^c_{jk} - \mathcal{F}^d_{jk})\beta_k^{n+1} - U_j^{n+1} s^{n+1}\right] w\,\mathrm{d}\Gamma,
\end{aligned} \tag{4.15}$$

and g_k, r, β_k, and s are time averaged geometric quantities given by

$$\begin{aligned}
g_k^{n+1} &= \frac{1}{J^{n+1}}\left(\tfrac{3}{2}Q_{lk}^{n+\frac{1}{2}} - \tfrac{1}{2}Q_{lk}^{n-\frac{1}{2}}\right)\frac{\partial w}{\partial \xi_l},\\
r^{n+1} &= \frac{1}{J^{n+1}}\left(\tfrac{3}{2}Q_{lk}^{n+\frac{1}{2}}\, v_k^{*n+\frac{1}{2}} - \tfrac{1}{2}Q_{lk}^{n-\frac{1}{2}}\, v_k^{*n-\frac{1}{2}}\right)\frac{\partial w}{\partial \xi_l},\\
\beta_k^{n+1} &= \frac{1}{J_\Gamma^{n+1}}(\tfrac{3}{2}\eta_k^{n+\frac{1}{2}} - \tfrac{1}{2}\eta_k^{n-\frac{1}{2}}),\\
s^{n+1} &= \frac{1}{J_\Gamma^{n+1}}(\tfrac{3}{2}\eta_k^{n+\frac{1}{2}} v_k^{*n+\frac{1}{2}} - \tfrac{1}{2}\eta_k^{n-\frac{1}{2}} v_k^{*n-\frac{1}{2}}),\\
\eta_k^{n+\frac{1}{2}} &= \frac{1}{\Delta t}\int_{t^n}^{t^{n+1}} n_k J_\Gamma\,\mathrm{d}t,
\end{aligned} \tag{4.16}$$

and $v_k^{*n+\frac{1}{2}}$ is the (constant) velocity in time step $[t^n, t^{n+1}]$. Regarding the computation of the averaged Jacobians $Q_{lk}^{n+\frac{1}{2}}$ and $\eta_k^{n+\frac{1}{2}}$ the rules are the same

as before ((4.4),(4.9)), since their entries are polynomials of degree $n_d - 1$ within the time interval.

Chapter 5

Numerical simulations

The aim of this chapter is to expose the FSI simulations that have been carried out using the partitioned coupling algorithm implemented in PETSc-FEM, with the AJF formulation presented in the previous chapter. But, first are performed a set of validation tests for the fluid solver and the structural solver, which are the foundations of the partitioned algorithm. Then, and in order to check the coupling algorithm, a problem named the piston problem is solved, where the energy conservation and the convergence of the stage loop are analyzed. Also, a set of numerical tests in 2D and 3D are performed in order to establish the introduced error when the ALE formulation is not DGCL compliant. Finally, the interaction between the fluid and the structure during the start-up process of a rocket engine nozzle is carried out.

5.1 Fluid solver test

The compressible Navier-Stokes solver implemented in PETSc-FEM has been widely used and validated in the following works Paz (2006); Langhi (2007); Ríos Rodriguez (2009). In this section the solver is tested with the solution of a NACA0012 airfoil in a transonic flow. This test case has been widely used in the validation of numerical method (Tang and Hafez, 2001; Dadone and Grossman, 2003; Nejat and Ollivier-Gooch, 2008), because it presents a shock wave in the upper surface testing in particular the effect of the stabilization

techniques.

The domain is shown in Figure (5.1) and is discretized using an unstructured mesh of 17800 triangular elements, setting the airfoil to 4° of angle of attack. The fluid is assumed inviscid with a specific heat ratio $\gamma = 1.4$, a thermodynamic constant $R = 287$ [J/kgK] and the following reference conditions, $\rho_\infty = 1.225$ [kg/m^3], $p_\infty = 101325$ [Pa] and $M_\infty = 0.75$.

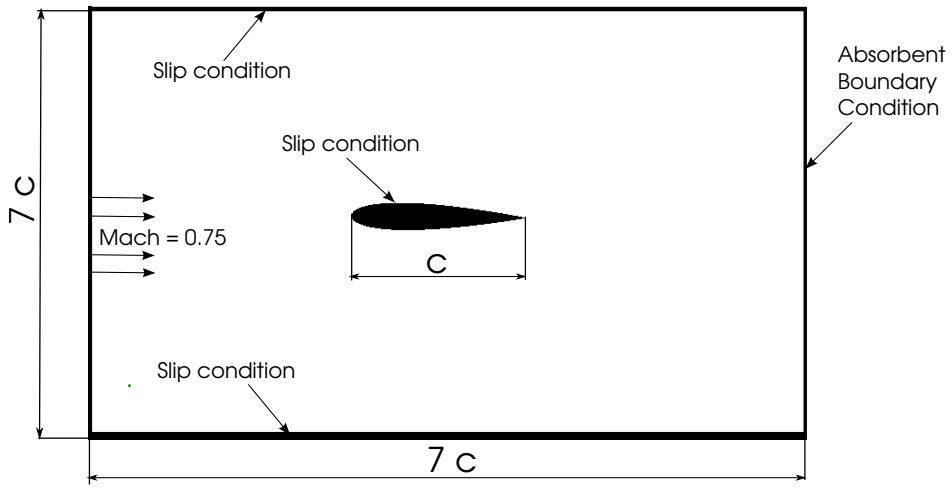

Figure 5.1: Domain and boudanry conditions.

In order to avoid numerical instabilities in the region of the shock wave the SUPG and SC stabilization techniques are used. The results obtained with PETSc-FEM are compared with that obtained by Romanelli and Serioli (2008); Romanelli et al. (2008) using OpenFOAM (OpenFOAM, 2011) and FLUENT®. In Figure (5.2) the pressure coefficient (Cp), which is computed as

$$\mathrm{Cp} = \frac{2}{\gamma \mathrm{M}_\infty^2} \left(\frac{\mathrm{p}}{\mathrm{p}_\infty} - 1 \right), \tag{5.1}$$

is plotted together with data from the above references. As can be seen, a good correlation between the solvers is found. The use of SUPG and SC avoids numerical instabilities in the shock wave region, achieving a good resolution of this feature.

In Figure (5.3) colormaps of pressure and Mach distribution around the airfoil is shown.

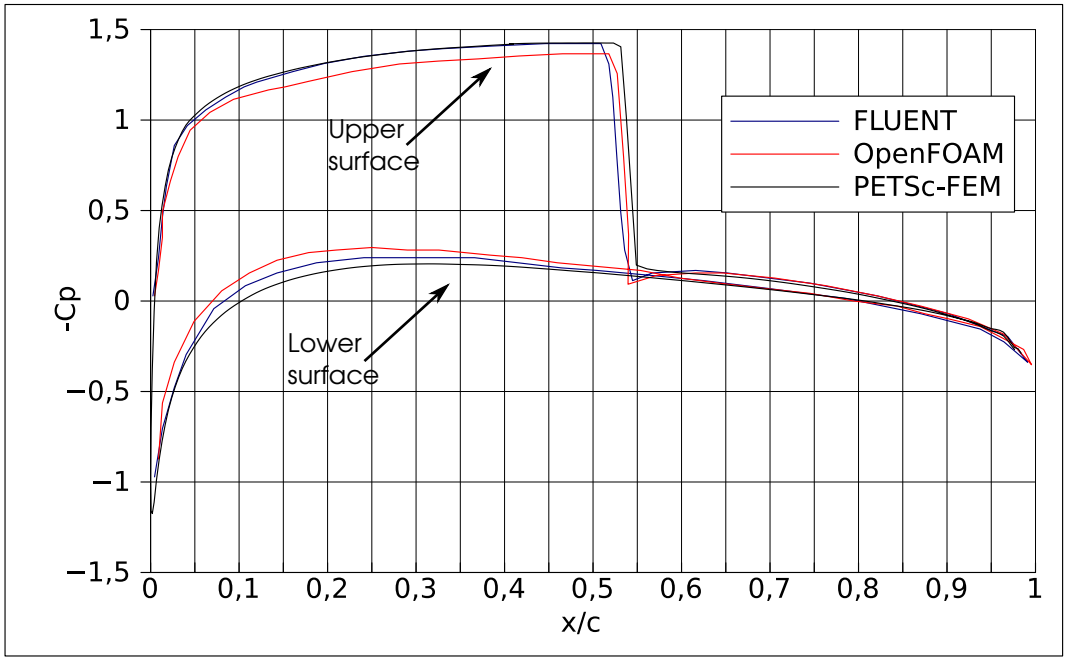

Figure 5.2: Pressure coefficient of the upper and lower surface of the NACA 0012.

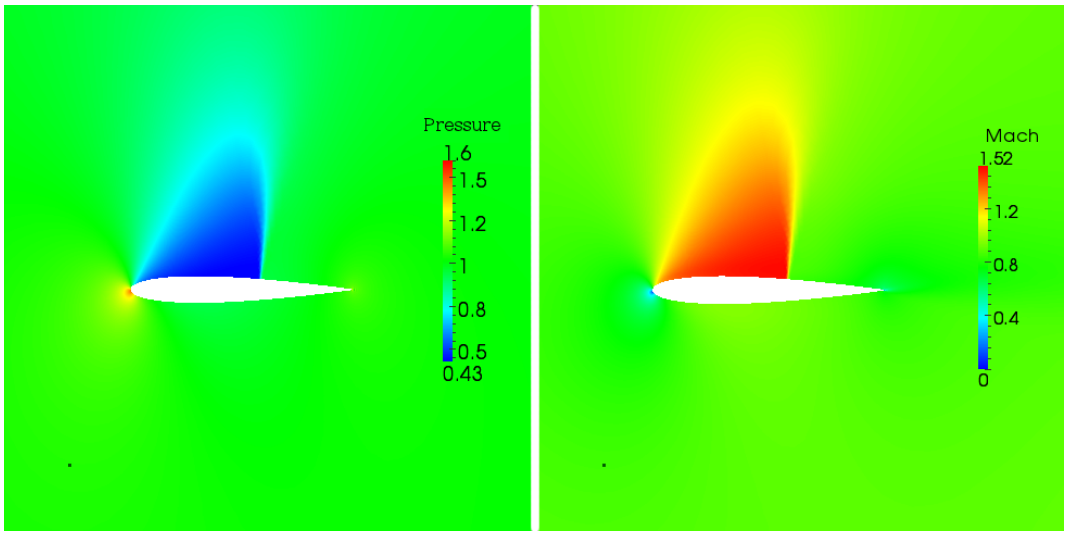

Figure 5.3: Colormaps of pressure and Mach distributions.

Having performed a test for the fluid, the next step is to validate the structural solver for both, dynamic and static cases.

5.2 Structural solver test

In this section is carried out the validation of the structural solver, using both static and dynamic cases. The static case consists on the large amplitude deflection of a 3D cantilevered beam and the dynamic case consists on solving the large amplitude vibration of the beam. These test cases has been used also by Tuković and Jasak (2007) in order to validate a Finite Volume solver for large deformation. The beam is clamped at $z = 0$ and subjected to an applied traction force t at $z = 2$. The beam has the dimensions shown in Figure (5.4) and is discretized with a structured tetrahedral mesh.

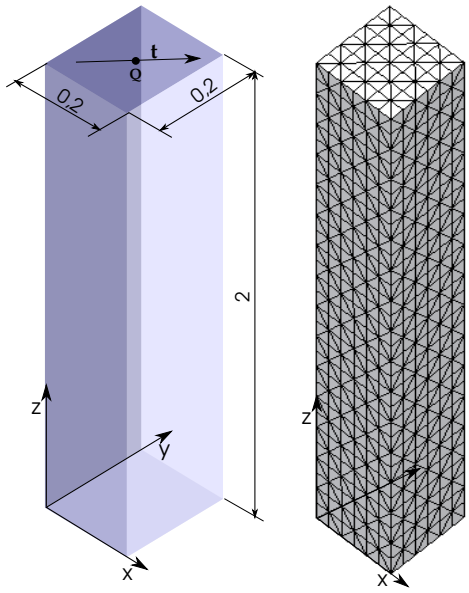

Figure 5.4: Dimensions of the 3D cantilever beam.

The density ρ_s and the modulus of elasticity E are selected in such a way to obtain the first natural frequency of the beam equal to $f_1 = 1\ [Hz]$

$$f_1 = \frac{1.875^2}{2\pi}\sqrt{\frac{\mathrm{EI}}{\rho_s A L^4}}. \tag{5.2}$$

The physical and geometrical properties of the beam are listed in Table (5.1).

For the static case, the equilibrium shape of the beam is obtained for different traction forces $\mathbf{t} = (\frac{|\mathbf{t}|}{\sqrt{2}}; \frac{|\mathbf{t}|}{\sqrt{2}}; 0)[\mathrm{N/m^2}]$, which is represented by the

Table 5.1: Physical and Geometrical properties of the beam

E	ρ_s	ν	A	I
15.293 [MPa]	1000 [kg/m^3]	0.3	0.4[m^2]	0.0001333[m^4]

following dimensionless parameter

$$\mathcal{T} = \frac{|\mathbf{t}|AL^2}{\mathrm{EI}}. \tag{5.3}$$

The computed displacements of the point Q

$$d_Q = \sqrt{u_x^2 + u_y^2}. \tag{5.4}$$

are compared with the results of Mattiasson (1981), where exact deflections d_{exact} of the point Q are computed by means of the numerical evaluation of elliptic integrals. The problem is solved for three different meshes ($4 \times 4 \times 20; 8 \times 8 \times 40; 16 \times 16 \times 80$), each one having a element mesh size of a half of the previous one.

Table 5.2: Deflection for different loads and meshes

$\mathcal{T}$	$d_{Q,4\times20}$	$d_{Q,8\times40}$	$d_{Q,16\times80}$	d_{exact}	Converg (p)
0.2	0.099	0.121	0.129	0.133	1.91
0.4	0.196	0.239	0.254	0.262	1.95
0.8	0.376	0.455	0.481	0.499	2.01
1.6	0.678	0.787	0.833	0.859	1.76

In Table (5.2) are listed the displacements of the point Q for different loads and meshes. Also, it is shown the reference value and a mesh convergence analysis which gives a second-order mesh convergence.

As example, the convergence for the first cases is shown. It is compute as

$$\begin{aligned} \mathrm{p} &= \frac{\log(\mathrm{e}_1/\mathrm{e}_2)}{\log(\mathrm{h}_1/\mathrm{h}_2)} \\ &= \frac{\log\left(\frac{0.129-0.099}{0.129}/\frac{0.129-0.121}{0.129}\right)}{\log(\frac{0.075}{0.0375})} = 1.91 \end{aligned} \tag{5.5}$$

In the next test, the dynamic response of the 3D cantilever beam to a suddenly applied traction force is analyzed. In the numerical model no damping effect exists, so it can be considered as an elastic system, expecting an undamped vibration of the beam about its static equilibrium. The transient simulation is performed on the intermediate computational mesh ($8 \times 8 \times 40$) and time step size is 0.002 [s] corresponding to a maximum Courant number Co around 10, where $\mathrm{Co} = c_s \Delta t/h$ and h is the minimum element dimension, and $c_s = \sqrt{\mathrm{E}/\rho_\mathrm{s}}$ is the solid wave speed. The Newmark-β time integration method described in section §2.2 is used, setting $\beta_n = 1/4$ and $\gamma_n = 1/2$. As solution is reported the deflection of the Q point as function of time and are compared with the results obtained by Tuković and Jasak (2007).

We note in Figure (5.6) that the amplitude of the vibration is well preserved while maintaining a vibration frequency close to the first natural frequency. Also as expected, the frequency increases with the amplitude of the vibrations due to a nonlinear geometric stiffness. The convergence history if the L_2 norm of the residual for the Newton iteration is shown in Figure (5.7).

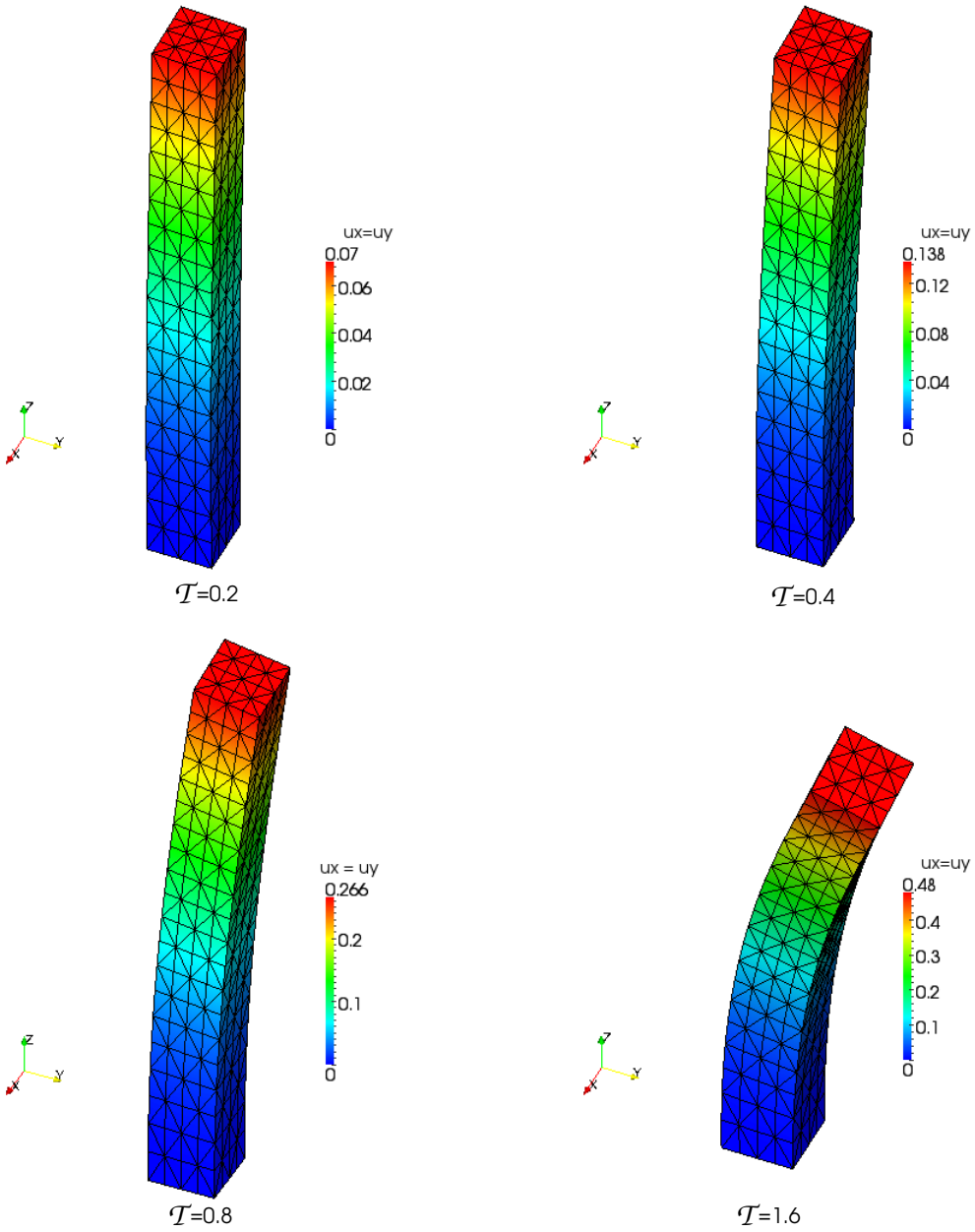

Figure 5.5: Deflection of the 3D cantilever beam for different traction forces.

5.3 Coupling test problem

As mentioned in previous sections, the solution of FSI problems using specialized existing codes involves the implementation of a coupling algorithm. The

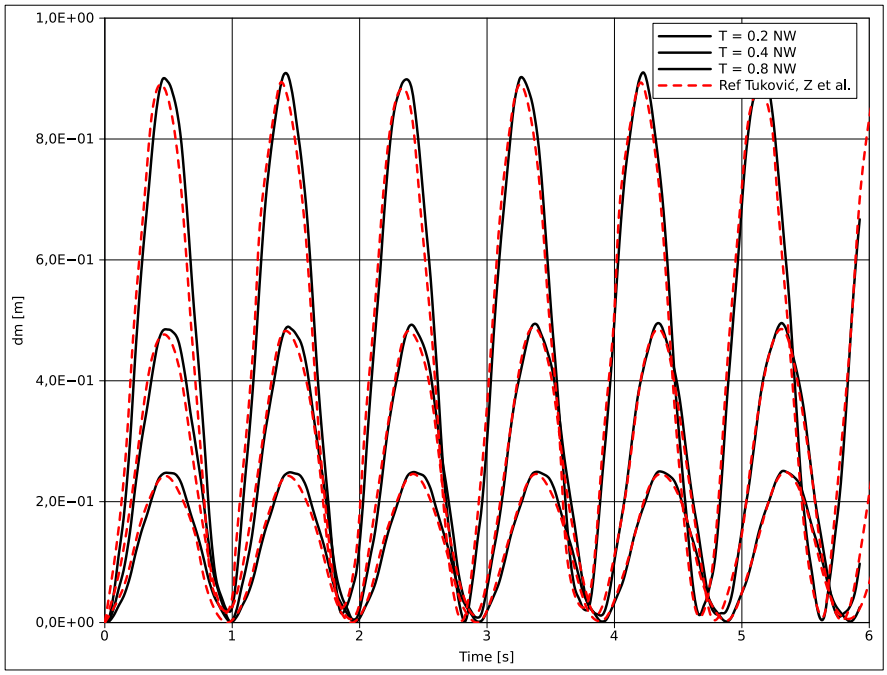

Figure 5.6: Displacement of the Q point.

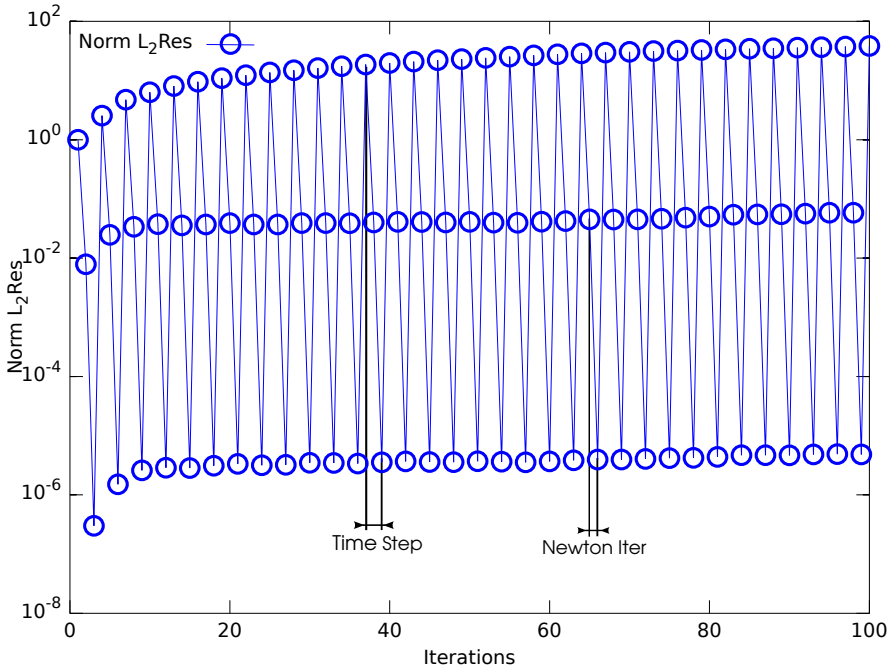

Figure 5.7: Norm L_2 of the Newton iteration residual.

coupling scheme has its particularities and it is important to have a good understanding about the algorithm to carry out reliable simulations.

As was stated in section §3.3, a disadvantage of the partitioned coupling is its inherent loss of the conservative properties of the continuum fluid-structure system and only satisfies conservation in an asymptotic way. This loss of the conservative properties can be improved using predictors or stages and if the staged loop converges, it does to the monolithic solution.

In order to prove the accuracy of the implemented coupling scheme an example problem known as the piston problem will be solved. This test problem has been used is several works, like in Piperno (1995) and Michler et al. (2003, 2004). It is a very simple problem from the computational point of view and it allows to evaluate all the characteristics of the coupling algorithm. In the continuum problem the unique source of energy dissipation is the damping of the structure, so if the structural damping is negligible, the system is stable and the global energy must be conserved. This is one of the key points to be analyzed because it is directly related with the coupling scheme and the time integration methods used in the discrete problem.

In Figure (5.8) we can see a sketch of the problem, being the fluid inside the chamber described by the one-dimensional Euler equations ($\nu = 0$) for a compressible flow. This set of equations are closed by the state equation for a perfect gas and the compression process is assumed to be adiabatic, there are no exchanges between the fluid and its external environment. The chamber has a fixed wall and a movable wall of unitary area. In this problem the structure is described by a mass-spring system of one degree of freedom and the fluid and the structure exchange information trough a common interface.

Some conditions must be fulfilled at the interface of the discrete fluid-structure system, one dynamic and the other two kinematic. The dynamic condition states that the pressure at either side of the interface are the same.

$$p_f = p_s. \tag{5.6}$$

One of the kinematic condition states that the position of the moving wall is equal to its reference position plus the structural displacement and the other

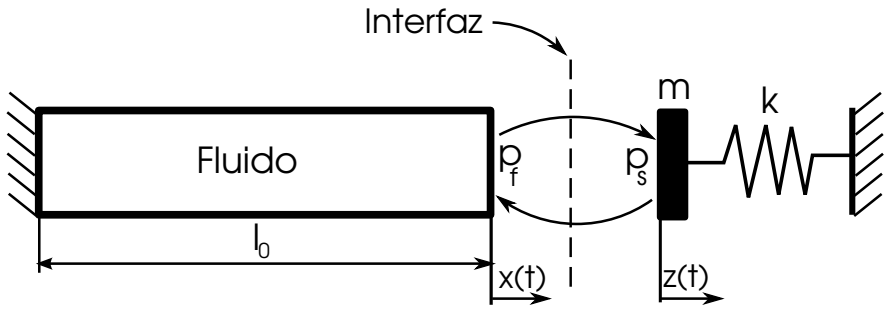

Figure 5.8: Sketch of the piston problem.

kinematic condition states equal velocity at the interface.

$$\begin{aligned} l_{(t)} &= l_0 + z_{(t)}, \\ u_{(t)} &= \dot{x}_{(t)} = \dot{z}_{(t)}. \end{aligned} \tag{5.7}$$

The fulfillment of these conditions are required in order to conserve mass, momentum and energy at the interface due to the fluxes must be the same at either side of the interface, and it can be expressed as:

$$\begin{aligned} &\rho(u - \dot{z}) = 0, \\ &\rho u(u - \dot{z}) + p_f = p_s, \\ &\rho e(u - \dot{z}) + u\ p_f = \dot{z}\ p_s. \end{aligned} \tag{5.8}$$

Now, some characteristics of the subsystems will be evaluated. The structural part is a mass-spring system which can be represented by the following equation

$$m\ddot{z} + kz = (p_s - p_0) \cdot A, \tag{5.9}$$

where m and k are the mass and stiffness of the system and p_s is the pressure exerted by the fluid and p_0 is a constant reference pressure and A is an unitary area of reference. The undamped angular frequency and characteristic time scale for this system are

$$\begin{aligned} w_s &= \sqrt{\frac{k}{m}}, \\ T_s &= \frac{2\pi}{w_s}. \end{aligned} \tag{5.10}$$

In the case of the fluid subsystem the characteristic time scale is given by

$$\begin{aligned} T_f &= \frac{2l_0}{c}, \\ c &= \sqrt{\frac{\gamma p_0}{\rho_0}}, \end{aligned} \tag{5.11}$$

and the relation between T_s/T_f determine how important are the transient effects on the fluid behavior. If $T_s \gg T_f$ the fluid can be considered as quasi-steady. Also, is important the mass ratio between the fluid and the structure

$$\zeta = \frac{\rho_0 l_0}{m}. \tag{5.12}$$

If $\zeta \ll 1$ the fluid mass can be neglected and only the structural mass is considered into the dynamic coupled system, but if $\zeta \approx \mathcal{O}(1)$ the fluid and structure masses has the same contribution to the dynamic coupled system.

The physical parameters used in the piston problem are listed in Table (5.3) and the ratio of characteristic times scale and masses are

Table 5.3: Parameters of the piston problem

m	k	T_s	ρ_0	p_0	T_f
0.8[kg]	7911[N/m]	0.063[s]	1.3[kg/m^3]	$10^5[Pa]$	0.0061[s]

$$\frac{T_s}{T_f} \approx 10, \quad \zeta \approx 1.63. \tag{5.13}$$

wherewith the fluid can be considered quasi-steady and its mass will impact on the oscillation frequency of the coupled system.

In order to estimate the oscillation frequency of the coupled system, we assume that the fluid behaves as a mass-spring system, adding a mass and stiffness to the structure system

$$(m + m_{fld})\ddot{z} + (k + k_{fld})z = 0, \tag{5.14}$$

where m_{fld} and k_{fld} are the mass and the stiffness added by the fluid. In

order to determine these parameters we use the hypotheses of quasi-steady flow, wherewith the fluid compression can be modeled as isentropic, where the volume of the chamber is proportional to the piston displacement

$$p = p_0 \left(\frac{V_0}{V}\right)^{\gamma} = p_0 \left(\frac{l_0}{l_0 + z}\right)^{\gamma}, \tag{5.15}$$

where γ is the ratio of specific heats. Eq.(5.15) can be linearized around $z_0 = 0$ for $z \ll l_0$

$$\begin{aligned} p &= p_0 - p_0\gamma \left(\frac{l_0}{l_0 + z}\right)^{\gamma-1} \frac{l_0}{(l_0 + z)^2}\bigg|_{z=0} (z - z0) + \mathcal{O}(\Delta z^2), \\ p &= p_0(1 - \frac{\gamma}{l_0}z) + \mathcal{O}(\Delta z^2), \\ p &\approx p_0(1 - \frac{\gamma}{l_0}z). \end{aligned} \tag{5.16}$$

Eq.(5.16) gives the variation of the chamber pressure due to a change in the length of the chamber. To obtain the stiffness added by the fluid k_{fld}, first the force is computed

$$F = pA = p_0(1 - \frac{\gamma}{l_0}z)A, \tag{5.17}$$

and then it is derived with respect to the displacement

$$k_{fld} = \frac{dF}{dz} = -\frac{p_0\gamma}{l_0}A. \tag{5.18}$$

The added mass term m_{fld} is computed as

$$\begin{aligned} m_{fld} &= \int_0^{l_0} \rho_0 \left(\frac{z}{l_0}\right)^2 A\mathrm{dz}, \\ m_{fld} &= \frac{1}{3}\rho_0 l_0 A. \end{aligned} \tag{5.19}$$

Thus the approximated oscillating frequency of the coupled system can be computed as

$$w_{fs} = \sqrt{\frac{k + k_{fld}}{m + m_{fld}}}, \tag{5.20}$$

and replacing with the corresponding values in the above equation the following values are obtained

$$w_{fs} = 346,3[\text{rad/s}] \ , \ T_{fs} = 0,0181[\text{s}]. \tag{5.21}$$

In the work of Michler et al. (2003) a coupled frequency of $w_{fs} = 342\ [rad/s]$ is obtained for the same parameters, which is in concordance with the frequency obtained in this work. Previously to carry out the analysis of the coupling algorithm, the structural solver is verified by comparing the oscillation frequency. This is done by imposing an initial displacement $z_{(t=0)} = 0.05$ and checking that the natural frequency matches with that computed using Eq.(5.10), which value is in Table (5.3). The problem was solved using two different time steps, in Case 1 $\Delta t_1 = 3.05 \cdot 10^{-4}[s]$ and in Case 2 $\Delta t_2 = 2.43 \cdot 10^{-3}[s]$ and the Newmark-β parameter are $\beta_n = 1/4$ and $\gamma_n = 1/2$.

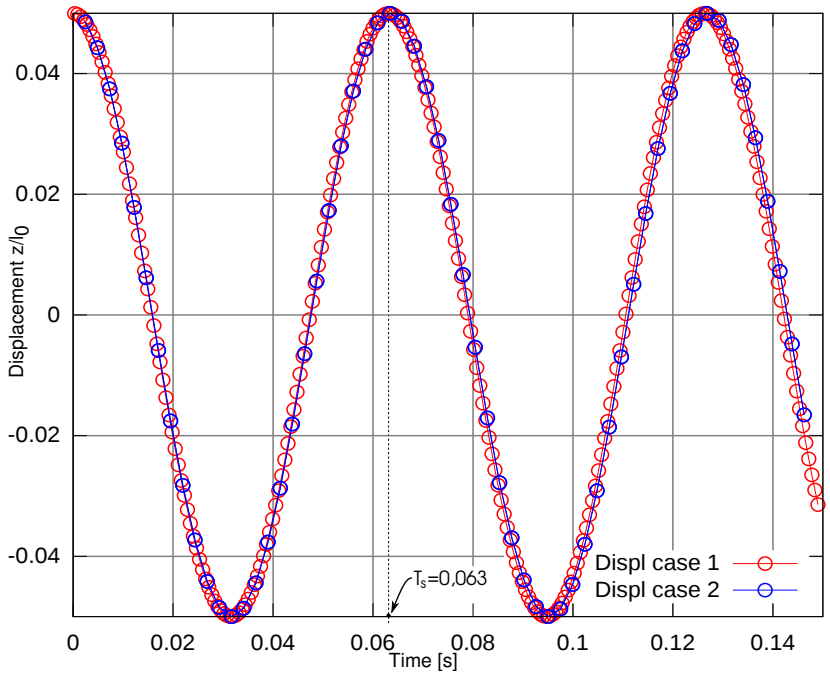

Figure 5.9: Structural displacement.

Having verified the structural solver, the coupled problem is solved using different values of α_0 and α_1 for the structural predictor and different Courant numbers. In these problems the structure initial conditions are $z_{(t=0)} = 0.05$

and $\dot{z}_{(t=0)} = 0$, and for the fluid the reference conditions stated in Table (5.3) are used to compute the initial conditions with a compression of $x_{(t=0)} = 0.05$.

In the first numerical test, the coupled problem is solved for Courant numbers in the range of $\text{Co} = \{0.5; 1; 2; 4\}$ without using structural predictors and for $\text{Co} = 1$ an oscillation period of the coupled problem is solved using 120 time steps. For the structure the Newmark-β parameter are $\beta_n = 1/4$ and $\gamma_n = 1/2$ and the fluid is solved using the Crank-Nicolson ($\theta = 0.5$) time integration method. This test allows to prove the issues corresponding to energy conservation treated in section §3.3.

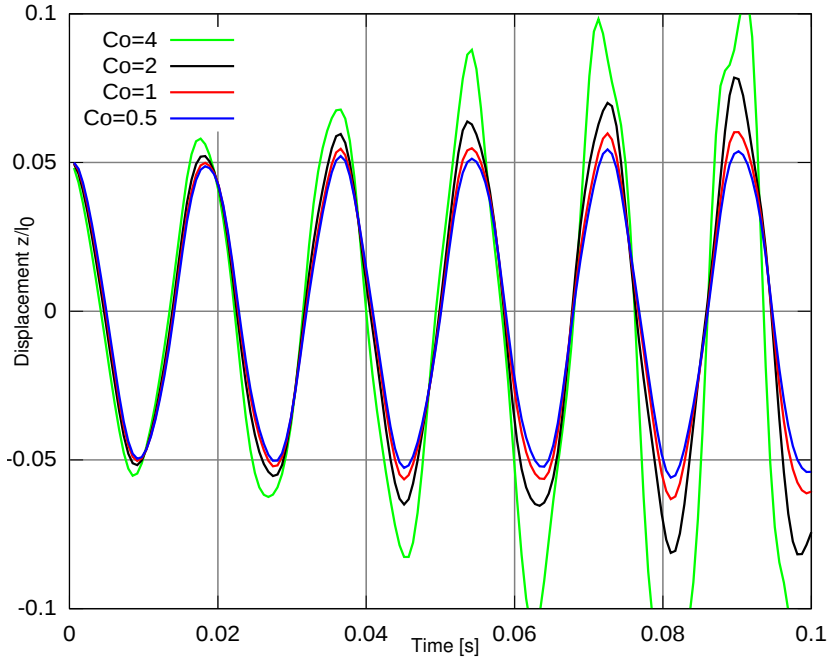

Figure 5.10: Structural displacement without predictor for $\text{Co} = \{0.5; 1; 2; 4\}$.

In Figure (5.10) it can be seen that the amplitude of the oscillation grows in time; this is because the energy of the system increases in time. In Figure (5.11) the structural total energy (Potential + Kinetic) is plotted versus time

$$E_T = \frac{1}{2} m \dot{z}^2 + \frac{1}{2} k z^2. \tag{5.22}$$

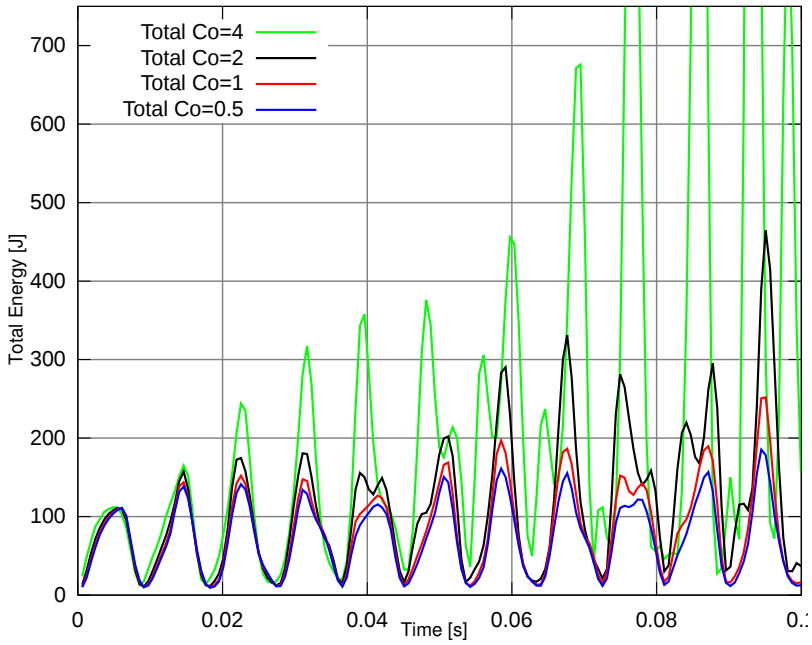

Figure 5.11: Structure total energy without predictor for Co $= \{0.5; 1; 2; 4\}$.

As an alternative, in order to avoid or decrease the fictitious energy added, the coupling algorithm can be supplied of an structural predictor, as that described by Eq.(3.1). Using $\alpha_0 = 1$ and $\alpha_1 = 0.5$ on Eq.(3.1) a second order predictor is obtained

$$\begin{aligned} \mathbf{z}_p^{(n+1)} &= \mathbf{z}^n + \alpha_0 \Delta t \dot{\mathbf{z}}^n + \alpha_1 \Delta t (\dot{\mathbf{z}}^n - \dot{\mathbf{z}}^{n-1}), \\ \mathbf{z}_p^{(n+1)} &= \mathbf{z}^n + \Delta t \dot{\mathbf{z}}^n + \frac{1}{2} \Delta t (\dot{\mathbf{z}}^n - \dot{\mathbf{z}}^{n-1}). \end{aligned} \tag{5.23}$$

The displacements obtained using a second order predictor are shown in Figure (5.12). The artificial energy added is significantly reduced and for Co $= 1$ and Co $= 0.5$ the solutions are very close to each other.

The total energy for the structure for different Courant numbers is shown in Figure (5.12) and it can be seen that the energy does not grow indefinitely as in the previous case.

Now, with the aim to improve the stability of the scheme, an inner loop is added to the algorithm, known as a ‘‘stage’’ loop. If the stage loop converges, then a strongly coupled algorithm is obtained (See Figure (3.3)). The stage

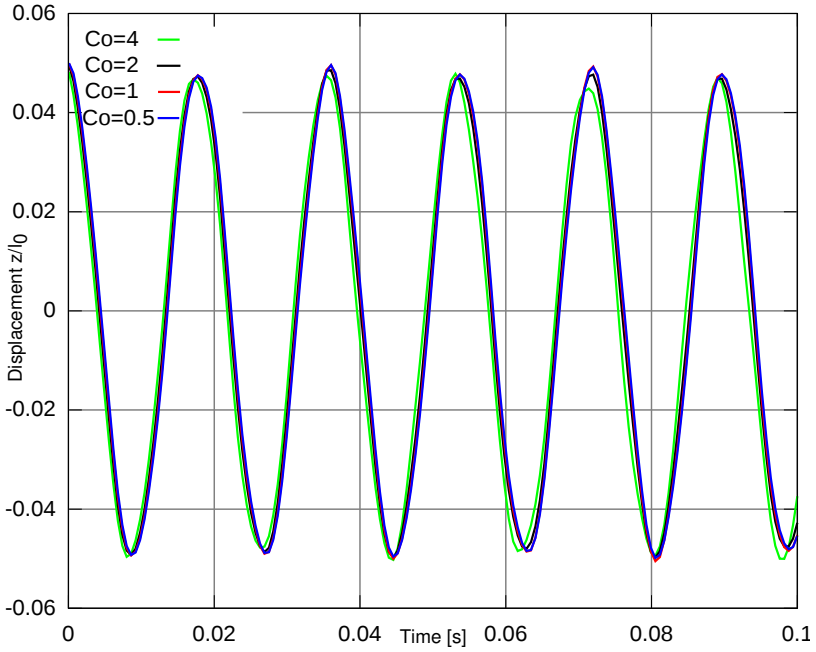

Figure 5.12: Structural displacement with second order predictor for Co = $\{0.5; 1; 2; 4\}$.

loop increases the computational costs almost proportional to the number of stages, but in cases of strong coupling between fluid and structure, the use of predictors are not enough to obtain a stable system. In Figure (5.14) the mass displacement for Co = 2 without structural predictor is plotted. With $n_{stage} = 1$ the displacement grows in time due to an energy increase in the system as it can be observed in Figure (5.11), but when $n_{stage} > 1$ the system becames stable.

If the stage loop is also used with the structural predictor, the number of stages needed to reach a residual error are less than if no structural predictor is used. The stage loop can be viewed as a fixed point iteration scheme over the variables of both fluid and structure systems, so if the sequence converges, the rate of convergence of the stage loop is only linear. In Figure (5.16) the scaled convergence of fluid state on the stage loop are plotted (i.e $||\mathbf{U}^{n+1,i+1} - \mathbf{U}^{n+1,i}||/||\mathbf{U}^{0,1} - \mathbf{U}^{0,0}||$) with and without the use of structural predictor. As was previously mentioned, the stage loop shows a linear convergence and better final convergence is obtained when using a structural predictor.

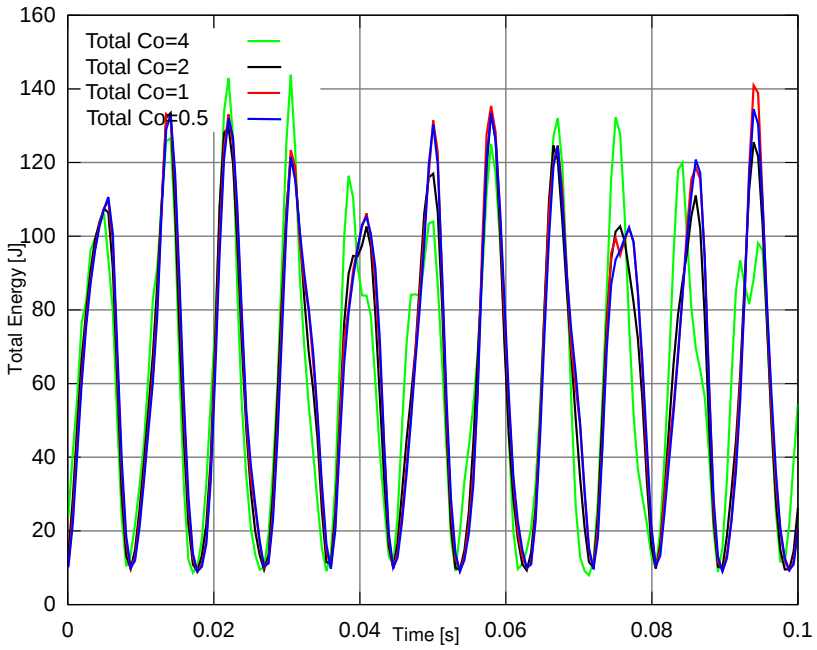

Figure 5.13: Structure total energy with second order predictor for Co = $\{0.5; 1; 2; 4\}$.

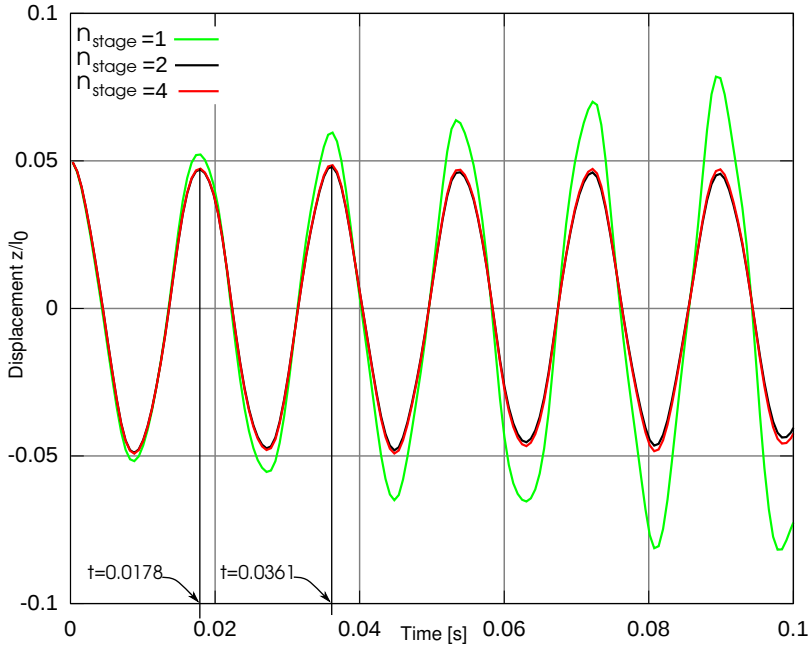

Figure 5.14: Structural displacement without predictor for Co = 2 using stages.

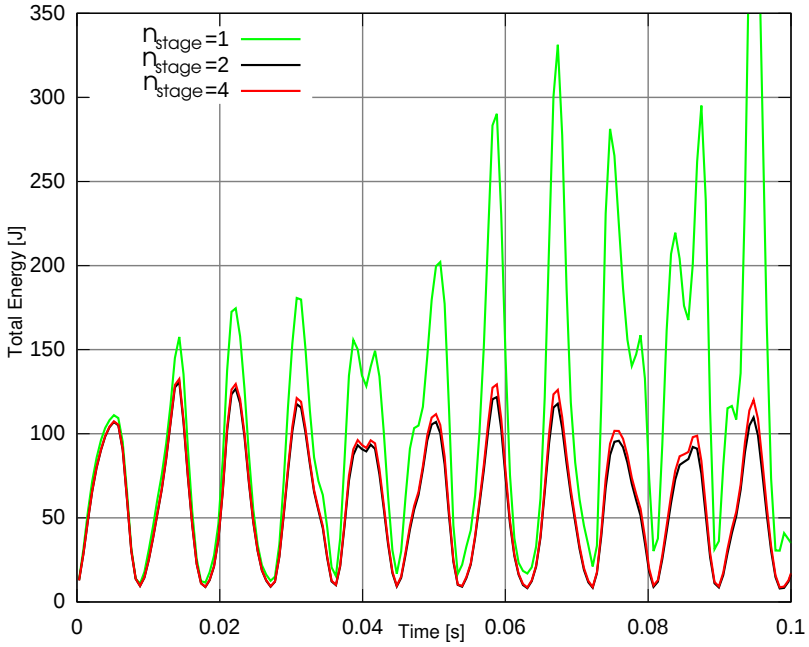

Figure 5.15: Structure total energy without predictor for Co = 2 using stages.

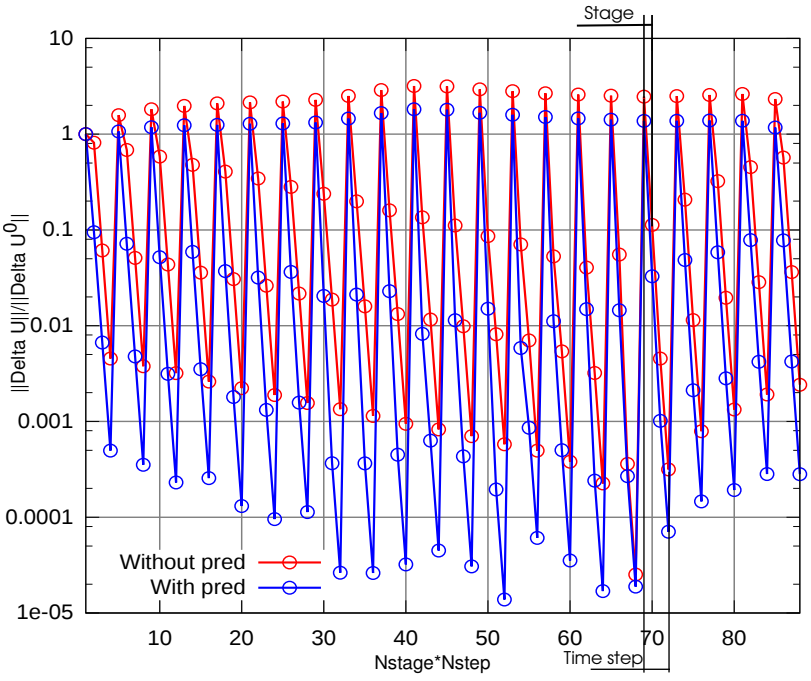

Figure 5.16: Fluid state convergence for Co = 2 using $n_{stage} = 4$.

In the same way, in Figure (5.17) the scaled convergence of structure state on the stage loop (i.e $||\mathbf{z}^{n+1,i+1} - \mathbf{z}^{n+1,i}||/||\mathbf{z}^{0,1} - \mathbf{z}^{0,0}||$) with and without the use of structural predictor are plotted.

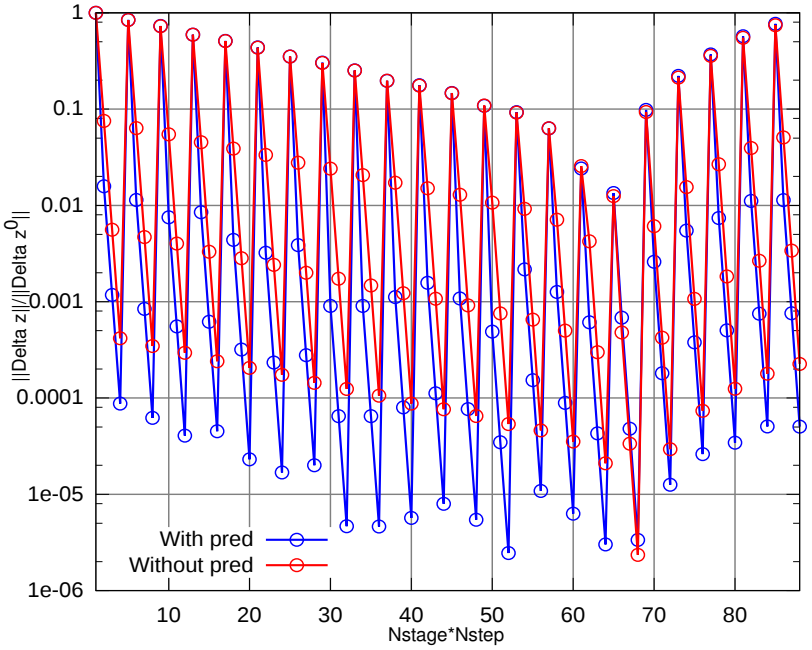

Figure 5.17: Structure state convergence for Co = 2 using $n_{stage} = 4$.

5.4 Validation of the Averaged Jacobian Formulation

In this section a set of numerical tests are performed in order to validate the Averaged Jacobian Formulation (AJF) proposed in section §4.2 in order to satisfy the DGCL. These tests consist in imposing the movement of the nodes by some law, in both 2D and 3D, and verifying that it satisfies the DGCL, which states that the numerical method must be able to reproduce a constant solution on a moving domain (See section §4.1).

5.4.1 Validation for 2D scalar diffusion problem with internal node movement

For the sake of clarity, let us consider, the scalar diffusion version of equation (2.1).

$$\begin{aligned} \frac{\partial u}{\partial t} - \mu \Delta u = 0 \quad & \text{for } \mathbf{x} \in \Omega^{\mathrm{t}},\ \mathrm{t} \in (0, \mathrm{T}] \\ u = u_0 \quad & \text{for } \mathbf{x} \in \Omega^{0},\ \mathrm{t} = 0 \\ u = u_\Gamma \quad & \text{for } \mathbf{x} \in \Gamma^{\mathrm{t}},\ \mathrm{t} \in [0, \mathrm{T}] \end{aligned} \tag{5.24}$$

where μ is the constant diffusivity or conductivity and Δ is the Laplacian operator.

To carry out the DGCL compliance test, the problem (5.24) is solved on an unit square domain with $\mu = 0.01$, so that

$$\begin{aligned} u_t - 0.01 \Delta u = 0 \quad & \text{for } \mathbf{x} \in \Omega^{\mathrm{t}},\ \mathrm{t} \in (0, \mathrm{T}], \\ u_0 = 1 \quad & \text{for } \mathbf{x} \in \Omega^{0},\ \mathrm{t} = 0, \\ u = 1 \quad & \text{for } \mathbf{x} \in \Gamma^{\mathrm{t}},\ \mathrm{t} \in [0, \mathrm{T}], \end{aligned} \tag{5.25}$$

being the mesh deformed according to the following rule

$$\begin{aligned} \chi_1(\xi, t) = x = \xi + 0.125\ \sin(\pi\ t)\ \sin(2\pi\ \xi). \\ \chi_2(\eta, t) = y = \eta + 0.125\ \sin(\pi\ t)\ \sin(2\pi\ \eta). \end{aligned} \tag{5.26}$$

As was mentioned in §4.1 a discrete formulation is said to satisfy the DGCL

condition if it solves exactly a constant state regime, i.e. not depending on space or time, for a general mesh movement $\mathbf{x}(\boldsymbol{\xi}, t)$.

Figure (5.18) shows the reference domain and the deformed mesh for $t = 0.5$ $[s]$ where the maximum deformation occurs.

The problem is solved using piecewise linear triangles for the spatial discretiza-

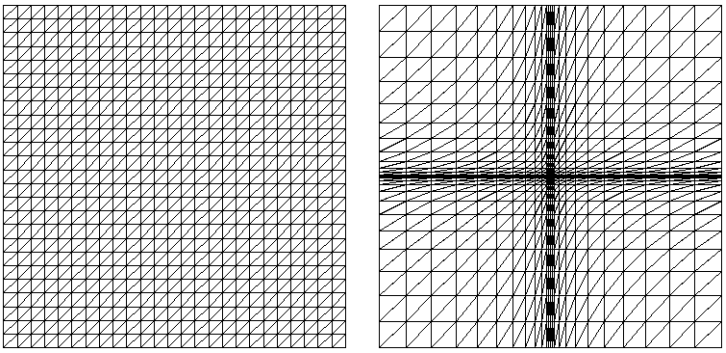

Figure 5.18: Reference and deformed mesh.

tion, a piecewise linear interpolation of the mesh movement and for the time integration the *Backward Euler* (BE, $\theta = 1$), *Crank-Nicolson* (CN, $\theta = 0.5$) and *Galerkin* (GA, $\theta = 2/3$) schemes are considered with $\Delta t = \{0.15,\ 0.1,\ 0.05,\ 0.025\}$. Figure (5.19) reports the error $||u_h - u||_{L^2(\Omega_t)}$ for three periods of oscillation, using the time integration methods and time steps mentioned above. The error must be null to machine precision over time for a DGCL compliant scheme.

A numerical error is introduced when using the *Backward Euler* or *Garlerkin* scheme due to lack in DGCL compliance for 2D problems. In Figure (5.20) the solution for times $t = \{0.1, 2.4, 5.4\}$ $[s]$ is shown for the three different integration schemes. The error related to the constant solution is located in the zones of the domain where the element deformation is higher, as in the center and the corners.

Now, if the Averaged Jacobian Formulation (AJF) is used, all these three time integration schemes are DGCL compliant, so the error remains null to machine precision (see Figure (5.21)).

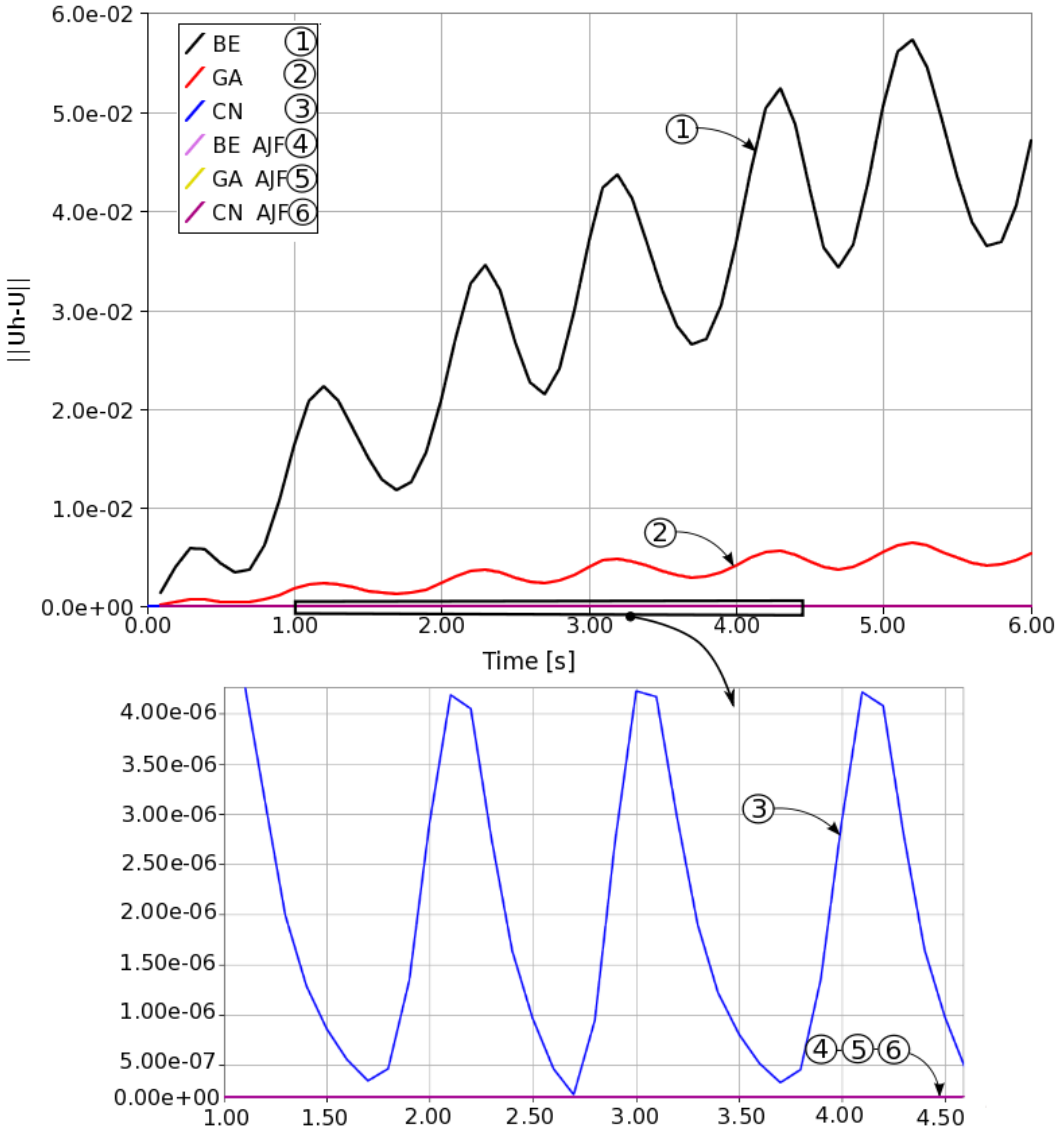

Figure 5.19: $||u_h - u||_{L^2(\Omega_t)}$ for *Garlerkin* (GA) and *Backward Euler* (BE) schemes compared with *Crank-Nicolson* (CN).

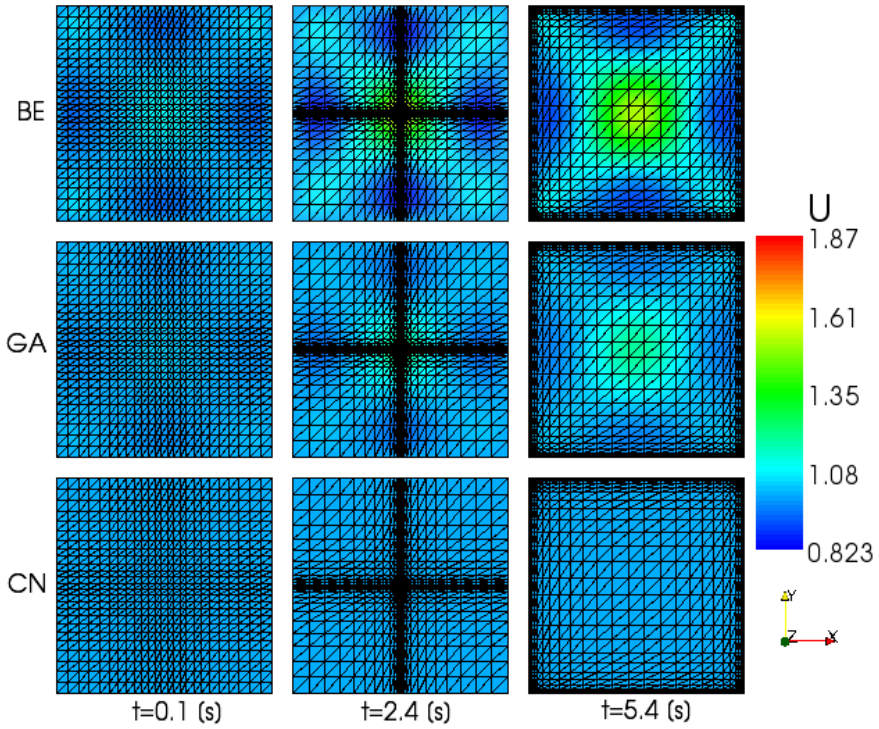

Figure 5.20: Solution for the *Backward Euler* (BE), *Galerkin* (GA) and *Crank-Nicolson* (CN) schemes.

5.4.2 Validation for 2D scalar diffusion problem with a periodic expansion and contraction of the domain

In this test case the problem (5.24) is solved in an unit square domain with $\mu = 0.1$, so that

$$\begin{aligned} u_t - 0.1\Delta u = 0 \quad & \text{for } \mathbf{x} \in \Omega^{\mathrm{t}},\ \mathrm{t} \in (0, \mathrm{T}], \\ u_0 = 1 \quad & \text{for } \mathbf{x} \in \Omega^{0},\ \mathrm{t} = 0, \\ u = 1 \quad & \text{for } \mathbf{x} \in \Gamma^{\mathrm{t}},\ \mathrm{t} \in [0, \mathrm{T}], \end{aligned} \tag{5.27}$$

being the domain deformed according to the following rule

$$\boldsymbol{\chi}(\boldsymbol{\xi}, t) = (2 - \cos(20\pi t))\boldsymbol{\xi}. \tag{5.28}$$

This deformation rule represents a periodic expansion and contraction of the

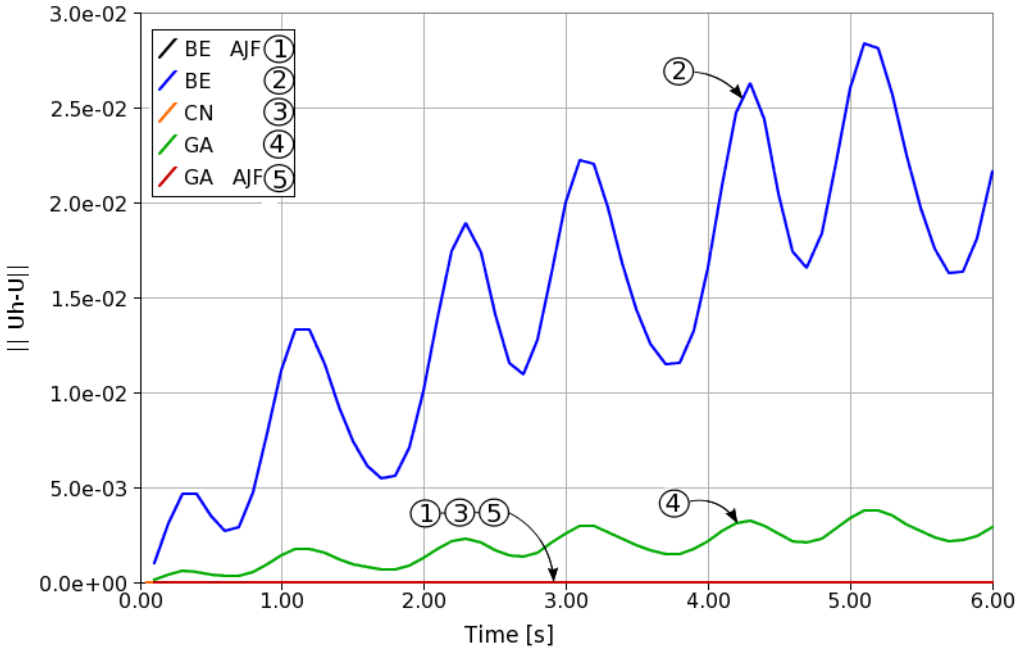

Figure 5.21: Errors using the Averaged Jacobian Formulation (AJF) and No-Averaged Jacobian Formulation for $\Delta t = 0.1$[s].

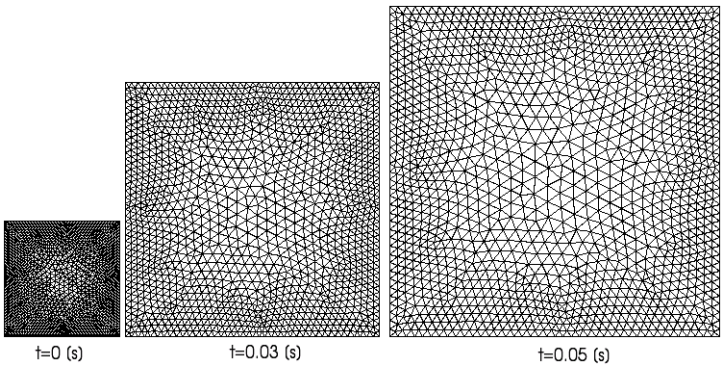

Figure 5.22: Deformed domain.

domain as it is shown in Figure (5.22) for $t = \{0, 0.03, 0.05\}$ $[s]$.

As in the previous case a numerical error is introduced when using the *Backward Euler* or *Garlerkin* scheme due to lack in DGCL compliance for 2D problems, but when the Averaged Jacobian Formulation (AJF) is used all the time integration schemes are DGCL compliant.

In Figure (5.23) the error $||u_h - u||_{L^2(\Omega_t)}$ in the solution is reported for four

periods of oscillation.

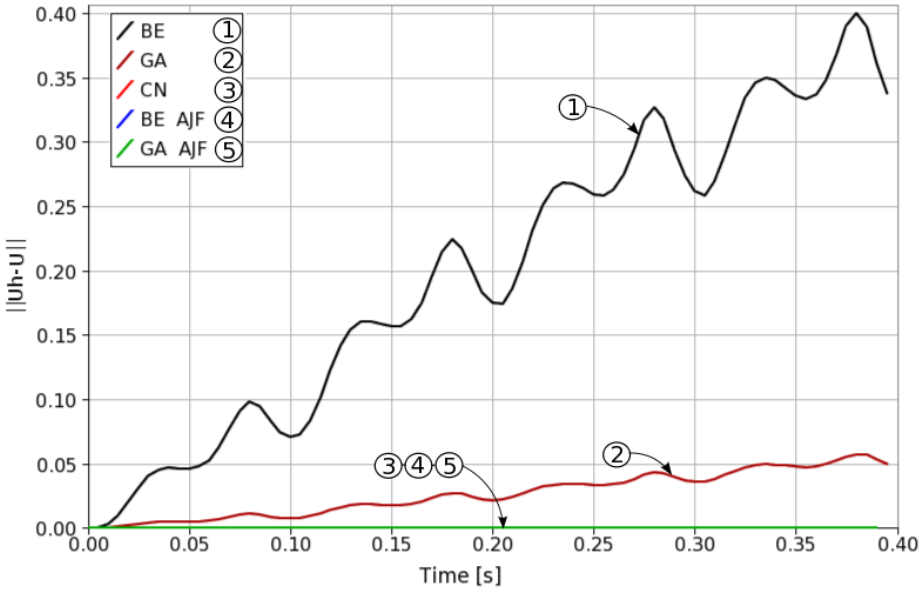

Figure 5.23: $||u_h - u||_{L^2(\Omega_t)}$ for *Backward Euler* (BE), *Galerkin* (GA) and *Crank-Nicolson* (CN) schemes for $\Delta t = 0.005$ [s].

5.4.3 Validation for 3D scalar diffusion problem with a periodic expansion and contraction of the domain

In this section the Averaged Jacobian Formulation is validated for 3D problems. The initial test is the extension to 3D of the problem (5.27) and the mesh moving rule (5.28). It is solved using piecewise linear tetrahedral for the spatial discretization, a piecewise linear interpolation of the mesh movement and for the time integration the *Backward Euler* ($\theta = 1$), *Crank-Nicolson* ($\theta = 0.5$) and *Garlerkin* ($\theta = 2/3$) schemes.

Figure (5.24) shows the deformed domain for $t = \{0, 0.03, 0.05\}$ $[s]$ and Figure (5.25) reports the error $||u_h - u||_{L^2(\Omega_t)}$ for four periods of oscillation. When the AJF is used the error remains null to machine precision, due to the scheme is DGCL compliant.

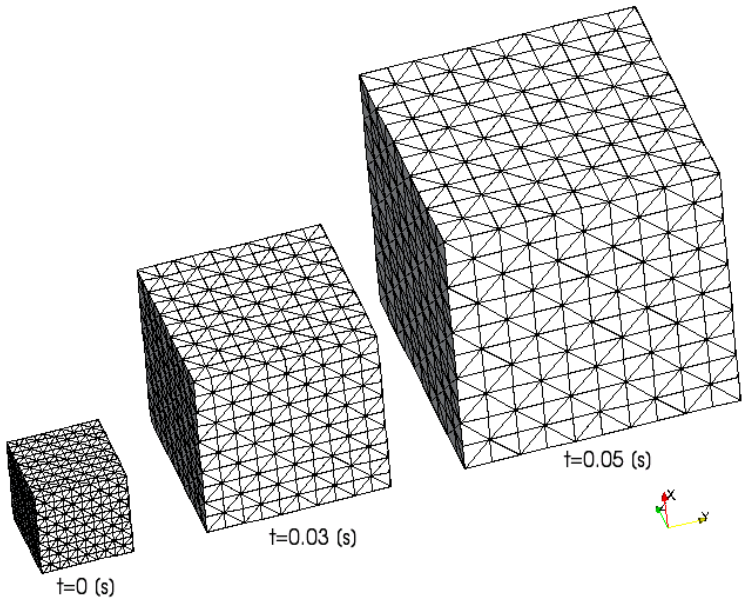

Figure 5.24: Deformed domain.

5.4.4 DGCL validation for 3D scalar diffusion problem with internal node movement

This test is the extension to 3D of the problem (5.25) and the deformation rule (5.26). It is solved using piecewise linear tetrahedral for the spatial discretization, a piecewise linear interpolation of the mesh movement and for the time integration the *Backward Euler* ($\theta = 1$), *Crank-Nicolson* ($\theta = 0.5$) and *Garlerkin* ($\theta = 2/3$) schemes.

Figure (5.26) shows the deformed mesh for $t = \{0, 0.5, 1.5\}$ $[s]$ and Figure (5.27) reports the error $||u_h - u||_{L^2(\Omega_t)}$. A numerical error is introduced when using any of the θ-family scheme in 3D problems due to lack in GCL compliance. In Figure (5.28) the solution for times $t = \{0.1, 2.4, 5.4\}$ $[s]$ is shown for the *Backward Euler* scheme. The error with respect to the constant solution are localized in the zones of the domain where the element deformation is higher, as in the center. But, when the AJF is used the error remains null to machine precision, due to the scheme is DGCL compliant.

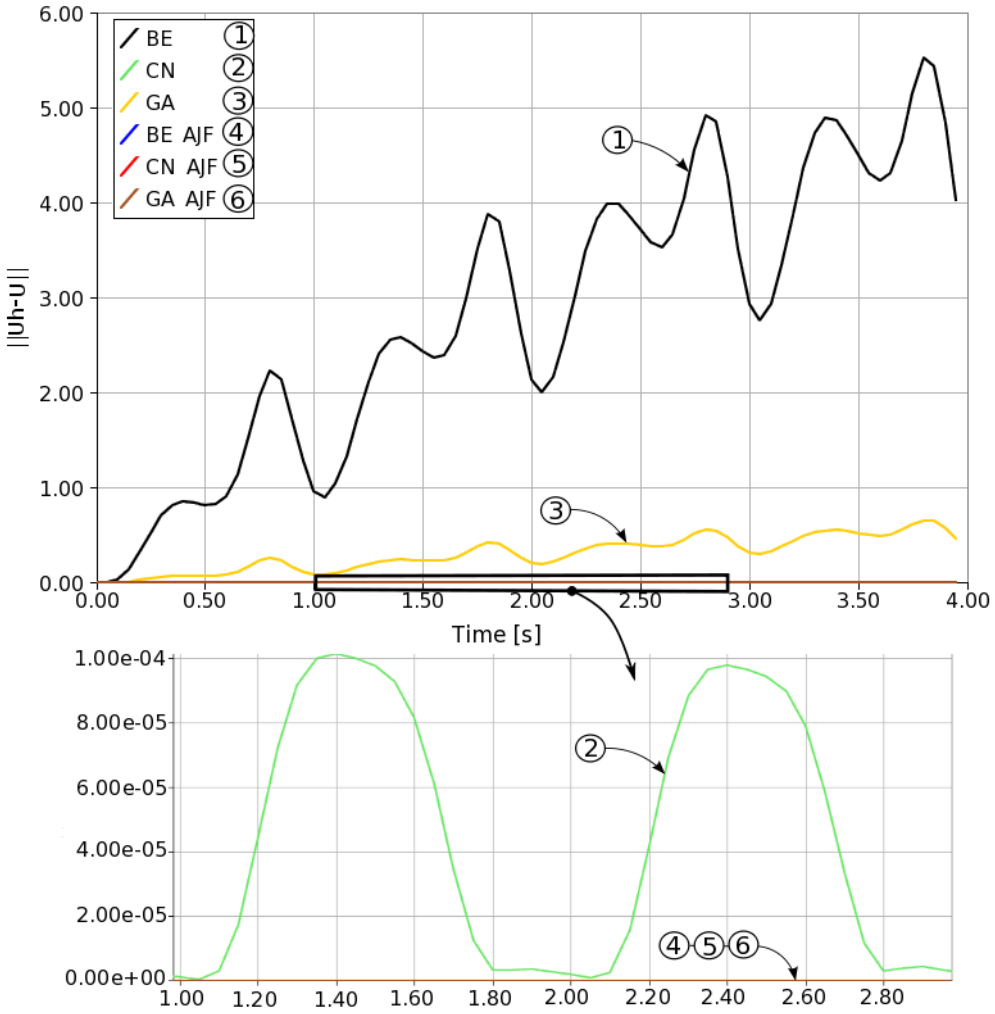

Figure 5.25: Errors for Averaged Jacobian Formulation (AJF) and No-Averaged Jacobian Formulation for $\Delta t = 0.005$ [s].

5.4.5 Moving an internal cylinder

This example consists of an external cylinder of radius R_2, which contains an internal smaller cylinder of radius R_1 and performs an harmonic motion of amplitude d_0 with an angular frequency ω, i.e. the instantaneous displacement of the center of the internal cylinder d is

$$d(t) = d_0 \sin(\omega t) \tag{5.29}$$

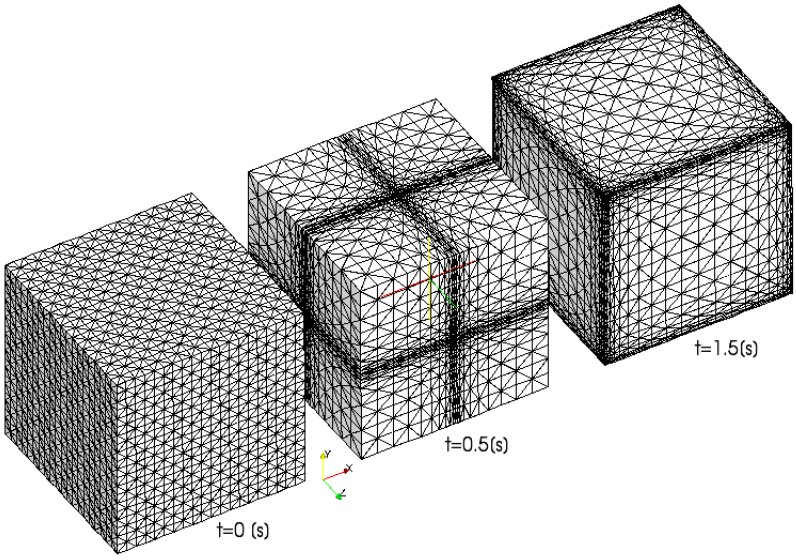

Figure 5.26: Deformed mesh.

In this example, an orthogonal mapping can be found between the reference domain where the two cylinders are concentric, and the general case where they are eccentric. The transformation between the current domain and the reference domain can be described as the composition of two conformal mappings ($z \to w \to v$) and a third orthogonal (but non-conformal) mapping ($v \to u$). Here u, v, w, and z are complex variables. The z-plane (see Figure 5.29(a)) is the physical plane with the current position (eccentric) of the inner cylinder. The region in the z-plane is

$$\Omega_z(t) = \{z \in \mathbb{C}/|z| < R_2 \text{ and } |z - d(t)| > R_1\} \tag{5.30}$$

The key transformation is the inversion

$$z = \frac{1}{w + d_w} + z_0 \tag{5.31}$$

which transforms the circular annulus

$$\Omega_w = \{w \in \mathbb{C} \ / \ R_{w2} \leq |w| \leq R_{w1}\} \tag{5.32}$$

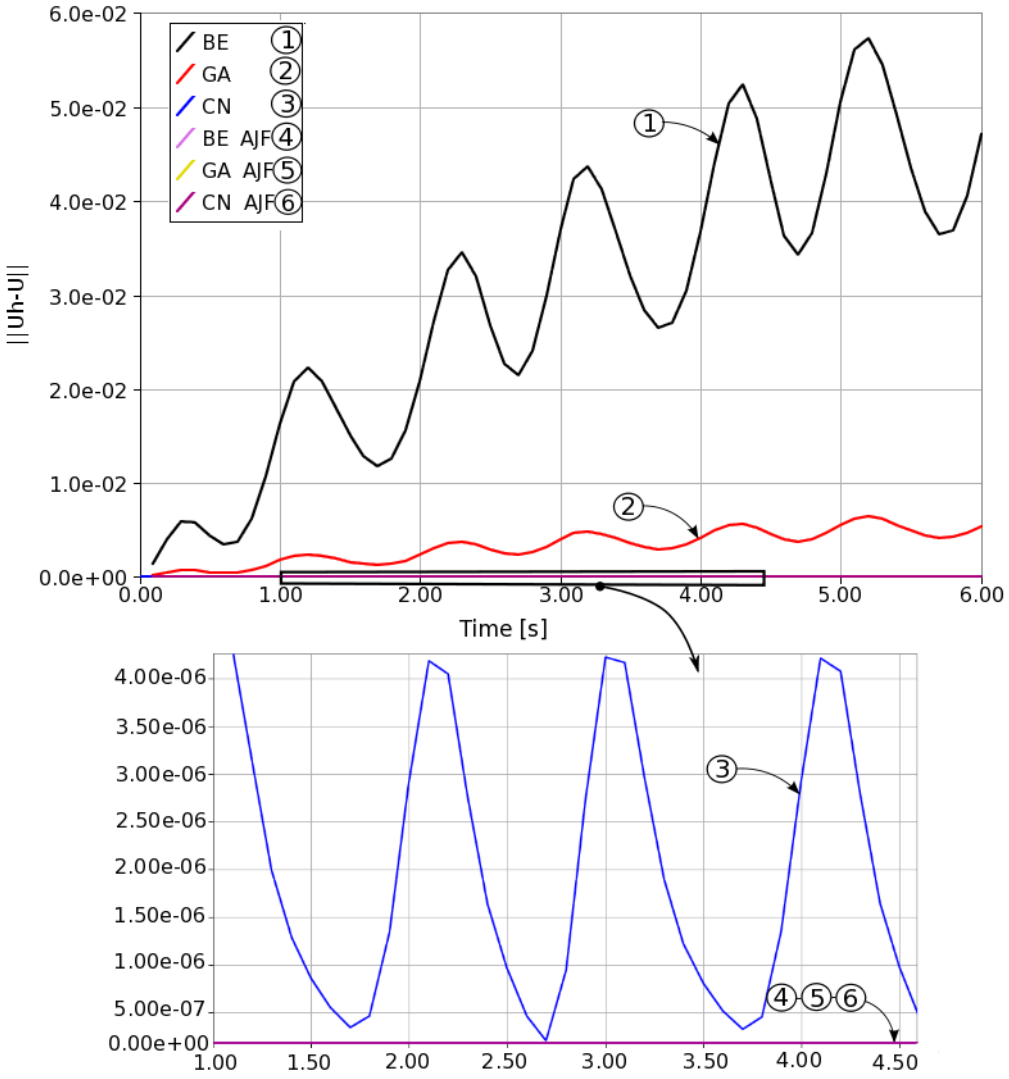

Figure 5.27: $||u_h - u||_{L^2(\Omega_t)}$ for *Backward Euler* (BE), *Galerkin* (GA) and *Crank-Nicolson* (CN) schemes for $\Delta t = 0.005$ [s].

in the w-plane onto Ω_z. As it is an inversion transformation, it maps lines and circles onto lines and circles. The real parameters of the transformation R_{w1}, R_{w2}, d_w, z_0 are unknown, but they can be easily found by adjusting the points A, B, C, and D, so that the radiuses in the z-plane are R_1 and R_2, as

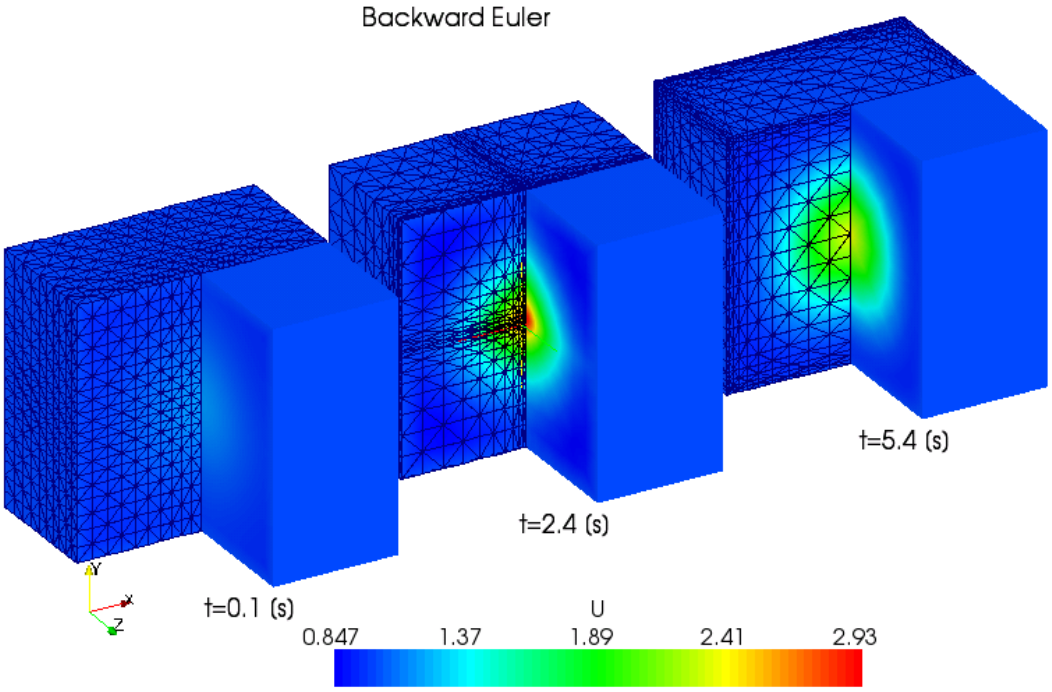

Figure 5.28: Solution for the *Backward Euler* (BE) scheme.

required. The coordinates of these points in the w-plane are

$$\begin{aligned} w_A &= R_{w2}, \\ w_B &= -R_{w2}, \\ w_C &= R_{w1}, \\ w_D &= -R_{w1}. \end{aligned} \tag{5.33}$$

and then, using the transformation (5.31), their z-coordinates are

$$\begin{aligned} z_A &= \frac{1}{d_w + R_{w2}} + z_0, \\ z_B &= \frac{1}{d_w - R_{w2}} + z_0, \\ z_C &= \frac{1}{d_w + R_{w1}} + z_0, \\ z_D &= \frac{1}{d_w - R_{w1}} + z_0. \end{aligned} \tag{5.34}$$

Then we arrive to the following equations

$$\begin{aligned} z_A - z_B &= 2R_2, \\ z_C - z_D &= 2R_1, \\ z_{c1} - z_{c2} &= \frac{z_C + z_D}{2} - \frac{z_A + z_B}{2} = d. \end{aligned} \tag{5.35}$$

The last equation comes from the requirement that the center z_{c1} of the internal cylinder must be shifted a distance d from the center z_{c2} of the external cylinder. Replacing withe the expressions for the z-coordinates given in (5.34) we arrive to the equations

$$\begin{aligned} \frac{1}{d_w + R_{w2}} - \frac{1}{d_w - R_{w2}} &= 2R_2, \\ \frac{1}{d_w + R_{w1}} - \frac{1}{d_w - R_{w1}} &= 2R_1, \\ \frac{1}{d_w + R_{w2}} + \frac{1}{d_w - R_{w2}} - \frac{1}{d_w + R_{w1}} - \frac{1}{d_w - R_{w1}} &= 2d. \end{aligned} \tag{5.36}$$

which is a system of three nonlinear equations that can be solved for R_{w1}, R_{w2}, and d_w in terms of R_1, R_2, and d. The system can be solved with the Newton-Raphson method, for instance. Note that the fourth parameter z_0 does not enter in the equations. Once these three parameters are found z_0 can be easily found from the requirement that the external cylinder must be centered at $\mathrm{Re}\{z\} = 0$, i.e.

$$z_{c2} = \frac{z_A + z_B}{2} + z_0 = 0, \tag{5.37}$$

from where

$$z_0 = -\frac{z_A + z_B}{2}. \tag{5.38}$$

Once the $z - w$ transformation is known, the other two are easily found. Note that, due to the inversion, the internal radius in the Ω_w domain is mapped onto the external radius in the Ω_z domain, and viceversa. Then, a second inversion is performed

$$w = \frac{1}{v}, \tag{5.39}$$

and the resulting Ω_v domain is a circular annulus

$$\Omega_v = \{v \in \mathbb{C}^2 \ / \ R_{v1} \leq |v| \leq R_{v2}\}\}. \tag{5.40}$$

with $R_{v1} = 1/R_{w1}$, and $R_{v2} = 1/R_{w2}$. Finally, the transformation $u - v$ is orthogonal (but non-conformal), that maps linearly the radius so as to map the Ω_v domain onto the reference domain

$$\Omega_u = \Omega_z(d = 0) = \{u \in \mathbb{C}^2 \ / \ R_1 \leq |u| \leq R_2\}\}. \tag{5.41}$$

The transformation is better described in terms of polar coordinates $v = |v|\mathrm{e}^{\mathrm{i}\phi_v}$, $u = |u|\mathrm{e}^{\mathrm{i}\phi_u}$ as follows

$$\begin{aligned} \phi_v &= \phi_u, \\ |v| &= R_{v1} + \frac{|u| - R_1}{R_2 - R_1}(R_{v2} - R_{v1}). \end{aligned} \tag{5.42}$$

Computationally, the process is as follows. At a certain time t the nodes position must be determined, first the parameters of the transformation are determined from (5.35). Then, given the coordinates of the node in the reference domain u, the successive transformations (5.42), (5.39), and (5.31), are applied, and the coordinates of the node in the actual position of the mesh z are obtained.

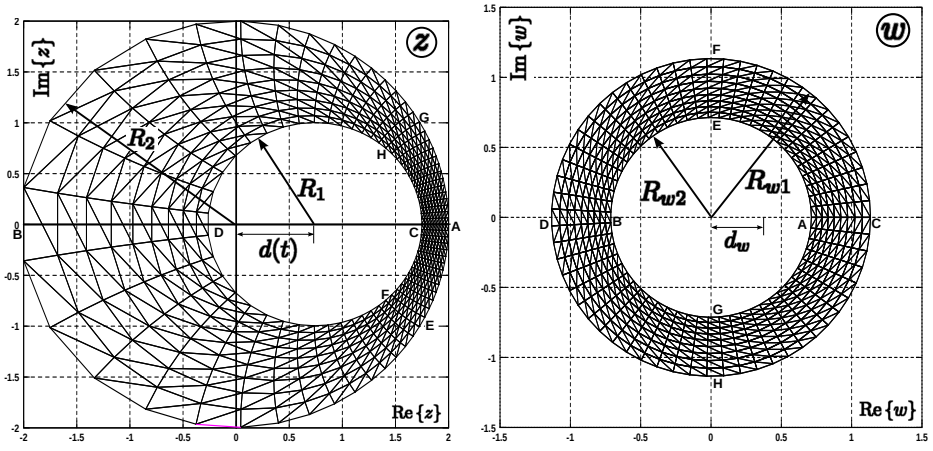

(a) z-plane (b) w-plane

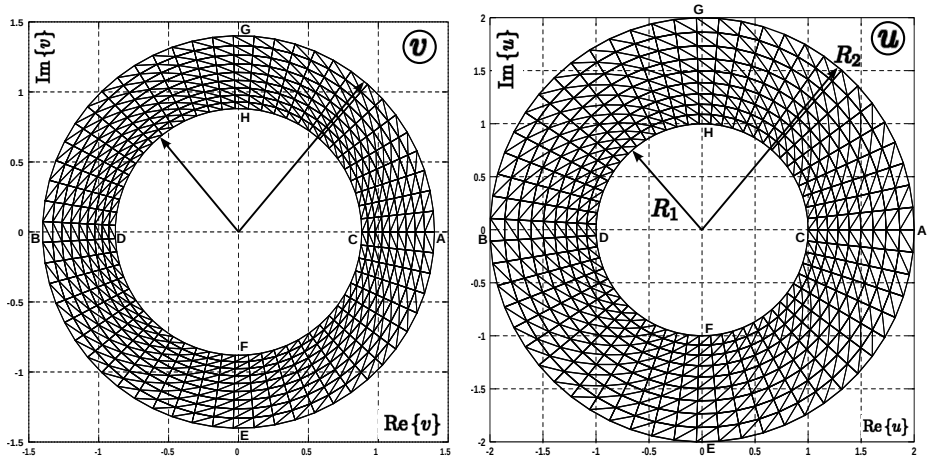

(c) v-plane (d) u-plane

In this test the parameters used were $R_2 = 2$, $R_1 = 1$, $\omega = 1.047$ and $d_0 = 0.7$. The domain was discretized with 10 elements in the radial direction and 96 elements in the perimeter using linear triangular elements (see Figure (5.29)). The dimensionless equations of a viscous compressible flow were solved in the interior of the domain using the Backward Euler time integration scheme, varying the Courant number between 2 and 0.025.

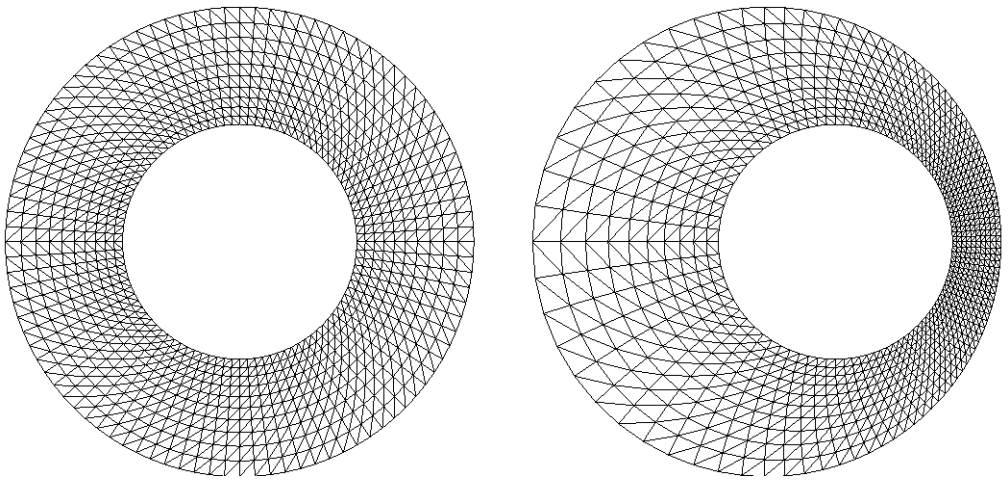

Figure 5.29: Initial mesh and maximum displacement mesh.

In order to analyze the numerical error introduced due to lack in DGGL

compliance, the density on a fixed spatial point with coordinates $\mathbf{x} = (1.8, 0.2)$ was plotted in Figures (5.30) to (5.32) for 4 periods of oscillation.

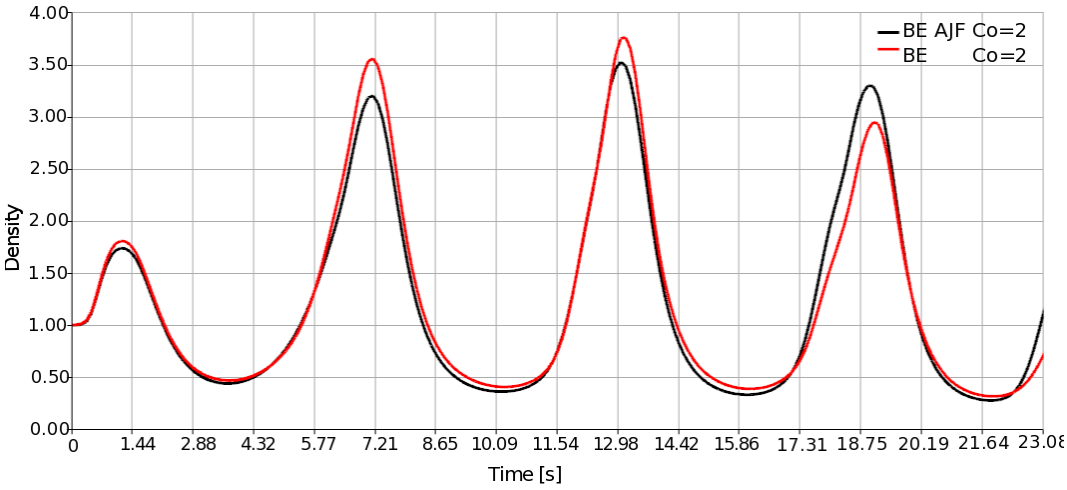

Figure 5.30: Density using the Averaged Jacobian Formulation (AJF) and No-Averaged Jacobian Formulation for Co = 2.

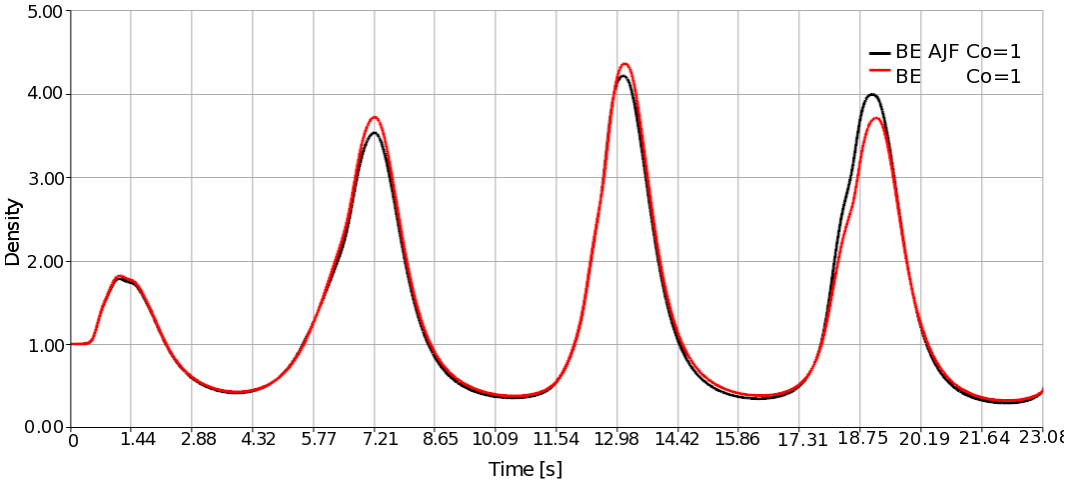

Figure 5.31: Density with and without the Averaged Jacobian Formulation (AJF) for Co = 1.

As the time step is reduced, the differences between the solutions obtained with and without the AJF decreases, as was stated in the previous examples. In the results corresponding to Co = 2, the difference between both solutions

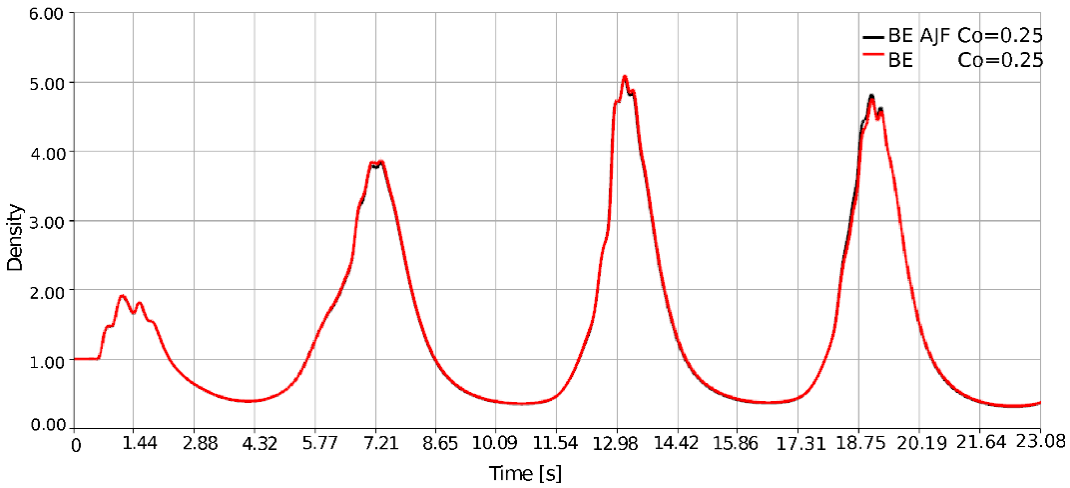

Figure 5.32: Density with and without the Averaged Jacobian Formulation (AJF) for Co = 0.25

are significative while in the results corresponding to Co = 0.25 are negligible.

In Figure (5.33) the pressure distribution in the domain for different positions of the inner cylinder is shown. The domain was discretized with 35 elements in the radial direction and 342 elements in the perimeter using triangular elements. The pressure increase in the compressed region induces a fluid motion toward the opposite side as shown by the velocity vectors of the figure.

5.5 Numerical simulations of FSI problems

In this section the numerical simulation of the start-up process of a rocket engine using the partitioned algorithm presented in chapter §3 and the methodologies presented in chapter §4 is carried out. The start-up process of a rocket engine is simulated and the shifting of two modes due to the coupling with the fluid are analyzed. The resolution of this problem was a great challenge, because the consulted references on the area solve the problem as two-dimensional. Moreover, the shifting of the natural frequencies can be studied only by solving the problem in 3D.

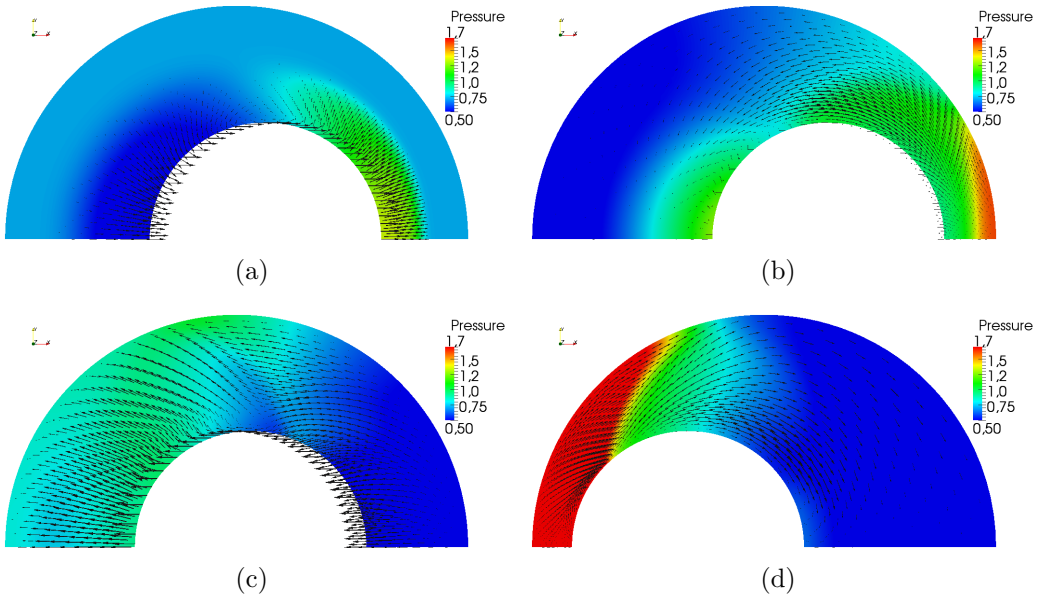

Figure 5.33: Pressure at different positions of the inner cylinder.

5.5.1 Simulation of a rocket nozzle ignition

The algorithm described and validated in previous sections will be used to obtain the deformation in the nozzle of a rocket engine during the ignition. This problem has been under study by many researchers over the years, carrying both numerical (Lefrancois et al., 1999; Taro Shimizu and Tsuboi, 2008; Wang, 2004; Lefrancois, 2005) and experimental (Shashi Bhushan Verma Ralf Stark, 2006; Moríñigo and Salvá, 2008) analysis.

Nozzles with high area ratio are used in the main space launchers (Space Shuttle Main Engine, Ariane 5). These engines must work in conditions ranging from sea level to orbital altitude but an efficient operation is reached only at high altitude. The nozzles contour is often designed according to the theory proposed by Rao Rao (1996) that results in TOP (Thrust Optimized Parabolic or Parabolic Bell Nozzle) nozzle, which has some advantages compared to the traditional conical shapes. These advantages are the smaller length, lower weight, as well as the reduction in energy losses in the expansion of gases (Sutton and Biblarz, 2001; Oates, 1997; Mattingly and Ohain, 2006; Tuner, 2006).

During the start-up phase the structure is deformed due to the advance of a shock wave that is highly detrimental to the integrity and service life cycle of the rocket engine. Many problems have been encountered in the Space Shuttle Main Engine, European Vulcain (Ariane) and in the Japanese LE-7, all these were related to the ignition stage and side loads phenomena.

The nozzle under study has a bell-shape geometry which is generated by rotating a contour line around the x axis. In this way the 3D geometry is obtained (see Figure (5.34)).

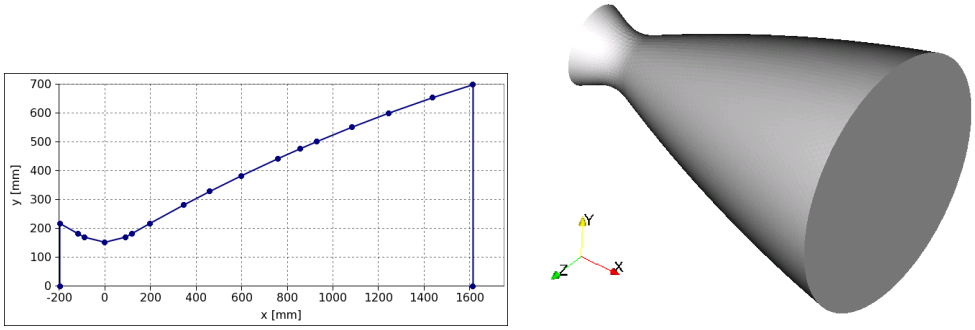

Figure 5.34: Contour line and 3D model.

The most relevant geometrical data are detailed below:

- Overall length: $l = 1810$ [mm].
- Throat diameter: $D_t = 304$ [mm].
- Exit diameter: $D_e = 1396$ [mm].
- Area ratio: $\epsilon = 21.1$.

5.5.2 Numerical Model

Starting from the three-dimensional model two independent meshes are generated, one for the fluid domain discretization and the other for the structure domain discretization. A mesh with 334700 tetrahedral elements is generated for the fluid with a linear interpolation of the variables. The structural mesh is

composed of 59600 wedge (triangular base prismatic) elements. Detailed view of grid zones of both meshes is shown in Figure (5.35).

In FSI problems there is an information transfer in the fluid-structure interface. Using conforming meshes (node to node coincident) on the interface, the transmission is direct and does not need an algorithm to do a surface tracking, state interpolation and load projection, but the major drawback of this method is that refinement in the structure mesh will cause an increase in the fluid mesh and therefore in the overall problem size.

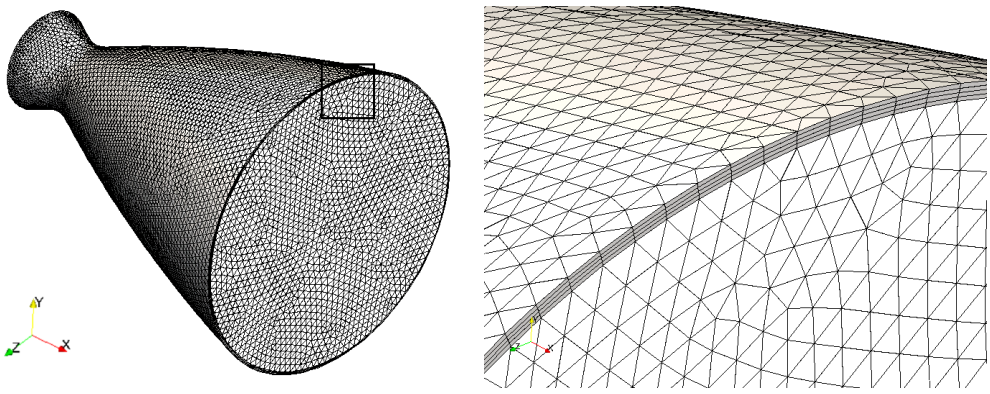

Figure 5.35: Spatial discretization for the fluid and for the structure.

The structural problem is solved using the theory of constitutive linear elastic material and geometrically nonlinear, as shown in section §2.2. For the fluid, the gasdynamics Euler equations are solved and SUPG stabilization is used together with the shock-capturing method (see section §2.1). Using the Euler equations the CPU and memory costs can be significantly reduced comparatively to the viscous case. Furthermore, from previous works (Prodromou and Hillier, 1992; Igra et al., 1998) it can be concluded that this equations correctly predict the main flow features.

The strategy adopted in this work to solve an aeroelastic problem would be useful when analyzing the stability of nozzles, and it will be considered in a future work. In the early 1990's simplified techniques for analyzing the stability were proposed by Pekkari (1993, 1994), where the parietal pressure due to the wall deformation is given by an analytical expression. A recent work carried out by Östlund (2004) made an improvement in the technique. But

Table 5.4: Solid Properties

Young's modulus	Poisson's coeff.	Density	Thickness
$2.07 \cdot 10^{10}$ [N/m^2]	0.28	8400 [kg/m^3]	0.015 [m]

Table 5.5: Fluid Properties

R	γ	ρ_∞	T_∞	p_∞
287 [J/kg K]	1.40	1.225 [kg/m^3]	288 [K]	101253 [Pa]

these methods solve the aeroelastic problem in a decoupled fashion.

In order to solve the aeroelastic problem the material properties for the nozzle and fluid are summarized in Tables 5.4 and 5.5. In this work the nozzle is modeled with an homogeneous material, but more complex structural models can be similarly used.

5.5.3 Boundary and Initial Conditions for the Nozzle Ignition Problem

The FSI problem requires initial and boundary conditions for both, the structural and the fluid problem, separately. The nozzle is clamped (all displacements null) at the junction with the combustion chamber and the rest is left free. In the fluid flow problem a slip condition is applied to the wall of the nozzle, which is mathematically represented by the following equation.

$$(\mathbf{v} - \mathbf{v}_{str}) \cdot \hat{\mathbf{n}} = (\mathbf{v} - \dot{\mathbf{u}}) \cdot \hat{\mathbf{n}} = 0. \tag{5.43}$$

As mentioned above the slip condition must be applied dynamically because the normal to the wall and the structure velocity change during the simulation. For the fluid, (p_0, T_0) are imposed at the inlet. These conditions are taken from the stagnation condition of the combustion chamber (p_0, T_0), and then ρ_0 is computed from the state equation (see Table 5.6).

Table 5.6: Stagnation values used for the combustion chamber

p_0	ρ_0	T_0
26 [MPa]	306.25 [kg/m^3]	299 [K]

The modeling of the ignition of a rocket exhaust nozzle is challenging from several points of view. One of these points is the imposition of non-reflective boundary conditions at the outlet (Paz et al., 2010). Moreover, in such case, the number of boundary conditions at the outlet change from rest (i.e., subsonic flow) to supersonic flow as a shock wave appears at the throat and propagates toward the boundary. So, the condition must be capable of handling the dynamical change of the Jacobians matrix profile. During the flow computation inside the nozzle the number of incoming/outgoing characteristics, and therefore the number of Dirichlet conditions to be imposed, will change. Having a boundary condition that can automatically adapt itself to this change is essentially useful in such a problem. In addition, the computational domain can be limited to the nozzle interior up to the exit plane, with a significant reduction in CPU time and memory use. Imposing absorbent/dynamic boundary conditions is based on the analysis of the projection of the Jacobians of advective flux functions onto normal directions to fictitious surfaces. The advantage of the method is that it is very easy to implement and that it is based on imposing non-linear constraints via Lagrange Multipliers or Penalty Methods (see Reference Storti et al. (2008) for a more detailed description).

Initial conditions must be established in both domains. The following are adopted for the fluid

$$\mathbf{v}(\mathbf{x}, t_0) = 0, \tag{5.44}$$

$$p(\mathbf{x}, t_0) = p_\infty, \tag{5.45}$$

$$\rho(\mathbf{x}, t_0) = \rho_\infty, \tag{5.46}$$

Table 5.7: Characteristic Dimensions

Nozzle	**Vulcain**	**S1**	**S3**
Area ratio (ϵ)	45	20	18.2
Nozzle length (L) [mm]	2065.5	350	528.2
Throat diam. (D_t) [mm]	262.4	67.08	67.08
Nozzle exit diam.(D_e) [mm]	1760.2	300.0	286.5

and for the structure

$$\mathbf{u}(\mathbf{x}, t_0) = 0, \tag{5.47}$$

$$\dot{\mathbf{u}}(\mathbf{x}, t_0) = 0. \tag{5.48}$$

5.5.4 Aeroelastic behavior of the nozzle

The proposed numerical problem was carried out on a cluster (Guruswamy (2007)) machine using 30 processors Intel® Pentium®IV Prescott 3GHz with 2 Gb of RAM (DDR2 400 Mhz), interconnected with two switch Gigabit Ethernet (1 Gbit/sec), 3Com®Super Stack 3. In the simulation, 2000 time steps with a $\Delta t = 2 \cdot 10^{-5}$ [secs] are computed to obtain a fully developed flow, taking into account that the shock wave leaves the interior of the nozzle in approximately $8.8 \cdot 10^{-3}$ [secs].
Before performing the aeroelastic analysis, the nozzle used in this work is compared to the Vulcain nozzle and to the sub-scale S1 and S3 nozzles (see Table 5.7) through a parametric study that was carried out in Östlund (2002). That is done because the fluid flow field is determined by the shape of the nozzle and this affects the pressure distribution on the wall from which the fluid loads are computed.

In the S1 sub-scale nozzle the characteristic length for the scaling was the nozzle exit radius (r_e) and in the S3 sub-scale nozzle was the throat radius (r_t), thus different contours are obtained. Therefore to perform an aeroelastic study of the proposed TOP (Thrust Optimized Parabolic or Parabolic Bell Nozzle) nozzle the radius and the wall pressure distribution (p_w) must be comparable to the Vulcain, S1 and S3 (see Figure (5.36) and Figure (5.37)).

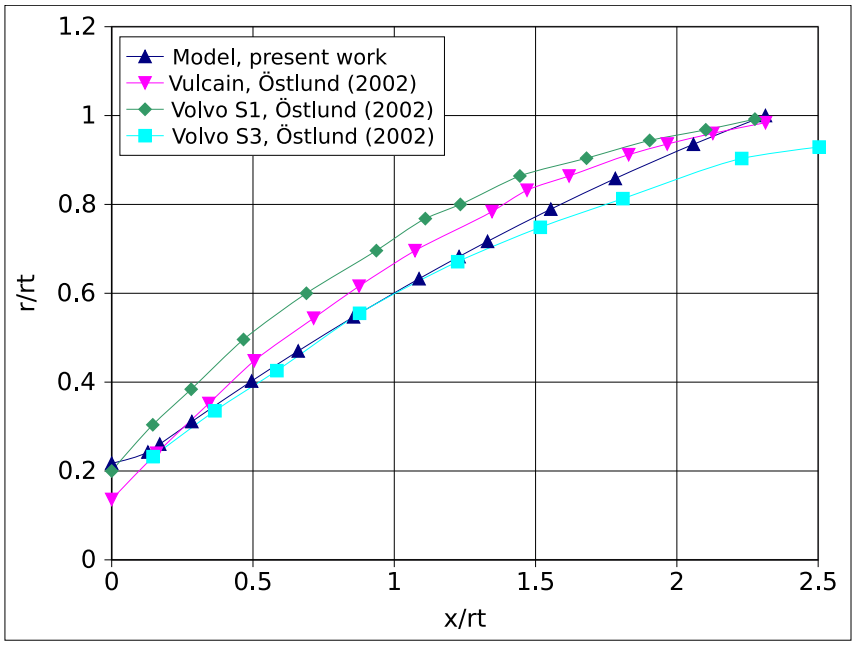

Figure 5.36: Radius distribution.

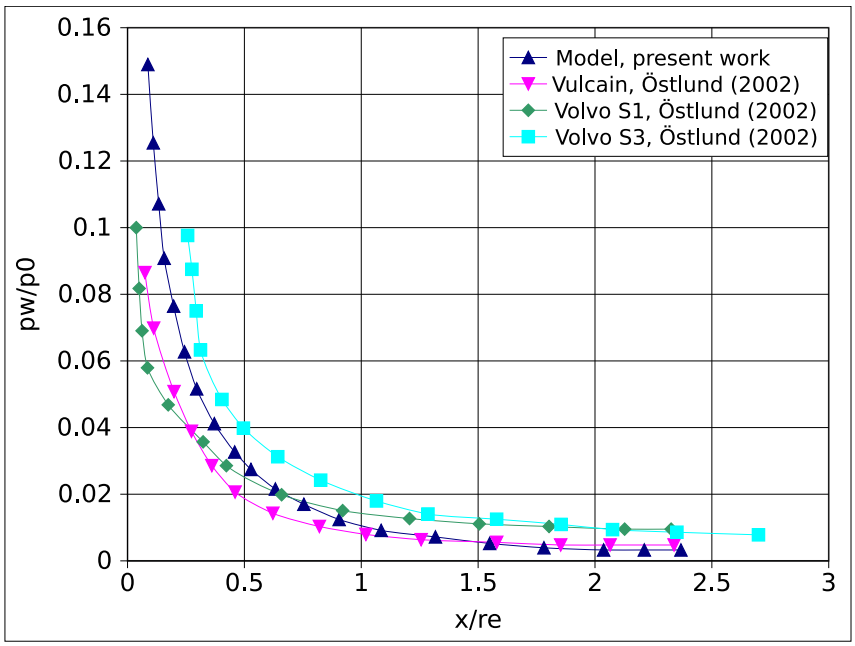

Figure 5.37: Wall pressure distribution.

Figure (5.36) shows that the TOP nozzle under study has similar radius distribution than Vulcain, S1 and S3, which makes valid the comparison between the parietal pressures. Then, the computed wall pressure when the flow is completely developed is compared, showing a good agreement.
Having verified the pressure distribution when the flow is completely developed, the next step is to study qualitatively the evolution of the shock wave during the start-up. Lefrancois (2005) describes the behavior of the structure when a shock wave moves through the divergent zone of the nozzle and the process is outlined in Figure (5.38).

During the start-up process the pressure increases linearly from p_∞ to p_0 in $1 \cdot 10^{-4}$ seconds. The formed shock moves rapidly (faster than the speed of sound for the non-perturbed condition) trough the stagnant low pressure medium. Also a secondary left running (with respect to the fluid) shock wave appears and is carried to the right because of the supersonic carrier flow. This shock wave links the high Mach number, low pressure flow, with the lower velocity high pressure gas behind the primary shock. The results of the fluid structure interaction during this stage are shown in Figure (5.39), together with the pressure at the wall.

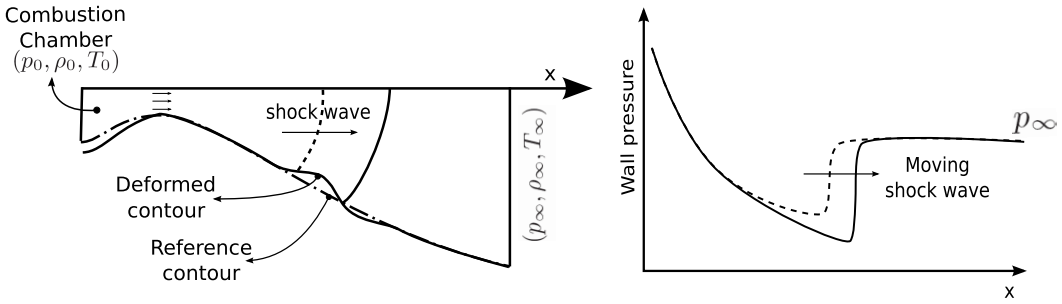

Figure 5.38: Schematic deformation of the structure.

Note a large pressure jump across the secondary shock wave (see Figure (5.39)), which produces significant bending moments in the structure, changing the outflow pattern and the pressure downstream while the shock wave propagates towards outlet, making this process totally dynamic.

First of all, a run is performed only considering the fluid problem (hereafter case name **NO-FSI**) such that the parietal pressure is computed without the

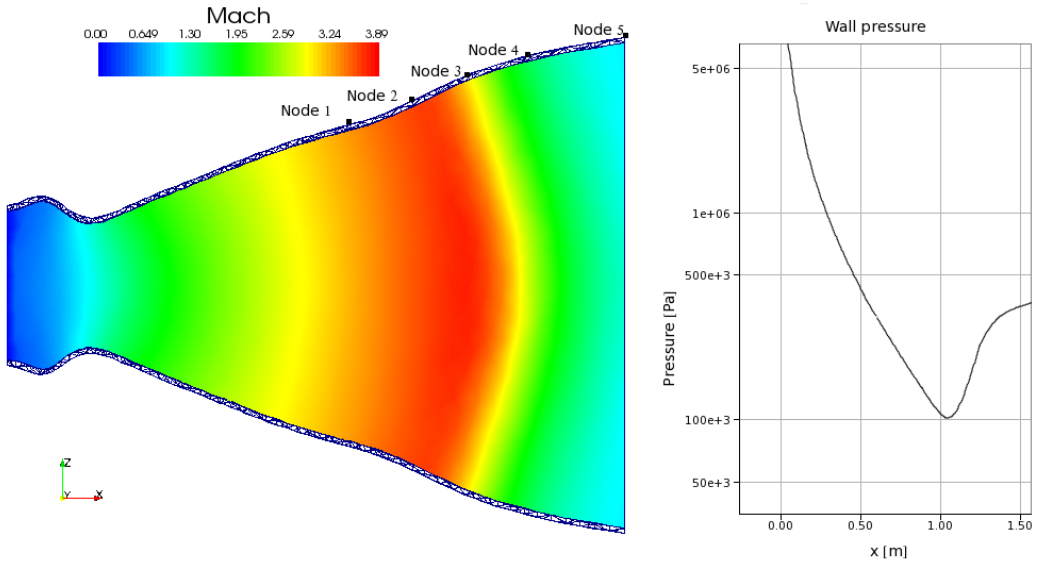

Figure 5.39: Structure deformation and pressure distribution for the moving shock wave.

effect of the wall movement. Then, the coupling is performed (case name **FSI**) and the parietal pressures of both cases are compared. The temporal evolution of the pressure at the nodes (1-5) located at the positions shown in Figure (5.39) are plotted in Figure (5.40).

As seen in the Figures, the wall displacements (shown in Figure (5.41)) produce oscillations in the fluid pressure which are not considered for the first case **(NO-FSI)**. As the plot shows, considering the wall displacement to compute the pressure acting in the nozzle is very important and this is one of the key points of this work.

In this case the shock wave is expelled from the nozzle but in certain operating condition, like overexpanded mode, the shock wave do not leave the nozzle. This kind of shock produces a strong pressure jump and coupled with the structure deformation can cause an asymmetric pressure distribution as is mentioned in Östlund (2004). So, this is a first step in order to demonstrate the relation between the aeroelastic coupling and the acting lateral loads.

The sequence in Figure (5.42) shows the behavior of the structure as the shock wave moves through the divergent section of the nozzle. Also, the Mach number on the nozzle centerline is plotted in the right side.

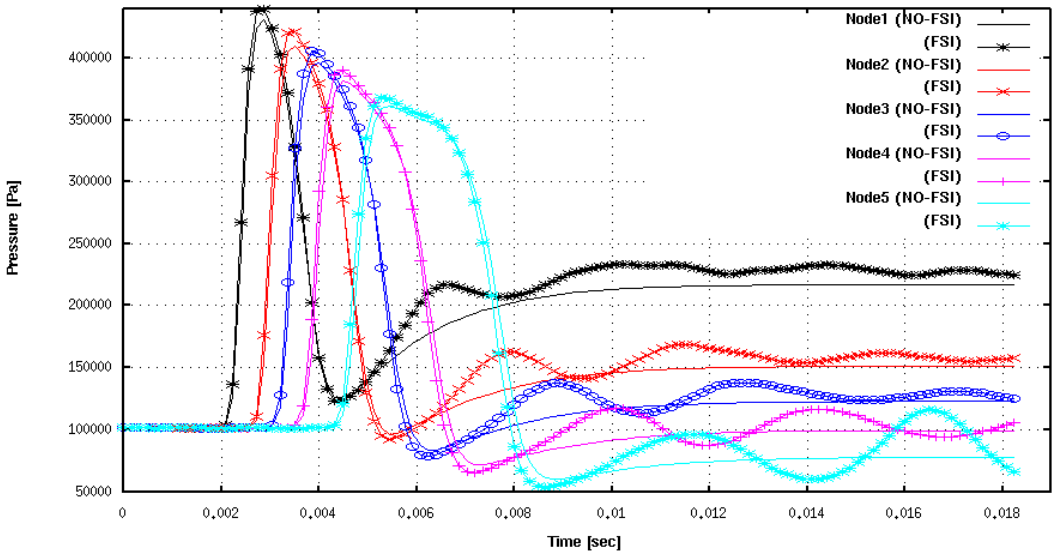

Figure 5.40: Wall pressures during the start-up. Comparison between **NO-FSI** and **FSI** cases.

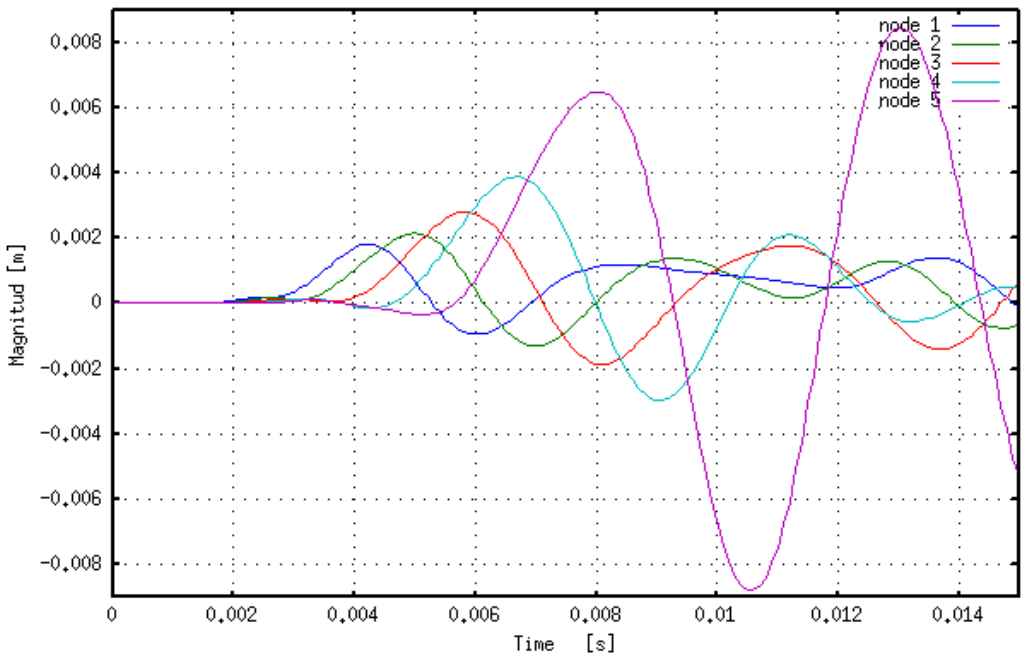

Figure 5.41: Displacement of nodes 1-5.

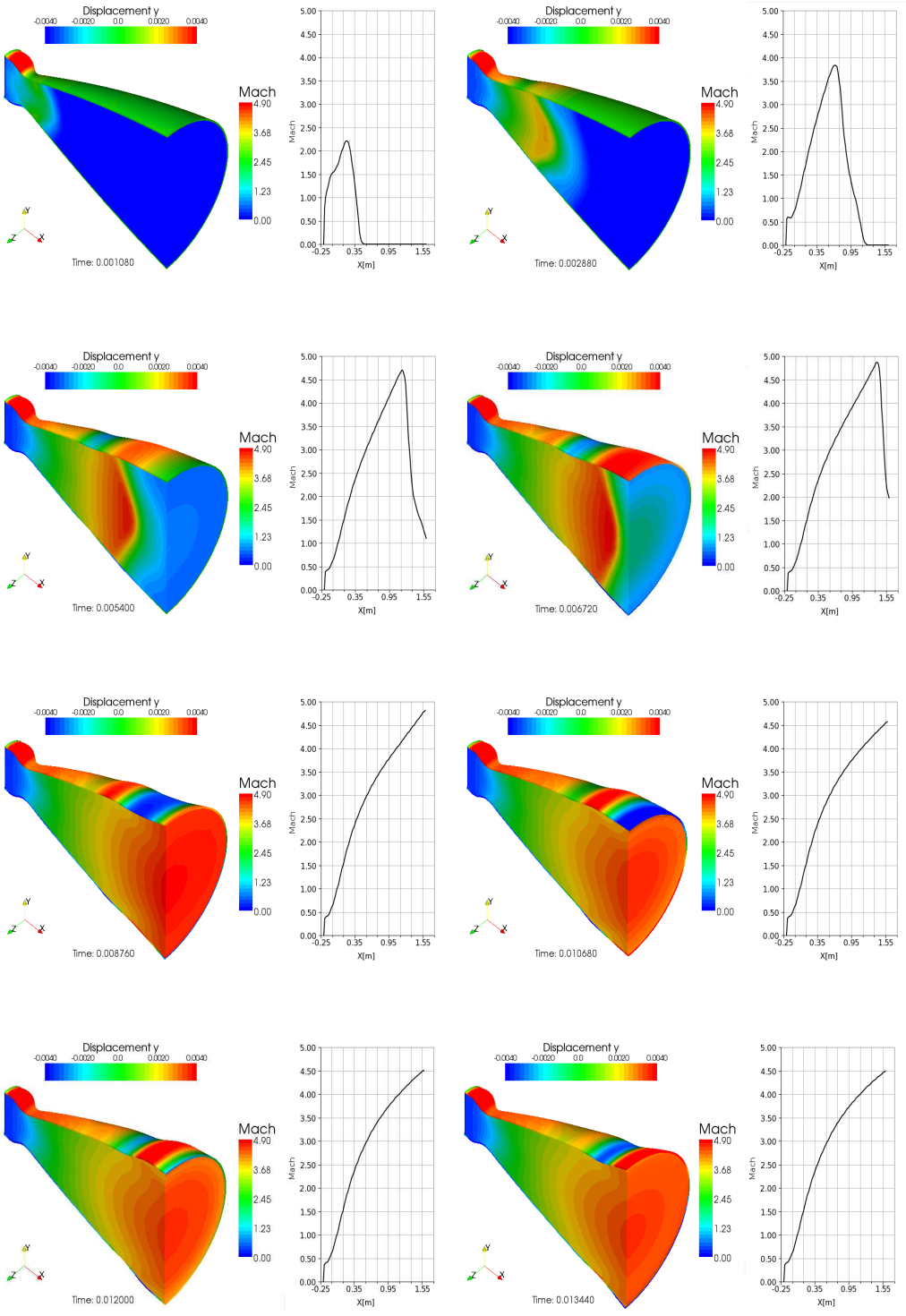

Figure 5.42: Ignition process of the rocket engine.

5.5.5 Aeroelastic Frequency Shifting

During the design of a nozzle it is important to predict the response of the structure under thrust loads, like lateral ones, because in normal operating conditions, the nozzle is subject to external and internal flows that change the wall pressure distribution dynamically. There exist several approaches to perform this analysis, starting from the simplest one, where the nozzle is characterized only by the mass, the inertia and a torsional spring at the throat, to more complex FSI models (Tezduyar et al., 2006) as the one studied in this work.

The following analysis gives some physical insight in how the fluid forces shift the eigenfrequencies of the system due to the coupling phenomena.

The most studied mode in the nozzle structure problem, is the lowest frequency bending mode (1) (see Figure (5.43)). In this work, the study is extended to the lowest frequency axial mode (2). The bending mode is excited by side loads while the axial mode is excited by fluctuations in the thrust, as occurs during start-up.

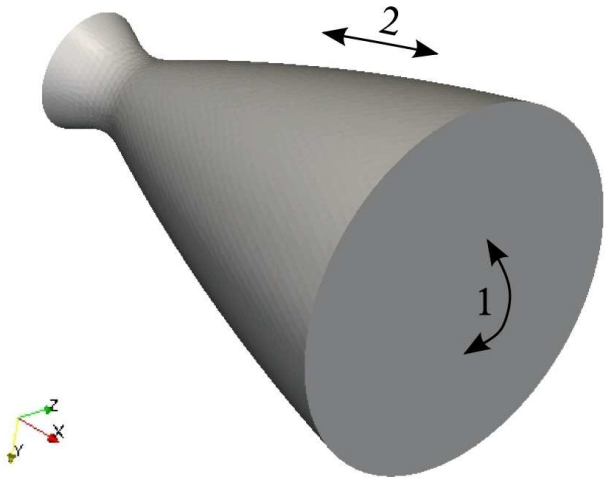

Figure 5.43: Modes of vibration.

For the computation of the eigenfrequencies ω_i of the structure two methods are considered. One is the "hammer test" where the nozzle is deformed and

then is free to vibrate, characterizing the modes and frequency via a FFT (Fast Fourier Transform). The other method is the ''Generalized Eigenvalue Problem'' (GEVP) in which the mass and rigidity matrix are needed to solve the system

$$(\mathbf{K} - \omega_i^2 \mathbf{M})\ \mathbf{u} = 0. \tag{5.49}$$

The eigenfrequencies obtained with these methods are listed in Table 5.8.

Table 5.8: Eigenfrequencies

-	FFT [Hz.]	GEVP [Hz.]	Diff %
Mode 1	17.2	15.7	9.5
Mode 2	138.5	129.9	6.6

The next step is to compute the eigenfrequencies for the coupled problem. Therefore to obtain these eigenfrequencies, the structure and the fluid are started from a fully-developed steady flow condition computed previously, being the structure deformed with the eigenvector obtained from the GEVP corresponding to the studied modes. Then, a FFT is performed over the temporal displacement of the nodes 1-5. The frequencies resulting after carrying out these numerical simulations are compared in the Figure (5.44).

This analysis shows that the influence of the fluid-structure coupling may be very important, producing a frequency shift of 47.7% for the bending mode and 8.7% for the axial mode. In addition, the frequency of the axial mode increases, while the frequency of the bending mode decreases. It will be shown with a simple analysis that this change in behavior can be explained by the sign of the additional stiffness when considering the coupling with the fluid. The governing equations for the structure are

$$\mathbf{M}\ddot{\mathbf{u}} + \mathbf{C}\dot{\mathbf{u}} + \mathbf{K}\mathbf{u} = F_{\text{aero}}(\mathbf{u}, \dot{\mathbf{u}}, \ddot{\mathbf{u}}, ...), \tag{5.50}$$

where $\mathbf{M}$ is the mass matrix, $\mathbf{C}$ is the damping matrix, $\mathbf{K}$ is the stiffness matrix and F_{aero} is the aerodynamic forcing term which can be expanded in term of a series in $\mathbf{u}$ and its derivatives, from which the terms up to second order are retained.

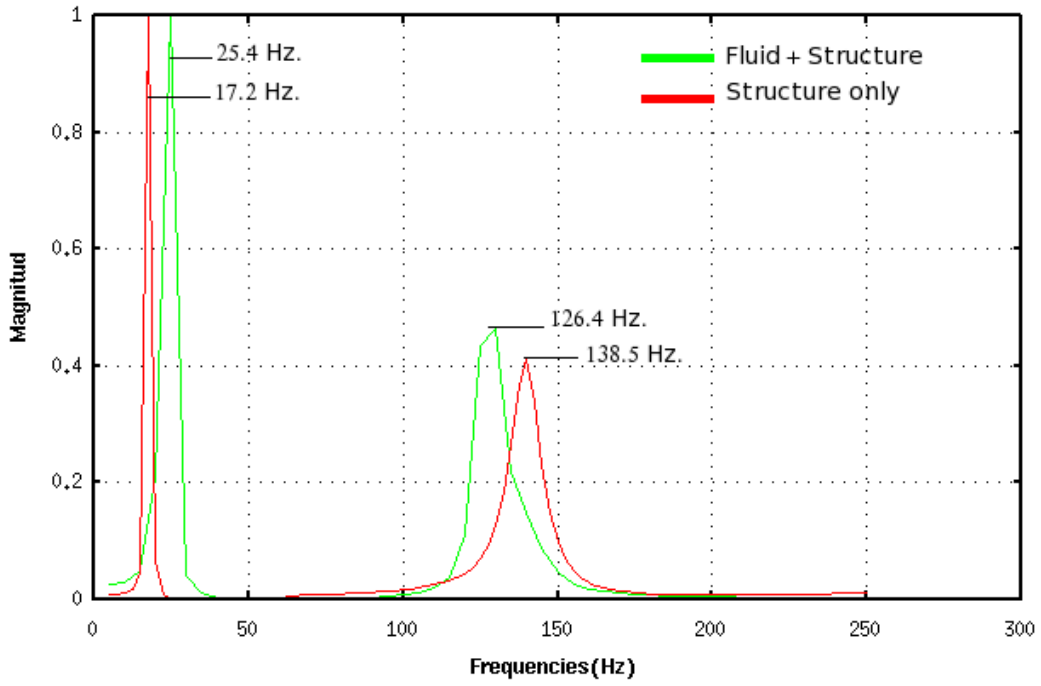

Figure 5.44: Spectrum of the two studied modes.

$$F_{\text{aero}}(\mathbf{u}, \dot{\mathbf{u}}, \ddot{\mathbf{u}}) \approx -(\mathbf{K}_{\text{aero}}\ \mathbf{u} + \mathbf{C}_{\text{aero}}\ \dot{\mathbf{u}} + \mathbf{M}_{\text{aero}}\ \ddot{\mathbf{u}}). \tag{5.51}$$

where $\mathbf{M}_{\text{aero}}$, $\mathbf{C}_{\text{aero}}$, and $\mathbf{K}_{\text{aero}}$ are the mass, damping and stiffness added by the fluid. The ratio between the fluid and the structure masses is 1/400, so the mass added by the fluid is negligible and is not taken into account in the forcing term. In order to justify this assumption, a simple test case with the fluid at rest was carried out and showed that nozzle eigenfrequencies remain unchanged compared to the case without coupling. In addition, the added mass term always tends to reduce the frequency, so that it has no effect on the shift directions. The damping term has been neglected, being its influence on frequency of second-order. So, combining the Equations (5.50) and (5.51), results in

$$\mathbf{M}\ \ddot{\mathbf{u}} + (\mathbf{K} + \mathbf{K}_{\text{aero}})\ \mathbf{u} = 0. \tag{5.52}$$

We insist that the scope of these crude approximations is merely in order to have a very simple explanation for the different sign in the frequency shifts.

An increment in the global stiffness gives a higher eigenfrequency and viceversa. According to the perturbation theory, the eigenfrequency shift is given by

$$\delta\omega_i^2 = \frac{\psi_i^T \ \mathbf{K}_{\text{aero}} \ \psi_i}{\psi_i^T \ \mathbf{M} \ \psi_i}, \tag{5.53}$$

where $\delta\omega_i^2$ and ψ_i are the change in the square of the eigenvalue and the normalized vector of displacements for the mode i. As the denominator is always positive, only the sign of the numerator has to be determined. It can be shown that the numerator is the work $\mathcal{W}$ done by the fluid on the structure as it vibrates in the corresponding mode,

$$\psi_i^T \ \mathbf{K}_{\text{aero}} \ \psi_i = -\int_{\text{S}} (p_i - p_{ref}) \ (\hat{\mathbf{n}} \ \psi_i) \ \text{dS} = \mathcal{W} \tag{5.54}$$

where S and $\hat{\mathbf{n}}$ are the inner surface of the nozzle and its normal pointing to the inside. The wall pressure distribution on S for the unperturbed problem is p_{ref} and p_i is the pressure distribution corresponding to a small perturbation in the mode i.

Then, if the work done by the fluid is positive, the eigenfrequency is shifted to a higher value and conversely, if the work done is negative the eigenfrequency is shifted to a lower value.

Using the Equation (5.54), the work done by the fluid is 1.3 [J] for the bending mode and it is -53.1 [J] for the axial mode, which explains the sign of the frequency shifts shown in Figure (5.44).

Chapter 6

Extension to incompressible flows simulation's

In this chapter an alternative use of the FSI code developed in previous sections is shown. The simulation of FSI problems assuming incompressible viscous flows opens a wide range of problems that can be addressed, including biomechanics of heart valves, arteries, glaucoma drainage devices or engineered structures, such as bridges, buildings, membranes, etc. With all these potential uses in mind, in this chapter a first step in this direction is given. This initial development has been used in a collaborative work with a nano and micro medicine group (LabBiomens, 2011) in order to characterize an active microvalve being developed by the group.

6.1 Characterization of an active microvalve for glaucoma

The aim of this work is the characterization and simulation of a preliminary design of a new Glaucoma Drainage Device (GDD) for the treatment of glaucoma. This device is activated by means of a diaphragm, which produce a change in the hydraulic resistance, in order to achieve the desired intraocular pressure (IOP). The device is described in the patent of Guarnieri (2007) and the entire characterization work can be found in the work of Sassetti et al. (2011).

In Figure (6.1) a schematic diagram and the components that comprise the active valve are shown. The regulator was designed to control the IOP by varying its resistance to the flow by means of the deflection of the diaphragm. The regulator is conceptually a normally closed valve, with a small leakage flow. The hydraulic resistance of the regulator has a passive component due to

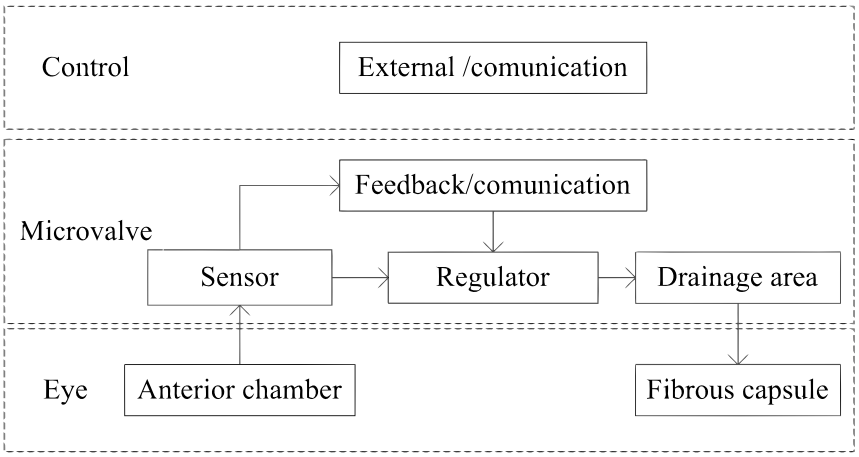

Figure 6.1: Schematic diagram of an active valve for glaucoma treatment.

the effects of fluid pressure on the diaphragm and an active component due to the change in the geometry, the deformation of the diaphragm, decreasing the hydraulic resistance between the input and output channels. In Figure (6.2) a cross section of the geometry of the regulator is shown and the channels (inlet and outlet) are connected by a deformable chamber.

For the characterization a fully coupled three-dimensional model is used. The fluid is described by the incompressible Navier-Stokes equations, written in an arbitrary time dependent coordinate system (ALE), which are implemented in a PETSc-FEM module. The equations to be solved are, Eq.(6.1) which express the conservation of mass for incompressible fluids and Eq.(6.2) the conservation of momentum.

$$\nabla \cdot \mathbf{u} = 0, \tag{6.1}$$

$$\rho \frac{\partial \mathbf{u}}{\partial t} + \rho[(\mathbf{u} - \mathbf{v}^*) \cdot \nabla]\mathbf{u} = \nabla \cdot \boldsymbol{\sigma} \tag{6.2}$$

where $\mathbf{u}$ is the fluid velocity vector, ρ the density, $\mathbf{v}^*$ the velocity of the moving

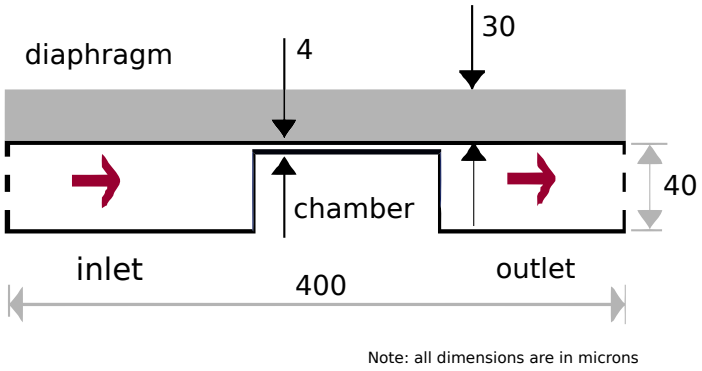

Figure 6.2: Geometry of the Regulator.

reference frame and $\boldsymbol{\sigma}$ stress tensor (pressure and viscous forces). Assuming that the fluid is Newtonian its constitutive equation is given by

$$\boldsymbol{\sigma} = \tau - p\mathbf{I} \quad \text{with} \quad \tau = \mu[\nabla\mathbf{u} + (\nabla\mathbf{u})^{\mathrm{T}}], \tag{6.3}$$

where μ the dynamic viscosity and p is the fluid pressure. In order to close the flow equations a set of boundary conditions are imposed

$$\begin{aligned} \boldsymbol{\sigma}\cdot\mathbf{n} &= \bar{\boldsymbol{t}} \quad \text{on} \quad \Gamma_{\mathrm{N}}, \\ \mathbf{u} &= \bar{\boldsymbol{u}} \quad \text{on} \quad \Gamma_{\mathrm{D}}, \end{aligned} \tag{6.4}$$

where Γ_N is a Neummann condition in the form of prescribed surface forces (traction) and Γ_D is a Dirichlet condition where the velocity is imposed. For the structure a constitutive linear elastic solid assuming large displacements and rotations is adopted. The description can be viewed in Section §2.2. The actuator has a thickness of 30 [μm] and is composed mainly of a conjugated polymer electrochemically deposited on a thin film conductor. The rigidity and the Poisson's ratio of the diaphragm are 450 [MPa] and 0.3 respectively.

This methodology allows to simulate both active and passive valves that have inherently three-dimensional flows. In the case of passive valves the fluid pressure deforms the diaphragm changing the hydraulic resistance and in the case of active valves the diaphragm deformation is prescribed as time function,

changing the hydraulic resistance.

The PETSc-FEM code has been used previously in the resolution of problems in microfluidics and electrokinetic flows (Kler et al., 2009, 2010). Therefore, in order to validate the proposed coupling algorithm when solving FSI problems in microfluidcs, the Ahmed Glaucoma Valve ®(AGV) is simulated with the geometry and mechanical properties described in Stay et al. (2005). Only half of the AGV geometry was simulated due to its symmetrical nature, reducing the size of the discrete problem. The valve is discretized using a structured mesh with 37500 linear hexahedral elements for the fluid and 15000 linear hexahedral elements for the structure (see Figure (6.3)). The problem was solved for several pressure drops through the valve, in order to construct a flow rate curve.

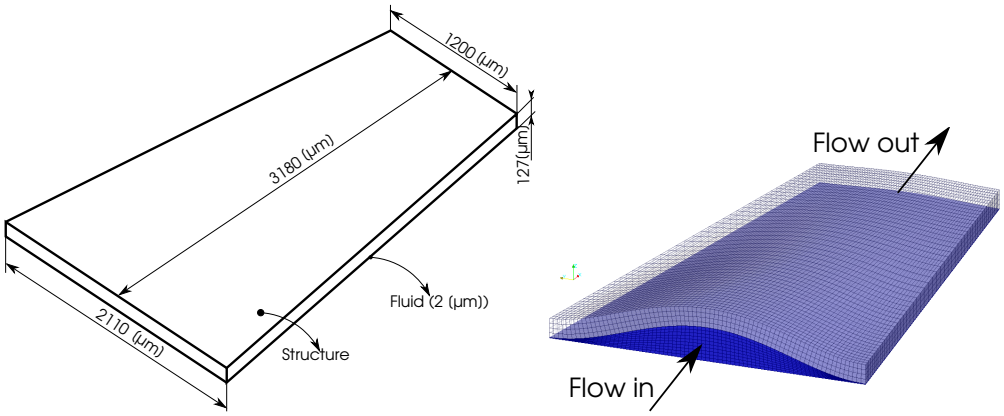

Figure 6.3: Diagram and Structured mesh in a deformed position of the AGV®valve.

Then, the characterization process of the active microvalve is carried out in two stages, first the passive resistance of the microvalve is obtained. In the second stage the active resistance of the microvalve is analyzed, i.e. when the diaphragm is actuated. In this case the diaphragm is deformed and the hydraulic resistance is decreased due to a change in the geometry of chamber.

To carried out this simulation the microvalve was discretized using a structured mesh with 147920 linear hexahedral elements for the fluid and 137388 linear hexahedral elements for the structure. Only half of the structure

mesh is shown in Figure (6.4) in order to obtain a clear view of the fluid mesh.

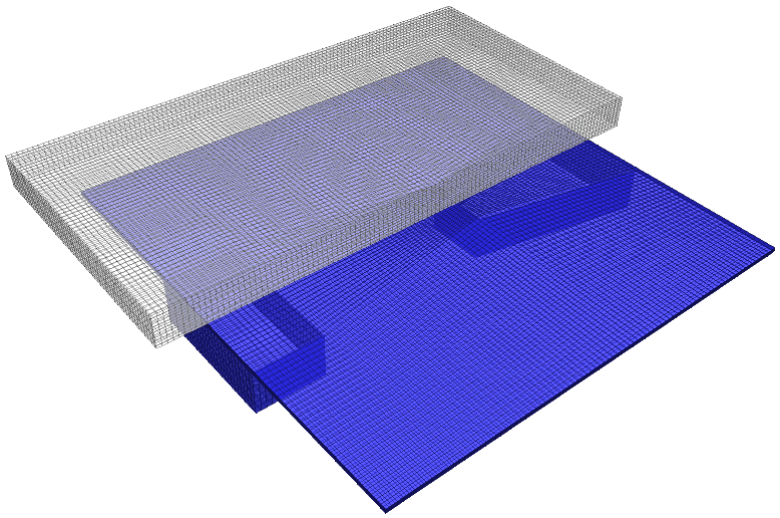

Figure 6.4: Structured mesh of the proposed microvalve.

To determine the variation in the passive hydraulic resistance of the microvalve due to fluid pressure over the diaphragm, the flow rates were measured for different pressure drops. The outlet pressure was set at 8 [mmHg] and the entry ranged from 15 [mmHg] to 60 [mmHg]. For each case, the flow rate and the maximum displacement of the diaphragm were obtained. The active hydraulic resistance was calculated by setting a pressure drop of 7 [mmHg] in the microvalve, varying the position of the diaphragm due to a deformation of the conjugate polymer. The numerical problem was carried out on a Beowulf cluster machine using 30 processors Intel®Pentium IV®Prescott 3GHz with 2 Gb of RAM, interconnected with two switch Gigabit Ethernet (1 Gbit/s), 3Com®Super Stack 3.

6.2 Results

In this section the results of the validation test and the characterization of the microvalve are shown. First, the passive hydraulic resistance is computed and then, the active hydraulic resistance. The equivalent circuit model is constructed using the obtained data from the previous simulations.

6.2.1 Validation Test

The results of the validation test proposed in the previous section are presented. Table (6.1) shows the experimental and numerical flow rate obtained by Stay et al. (2005) and the numerical flow rate obtained by Kara and Kutlar (2010) for AGV and they are compared with the results of PETSc-FEM. The time to obtain a steady state solution was around 20 minutes using 30 processors Intel®Pentium IV®Prescott 3GHz. In the range of normal operation of the valve the flow rate is similar to that obtained by Stay et al. (2005) in their experiments.

Table 6.1: Hydraulic resistance of Ahmed Glaucoma Valve®

Experim.		Stay et al.		Kara et al.		PetscFem	
Pressure	Flow rate	Pressure	Flow rate	Pressure	Flow rate	Pressure	Flow rate
[mmHg]	[μl/min]	[mmHg]	[μl/min]	[mmHg]	[μl/min]	[mmHg]	[μl/min]
5.20	1.54	5.80	1.55	5.37	1.6	5.80	1.90
7.40	2.51	6.52	2.51	7.74	2.5	7.01	3.81
8.51	4.95	7.71	4.96	8.51	5	8.00	5.87
9.70	9.97	9.21	9.98	9.25	10	9.00	8.71
10.50	19.95	11.02	19.96	11.29	20	11.00	17.80
10.81	24.91	11.64	24.98	11.82	25	11.50	20.00

The results of Table(6.1) are plotted in Figure (6.5).

6.2.2 Passive hydraulic resistance

In this subsection and the following, the results of the characterization process of the microvalve are presented. The Table(6.2) shows the flow rates for different pressure drops and can be concluded that the designed microvalve does not work as a passive pressure regulator, since the hydraulic resistance does not decrease with increasing IOP. The time to obtain the equilibrium state between pressure and elastic forces was around 25 minutes using 30 processors.

In Figure (6.8) the pressure distribution is plotted together with the velocity field in the center plane of the microvalve for a pressure drop of 52 [mmHg].

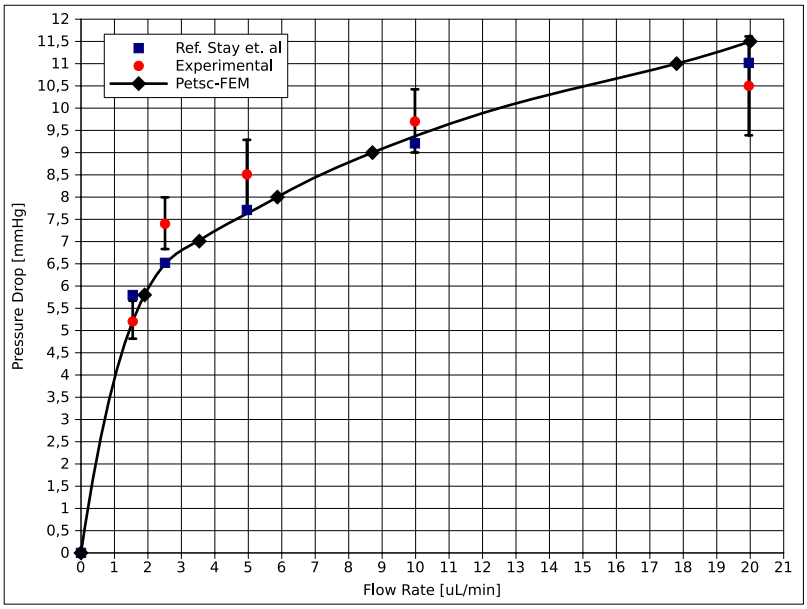

Figure 6.5: Flow thought the AGV as function of the pressure drop.

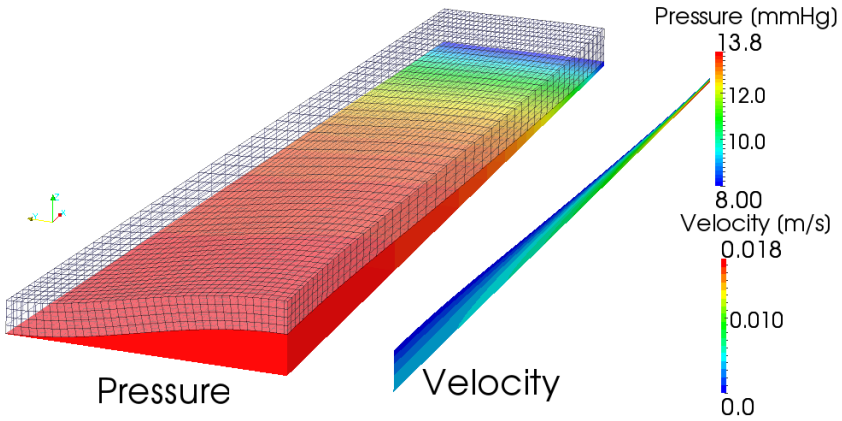

Figure 6.6: Pressure distribution and velocity field in the center plane for a pressure drop of 5.8 [mmHg].

6.2.3 Active hydraulic resistance

As was mentioned before, the deformation of the diaphragm reduces the hydraulic resistance of the microvalve by increasing the area of passage between the input and output channels.

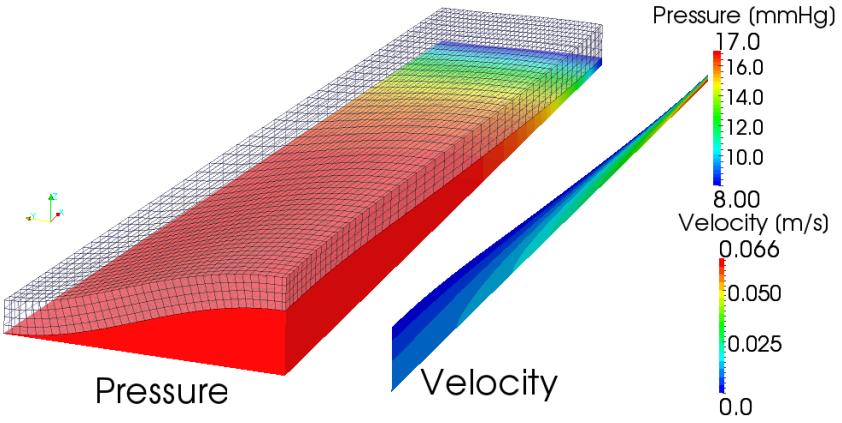

Figure 6.7: Pressure distribution and velocity field in the center plane for a pressure drop of 9 [mmHg].

Table 6.2: Passive hydraulic resistance

Intraocular Pressure [mmHg]	Displacement [μm]	Flow [μl/min]	Resistance [mmHg $\cdot$ min/μl]
15.00	0.024	0.54	13.08
22.50	0.049	1.12	12.96
30.00	0.074	1.72	12.80
37.50	0.100	2.32	12.72
45.00	0.125	2.94	12.59
52.50	0.151	3.56	12.50
60.00	0.176	4.20	12.38

To characterize the change in the hydraulic resistance, the flow rate through the valve has been measured for a set of diaphragm deformations, fixing the pressure drop to 7 [mmHg]. The time to reach the steady state was around 20 minutes using 30 processors.

In Table(6.3) the changes in the hydraulic resistance as a function of actuator deformation are shown.

The hydraulic resistance of the valve varies from 13.08 [mmHg $\cdot$ min/μl] to 0.36 [mmHg $\cdot$ min/μl] and the displacement of the diaphragm were in the range of 0 [μm] to 18.90 [μm]. In Figure (6.9) the streamlines for the maximum displacement of the diaphragm are shown and in Figure (6.10) is plotted the

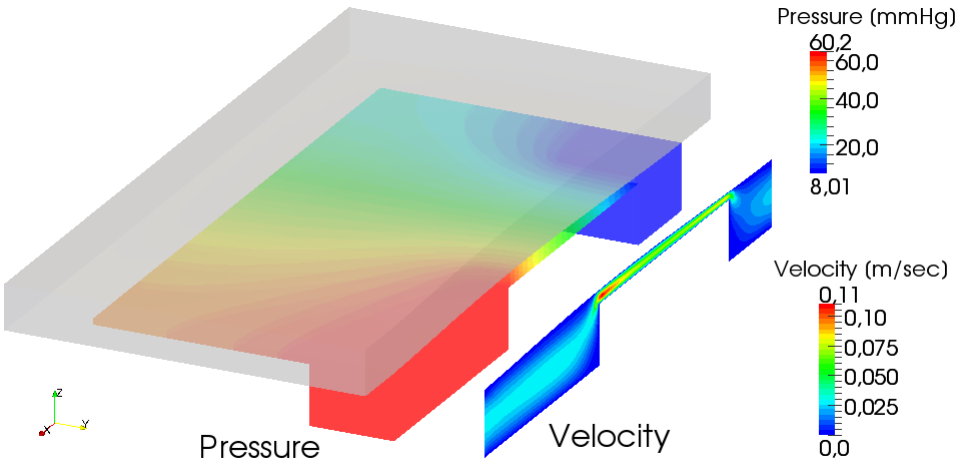

Figure 6.8: Pressure distribution and velocity field in the center plane.

Table 6.3: Active hydraulic resistance

Deformation actuator [%]	Displacement [μm]	Aqueous flow [μl/min]	Resistance [mmHg $\cdot$ min/μl]
0.00	0.024	0.54	13.08
0.30	2.67	1.34	5.22
0.40	3.57	1.73	4.05
0.50	4.50	2.19	3.20
1.00	9.32	5.80	1.21
2.00	18.90	19.44	0.36

pressure distribution together with the velocity field in the center plane of the microvalve.

The use of FEM allows the modeling and analysis of fluid structure interaction of complex 3D geometries that would be difficult to resolve otherwise, enabling the improvement of the design before its construction, reducing time and costs. It also facilitates the calculation of active and passive resistance of the regulator to incorporate in the equivalent circuit model. The parallel computation allows to compute efficiently the problem reducing dramatically the calculus time (from day to minutes).

The coupling algorithm used in this work, in contrast with that used by Kara

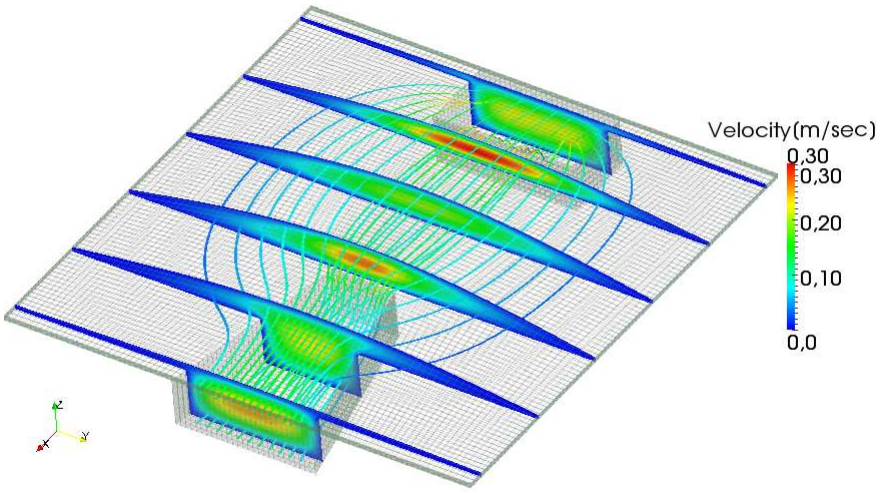

Figure 6.9: Streamlines for the maximum displacement of the diaphragm.

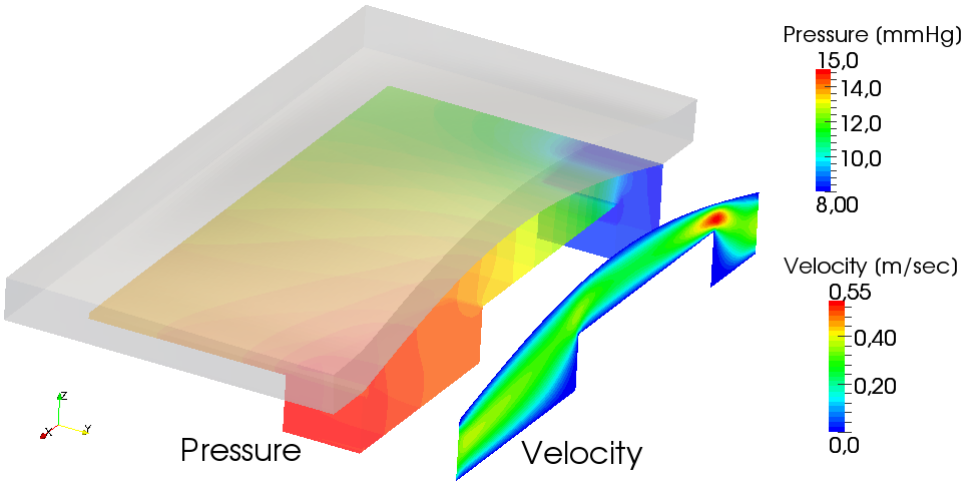

Figure 6.10: Pressure distribution and velocity field in the center plane.

and Kutlar (2010) takes into account the mechanical properties of the elastomer and the geometric changes of the valve during the deformation process. The FSI scheme allows to solve the problem using both weak or strong coupling. In this work, the flow characteristics and the stiffness of the membrane makes it sufficient to use a weak coupling strategy, without instability problems.

Chapter 7

Conclusion and contribution of the work

In this chapter, the contributions of the work and the research activities carried out during the course of this thesis are presented. Also, a brief discussion about the performed simulations and these results are exposed. Then, the guidelines about the future work are given in order to continue with development of a simulation tool for a wide range of FSI problems. Finally, the publications resulting from the research work carried out during this thesis are listed.

7.1 Conclusion of the work

In recent years, a substantial effort has been put into the numerical simulation of multiphysics systems. In particular, the interaction of a fluid with some movable or deformable structure has a historical and practical importance, and it has to be considered in the design of many engineering systems. Wherewith, the possibility to perform a numerical simulation of the whole coupled system has a significant importance, allowing to test a wide number of design parameters and having as result a detailed description of the fluid and the structure.

So, the general objective of this thesis was to obtain a simulation tool by means of the development and implementation of a coupling algorithm for existing PETSc-FEM modules. In order to couple the existing PETSc-

FEM modules, a partitioned algorithm was used (see Chapter 3). With this approach the systems to be solved are smaller and better conditioned that in the monolithic case, but requires a careful implementation in order to avoid serious degradation of the stability and accuracy. These drawbacks were overcome with the use of a structural predictor, which is sufficient to ensure the numerical stability in problems with a weak coupling between the fluid and the structure. In cases where a strong coupling between the systems exist, several stages by time steps must be used to ensure stability and accuracy of the solution.

The ALE formulation allows to use moving meshes in the numerical simulation, but some modifications are needed, as described in section §2.1. The fluid governing equations on an ALE reference frame have additional terms related to the mesh velocity and position, and an extra conservation law known as the DGCL must be satisfied in order to avoid the introduction of a numerical error due to the mesh movement. For this particular objective a new and original methodology for developing DGCL compliant formulations based on an AJF was implemented (see Chapter 4) and tested (see Section §5.4). This new methodology is not based on proposing a new temporal integration scheme and computing a set of unknown numerical coefficients in order to achieve compliance with the DGCL, but rather by averaging some geometrical quantities. These averages are computed exactly using the Gauss-Lobatto numerical quadrature and must be introduced in the volume terms as well as in the boundary terms. The AJF guarantees compliance with the DGCL criterion in the context of the ALE solutions of general advective-diffusive systems using classical temporal integration schemes and simplicial finite elements in 2D and 3D. The added cost is negligible and only involves a few changes at the elemental routine level. For the stabilization terms (SUPG and SC) the advective jacobians were transformed to ensure that the discrete formulation is ‘‘ALE invariant’’, in others words, for a given problem the same solution is obtained regardless of the mesh velocity.

Having implemented all the referent to the coupling algorithm and the AJF a set of validations test for the fluid solver and the structural solver, which are the foundations of the partitioned algorithm were performed. The fluid solver has been widely used on several previous works, so a steady state case

was performed. While for the structure, both static and dynamic cases with large deformations were performed. Then, the piston problem was solved in order to verify the issue about energy conservation in the coupling algorithm. This very simple problem from the computational point of view allows to understand the energy transfer trough the fluid-structure interface and to check the enhancement of the stability when a structural predictor or a stage loop are used.

The AJF developed in Chapter 4 was validated by solving a set of numerical test in 2D and 3D for different kind of problems. Also, the error introduced when the ALE formulation it is not DGCL compliant was established. Finally, the aeroelastic process developed during the starting phase of the rocket engine was analyzed with the developed FSI code using a weak coupling over the fluid and structure states. A comparative analysis of the parietal pressure of multiple TOP nozzle was carried out (§5.5.4) with the aim of validating the internal fluid flow model. The accuracy when computing the wall pressure distribution is very important because it is used in the aeroelasticity analysis, having a direct impact in computed eigenfrequencies of the coupled problem. Then, a modal analysis of the structure was performed via two different methods (FFT, GEPV) to obtain the eigenfrequencies of characteristic modes of the nozzle. The behavior of these modes was studied in the coupled case that represents the normal operation condition. It was verified that the effect of the coupling on the structure frequencies can not be neglected in this case.

In Chapter 6 a first step in the direction of using incompressible flows on FSI problems was given. The characterization and simulation of passive and active microvalves was performed. In the case of passive microvalves, the deformation of a membrane, due to a pressure gradient, allows the drainage of the fluid. Moreover, active microvalves varies the hydraulic resistance by means of a controlled deformation of a membrane allowing to control the IOP in a desired range. The use of FEM allows the modeling and analysis of fluid structure interaction of complex 3D geometries that would be difficult to resolve otherwise, enabling the improvement of the design before its construction, reducing time and costs. It also facilitates the calculation of active and passive resistance of the regulator. The parallel computation allows to compute efficiently the

problem reducing dramatically the computing time (from day to minutes).

7.2 Contributions of the work

A general contribution of this thesis was obtain a simulation tool by means of the development and implementation of a coupling algorithm for existing PETSc-FEM modules, with the aim of carry out reliable FSI simulations with the focus on the numerical stability of the simulations and its performance, using for this purpose distributed memory parallel platforms. A set of numerical simulations were performed in order to validate the numerical solvers and the coupling algorithm. In addition, with this work the following particular contribution were made

- The developing and implementation of a new methodology for obtain a DGCL compliant formulations based on Averaged ALE Jacobians Formulation (AJF), in the context of the FEM for general advective-diffusive systems on moving domains using an Arbitrary Lagrangian Eulerian.
- The extension of the AJF to the three point BDF, giving a wide range of possible applications.
- The numerical simulation of the start-up process of a rocket engine using the simulation tool developed in this work, analyzing the structural response under thrust and lateral loads, to obtain the frequency shifting due to the FSI coupling.
- The use of the FSI code on the simulation of a Glaucoma Drainage Device. The simulation of FSI problems assuming incompressible viscous flows opens a wide range of problems that can be addressed.

7.3 Future work

The algorithm and code developed, will be extended to the solution of FSI problems involving incompressible flows (Bathe et al., 1995; Bathe and Ledezma,

2007; Nobile, 2001; Förster et al., 2007; Degroote et al., 2008; Tezduyar et al., 2009) in order to obtain a code that can address the solution of a wide range of FSI problems. As in the case of compressible flows, incompressible flows must be stabilized using techniques like, Streamline-Upwind/Petrov-Galerkin (SUPG) for the advective terms; but in addition Pressure-Stabilizing terms like PSPG (for Pressure Stabilizing Petrov-Galerkin) must be added for stabilization of the incompressibility condition (Tezduyar and Sathe, 2003; Tezduyar and Osawa, 2000).

Also, the added mass effect (Nobile, 2001; Förster et al., 2007) will be investigated in order to obtain a stable algorithm to perform numerical FSI simulation with incompressible flows. When using a weak coupling algorithm the added mass effect can cause the divergence of the method and if a strong coupling is used, several stages are needed to reach the desired convergence. This effect becomes important in cases where the density of the fluid and structure are comparable, regardless of the time step chosen. Therefore is necessary to identify and understand what are the mathematical operators involved, in order to avoid numerical instability.

These developments will be implemented in PETSc-FEM (Storti et al., 2010) and oriented to the solution on distributed memory parallel platforms of the Beowulf Cluster (GNU/Linux OS) class, with particular emphasis on performance via parallel processing.

7.4 Publications

During the work on this thesis the following articles have been published or are going to be published in the following referred journals,

- **Sassetti, F.; Guarnieri, F.A.; Garelli, L.; Storti, M.A.**; Characterization and Simulation of an Active Microvalve for Glaucoma. *doi:10.1080/10255842.2011.585978. Computer Methods in Biomechanics and Biomedical Engineering.*

- **Storti, M.; Garelli, L.; Paz, R. R.**; A Finite Element Formulation Satisfying the Discrete Geometric Conservation Law Based on Averaged

Jacobians. *doi: 10.1002/fld.2669. International Journal for Numerical Methods in Fluids.*

- **Garelli, L.; Paz, R. R.; Storti, M.**; Fluid-Structure interaction study of the start-up of a rocket engine nozzle. *doi:10.1016/j.compfluid.2010.03.005. Computers & Fluids*, 39 (2010) 1208-1218.

- **Paz, R. R.; Storti, M.; Garelli, L.**; Local Absorbent Boundary Condition for Nonlinear Hyperbolic Problems with Unknown Riemann Invariants. *doi:10.1016/j.compfluid.2010.08.001. Computers & Fluids*, 40 (2010) 52-67.

In addition, the following book chapter has been written,

- **Garelli, L.; Paz, R.R.; Castro, H.G.; Storti, M.A.; Dalcín, L.D.** Fluid Structure Interaction and Galilean Invariance. Computational Fluid Dynamics: Theory, Analysis and Applications. *Nova Science Publishers, Inc.*. 2011. Pag.1 - 40. ISSN(978-1-61209-276-8)

Besides, several articles have been submitted and presented in conferences in different topics related with this thesis.

- **Sassetti, F.; Guarnieri, F.A.; Garelli, L.; Storti, M.A.**; Characterization and Simulation of an Active Microvalve for Glaucoma. *ENIEF 2011. Rosario, Argentina (Noviembre 2011).*

- **Sassetti, F.; Guarnieri, F.A.; Garelli, L.; Storti, M.A.**; Modelo Hidrodinámico para el Análisis del Sistema Ojo-Válvula en Pacientes con Glaucoma. *ENIEF 2011. Rosario, Argentina (Noviembre 2011).*

- **Storti, M.; Garelli, L.; Paz, R. R.;** ; A Finite Element Formulation Satisfaying the Discrete Geometric Conservation Law Based on Averaged Jacobians. *MECOM 2010 - CILAMCE 2010. Buenos Aires, Argentina. (Noviembre 2010).*

- **Garelli, L.; Paz, R. R.; Storti, M.**; Geometric Conservation Law in 2D Advection-Diffusion Problem. *II Congreso de Matemática Aplicada, Computacional e Industrial. Rosario, Argentina. (Diciembre 2009).*

- **Paz, R. R.; Storti, M.; Garelli, L.**; Absorbent Boundary Condition for General Nonlinear Hyperbolic PDE's with Unknown Riemann Invariants. *II Congreso de Matemática Aplicada, Computacional e Industrial. Rosario, Argentina. (Diciembre 2009)*

- **Garelli, L.; Paz, R. R.; Storti, M.**; Geometric Conservation Law in ALE Formulations. *XVIII Congreso sobre Métodos Numéricos y sus Aplicaciones. Tandil, Argentina. (Noviembre 2009).*

- **Paz, R. R.; Storti, M.; Garelli, L.**; Local Absorbent Boundary Condition for Nonlinear Hyperbolic Problems with Unknown Riemann Invariants. *XVIII Congreso sobre Métodos Numéricos y sus Aplicaciones. Tandil, Argentina. (Noviembre 2009).*

- **Garelli, L.; Paz, R. R.; Storti, M.**; Interacción Fluido Estructura en Flujo Compresible en Régimen Supersónico. Pag. 505-518. *XVII Congreso sobre Métodos Numéricos y sus Aplicaciones. San Luis, Argentina. (Noviembre 2008).*

- **Garelli, L.; Paz, R. R.; Ríos, G.; Storti, M.; Nigro, N. M.**; Explosiones de Gas en Recintos Cerrados. Pag. 938-961. *XVI Congreso sobre Métodos Numéricos y sus Aplicaciones. Córdoba, Argentina. (Octubre 2007).*

Appendix A

Resumen extendido en castellano

A.1 Interacción Fluido-Estructura empleando una formulación Lagrangiana Euleriana Arbitraria

A.1.1 Motivación

La interacción de un fluido con una estructura móvil o deformable tiene una importancia práctica y ha sido motivo de grandes estudios y análisis. A este fenómeno se lo conoce como FSI (por su siglas en inglés Fluid Structure Interaction) y su impacto tiene que ser considerado durante el diseño de diferentes sistemas. En ingeniería aeronáutica o aeroespacial, un fluido a alta velocidad y presión puede causar la deformación de una estructura, como se puede observar en la secuencias de imágenes de la Fig.(A.1), la cuales fueron tomadas por la NASA en 2010 durante el lanzamiento del transbordador. Pero, si las interacción es lo suficientemente intensa puede ocasionar la inestabilidad del sistema, lo cual es conocido como ‘‘flutter’’ y puede resultar en la falla del sistema o la estructura.

En ingeniería civil, las vibraciones inducidas por el viento pueden causar el colapso de una construcción, siendo uno de los ejemplos más estudiado el

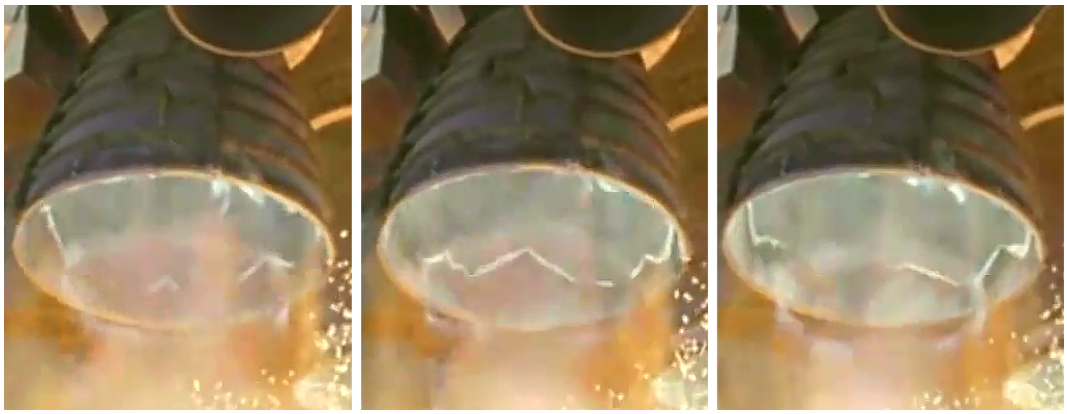

Figure A.1: Motores principales del transbordador durante el encendido (NASA 2010).

puente de Tacoma, el cual colapso con vientos de 64 [km/h], el 7 de Noviembre de 1940.

Otra área importante donde FSI desarrolla un papel fundamental es, por ejemplo, la ingeniería biomédica, donde las pulsaciones del flujo sanguíneo pueden ocasionar la ruptura de una aneurisma aórtica abdominal o cerebral, implicando un gran riesgo para el paciente.

En los ejemplos mencionados anteriormente es muy difícil determinar a priori los efectos del fluido sobre la estructura, siendo éstos detectados durante los ensayos o utilización del sistema. Cuando se conoce previamente que la interacción es lo suficientemente fuerte como para producir una deformación considerable en la estructura, se llevan a cabo una serie de intensivos ensayos experimentales. El proceso de puesta a punto de estos ensayos demanda muchísimo tiempo debido a que tienen que reproducir fielmente las condiciones de vuelo, en caso del ‘‘flutter’’ de un ala o las condiciones ambientales en el caso de puentes; y ciertos casos son imposible de reproducir en un túnel de viento.

Es en este contexto donde la posibilidad de realizar una simulación numérica de todo el sistema tiene una importancia significativa, permitiendo probar y analizar una variedad de parámetros de diseño, obteniendo como resultado una descripción detallada del fluido (p. ej., velocidades, presión, intensidad de la turbulencia, etc.) y de la estructura (p. ej., tensiones, deformaciones,

Figure A.2: Colapso del puente Tacoma (1940).

desplazamientos, etc.). Pero previo a realizar cualquier simulación numérica, son necesarias las ecuaciones que gobiernan al sistema. Estas ecuaciones describen la física subyacente y son generalmente expresadas como un conjunto de ecuaciones diferenciales parciales. Por un lado están las ecuaciones para el fluido, en general las ecuaciones de Navier-Stokes (NS) (Batchelor, 1967; Acheson, 1990), y por otro lados están las ecuaciones para la estructura, derivadas a partir de la teoría de elasticidad (Timoshenko, 1970; Atkin and Fox, 2005). En algunos casos estas ecuaciones son simplificadas empleado modelos. (p. ej., modelos de turbulencia, funciones de pared, materiales elástico lineales, etc.) o hipótesis (p. ej., fluido incompresible, fluido inviscido, pequeñas deformaciones, etc.) con el fin de reducir la complejidad de las ecuaciones a resolver.

Estas ecuaciones deben ser discretizadas tanto espacialmente como temporalmente, utilizando métodos como Elementos Finitos (MEF), Volúmenes Finitos (MVF) o Diferencias Finitas (MDF), y así obtener un sistema discreto de ecuaciones a ser resultas en una computadora o en un ‘‘cluster’’ de computadoras. El tratamiento numérico de las ecuaciones de la mecánica de fluidos y elasticidad son conocidas como, Fluido-Dinámica Computacional (CFD, por sus siglas en inglés) y Dinámica Estructural Computacional (CSD, por sus siglas en inglés), respectivamente. Ambas áreas han evolucionado lo suficiente en las últimas décadas como para abordar la resolución de problemas acoplados, como ser problemas de FSI. Pero este tipo de problemas trae nuevas complicaciones y complejidades a ser consideradas, como ser la técnica de acoplamiento, la interacción dinámica, las diferentes escalas de tiempo y longitud de los subsistemas involucrados, lo cual hace que la resolución de problemas de FSI sea

más dificultosa que la resolución del fluido y la estructura por separado. Con ésto en mente y debido al desafío que representa, las contribuciones en el área están creciendo a gran ritmo, estando en los objetivos de esta tesis contribuir a la expansión del conocimiento en el área.

A.1.2 Alcances y objetivos

En los últimos años, se ha puesto un esfuerzo sustancial en resolver este tipo de problema, debido a que representa en sí un gran desafío. Por lo tanto, uno de los objetivos de esta tesis es el desarrollo e implementación de un algoritmo de acople para módulos o códigos existentes, con el objetivo de realizar simulaciones de FSI haciendo foco en la utilización del cálculo distribuido.

Una importante consideración a ser tenida en cuenta cuando se realizan simulaciones de FSI, es la elección de la descripción cinemática del fluido a los fines de permitir la presencia de contornos móviles. En general, en problemas de flujos de fluido resueltos en mallas fijas es utilizada una descripción Euleriana. Esto facilita el tratamiento de las ecuaciones, como así también la simulación de flujos turbulentos, pero su principal desventaja es la dificultad en seguir una interfaz entre diferentes medios (e.g., interfaz fluido-solido). Una alternativa es emplear una descripción Lagrangiana, en la cual cada nodo de la malla sigue a una partícula material durante su movimiento. Esta descripción permite el seguimiento de interfaces entre diferentes medios, pero su debilidad se encuentra en el tratamiento de mallas con gran distorsión. Una alternativa es utilizar una descripción Lagrangiana Euleriana Arbitraria (ALE, por sus siglas en inglés), la cual puede manejar problemas con contornos móviles. La idea detrás de la formulación ALE es la introducción de una malla que se mueva con una velocidad independiente de la velocidad de las partículas materiales.

Cuando es empleada una formulación del tipo ALE, términos adicionales relacionados con la velocidad y posición de la malla son introducidos. Además, el movimiento de la malla del fluido produce un cambio de volumen de los elementos en el tiempo, lo cual agrega una ley de conservación extra a satisfacer a los fines de no introducir errores numéricos. Esta ley es conocida como Ley de Conservación Geométrica Discreta (DGCL, por sus siglas en inglés) y existe una

gran cantidad de literatura dedicada al impacto que tienen el cumplimiento de la DGCL en la estabilidad del esquema numérico y en la precisión del integrador temporal. En estos artículos se ha probado que satisfacer la ley de conservación geométrica es una condición necesaria y suficiente para que cualquier esquema ALE mantenga en mallas móviles las propiedades de estabilidad no-lineales que tiene en malla. Sin embargo, en muy pocos trabajos se ha propuesto una metodología para obtener un esquema que cumpla con la DGCL, sin cambiar el integrador temporal.

En esta tesis es presentada una nueva y original metodología para desarrollar formulaciones que satisfagan la DGCL, basada en el promediado de los jacobianos (Average Jacobians Formulation (AJF)) sin necesidad de cambiar el integrador temporal. Este desarrollo en llevado a cabo en el contexto de los elementos finitos (MEF) para sistemas generales advectivos-difusivos en mallas móviles usando una formulación del tipo ALE. Esta metodología es desarrollada para integradores temporales de la familia-θ y para BDF (Backward Differential Formula) de tres puntos, dan un amplio espectro de posibles aplicaciones.

Las implementaciones son realizadas en PETSc-FEM (Storti et al., 2010), el cual es un código de elementos finitos, multifísico, de propósitos generales , paralelo, basado en PETSc (Balay et al., 2011). Esta escrito en C++ con programación orientada a objetos, buscando siempre la eficiencia en la programación. PETSc-FEM puede correr en paralelo usando paso de mensaje (MPI), lo cual permite la solución de grande sistemas de ecuaciones no-lineales.

A.2 Ecuaciones de gobierno

Las ecuaciones de gobierno para la dinámica de fluidos, la estructura y el movimiento de malla serán revisadas brevemente en las siguientes secciones. Éstas ecuaciones son implementadas en PETSc-FEM en módulos especializados.

A.2.1 Dinámica de fluidos

El comportamiento dinámico de un flujo de fluidos esta gobernado por las ecuaciones de Navier-Stokes, las cuales son un conjunto de leyes de conservación

acopladas. Estas pueden ser enumeradas como

- Conservación de masa,
- Conservación de momento,
- Conservación de energía.

Otra ley adicional debe ser agregada, si el problema es resulto en un marco de referencia móvil y se emplea una formulación del tipo ALE,

- Ley de conservación geométrica.

La ecuaciones de Navier-Stokes pueden ser simplificadas, con el objetivo de reproducir algún tipo de flujo particular, como ejemplo, si la viscosidad es considerada nula el fluido es tratado como inviscido. En esta tesis el flujo es considerado compresible y viscoso, y se describe como un sistema advectivo-difusivo general, como el fin de simplificar su interpretación.

A.2.2 Sistema Advectivo-Difusivo general

La derivación de las ecuaciones se hace para un sistema advectivo-difusivo general (Donea, 1983; Lesoinne and Farhat, 1996; Donea and Huerta, 2003). Estas ecuaciones pueden ser escritas en una forma compacta

$$\frac{\partial U_j}{\partial t} + \left(\mathcal{F}^c_{jk}(\mathbf{U}) - \mathcal{F}^d_{jk}(\mathbf{U}, \nabla\mathbf{U})\right)_{,k} = 0, \quad \text{in } \Omega^t \quad \forall t \in (0, \mathcal{T}) \tag{A.1}$$

donde $1 \leq k \leq n_d$, n_d es el número de dimensiones espaciales, $1 \leq j \leq m$, m es la dimensión del vector de estado (e.g. $m = n_d + 2$ para flujo compresible), t is time, $(\ )_{,k}$ denota derivada con respecto al k-esima dimensión espacial, $\mathbf{U} = (\rho, \rho\mathbf{u}, \rho e)^t \in \mathbb{R}^{n_d}$ es el vector de estado incógnita expresado en términos de variables conservativas. Donde ρ , $\mathbf{u}$ y e representan la densidad, el vector velocidad y la energía específica total respectivamente, y $\mathcal{F}^{c,d}_{jk} \in \mathbb{R}^{m \times n_d}$ son los flujos convectivos y difusivos. Condiciones de borde apropiadas, como así también una condición inicial debe ser impuesta.

Este conjunto de ecuaciones es cerrado por una ecuación de estado, siendo para un gas politrópico

$$p = (\gamma - 1)[\rho e - \frac{1}{2}\rho||\mathbf{u}||^2], \tag{A.2a}$$

$$T = C_v[e - \frac{1}{2}\rho||\mathbf{u}||^2], \tag{A.2b}$$

donde γ es la relación de calores específicos y C_v es el calor específico a volumen constante. En flujos viscoso, el tensor de tensiones $\bar{\bar{\tau}}$ es definido para flujos Newtonianos como

$$\tau_{ij} = 2\mu\varepsilon_{ij}(\mathbf{u}) + \lambda(\nabla \cdot \mathbf{u})\delta_{ij}, \tag{A.3}$$

donde la hipótesis de Stokes es

$$\lambda = -\frac{2}{3}\mu, \tag{A.4}$$

y el tensor de tasa de deformación es

$$\varepsilon_{ij}(\mathbf{u}) = \frac{1}{2}\left(\frac{\partial u_i}{\partial x_j} + \frac{\partial u_j}{\partial x_i}\right). \tag{A.5}$$

Finalmente, se asume que la viscosidad dinámica es función de la temperatura y viene dada por la ley de Sutherland, la cual da para un gas ideal

$$\mu = \mu_0 \left(\frac{T}{T_0}\right)^{3/2} \frac{T_0 + 110}{T + 110}, \tag{A.6}$$

donde μ_0 es la viscosidad a una temperatura de referencia T_0.

A.2.3 Dinámica estructural

A continuación se dará una introducción a las ecuaciones que gobiernan la dinámica estructural. El objetivo de este trabajo está en abordar la resolución de problemas de FSI, por lo cual la parte estructural será brevemente cubierta. Explicaciones más detalladas sobre mecánica del continuo se pueden encontrar en Marsden and Hughes (1983); Landau et al. (1986) y respecto a las aproxima-

ciones numéricas de esos esquemas en Hughes (1987a); Zienkiewicz and Taylor (2005).

La dinámica estructural esta gobernada por la conservación de momento lineal, una ecuación constitutiva que relaciona las tensiones con las deformaciones y algunas relaciones cinemáticas. Uno de los punto claves de esta tesis es poder resolver una gran variedad de problemas de FSI, por lo cual es necesario un modelos estructural que admita grandes deformaciones. Sin embargo, es considerado un modelo elástico lineal para el material.

La estructura se describe por un vector de desplazamientos $\mathbf{z}$, la velocidad material $\mathbf{v}_s = \frac{\mathrm{d}\mathbf{z}}{\mathrm{dt}}$, la densidad del material ρ_s y el tensor de tensiones de Cauchy $\bar{\bar{\sigma}}_s$, formulado en una descripción Langrangiana, con respecto al estado inicial Ω_s^0, tenemos que

$$\rho_s \frac{\mathrm{d}^2\mathbf{z}}{\mathrm{dt}^2} - \nabla \cdot \bar{\bar{P}} = \rho_s \mathbf{b} \ \text{ in } \ \Omega_\mathrm{s}^0 \ \ \forall \ \ \mathrm{t} \in (0, \mathcal{T}), \tag{A.7}$$

donde el tensor

$$\bar{\bar{P}} = J\bar{\bar{\sigma}}_s \bar{\bar{F}}^{-T}, \tag{A.8}$$

es conocido como el primer tensor de Piola-Kirchhoff y

$$\bar{\bar{F}} = \bar{\bar{I}} + \nabla\mathbf{z}, \tag{A.9}$$

es el tensor del gradiente de deformación y J es el determinante jacobiano.

Para una conveniente especificación de la ecuación constitutiva, el segundo tensor de tensiones de Piola-Kirchhoff $\bar{\bar{S}}$ es introducido y se relaciona con el primer tensor de tensiones de Piola-Kirchhoff por $\bar{\bar{S}} = \bar{\bar{F}}^{-1}\bar{\bar{P}}$.

Para un material elástico-lineal isotrópico, la ecuación constitutiva puede ser expresada como

$$\bar{\bar{S}} = \lambda_s(\mathrm{tr}\bar{\bar{\mathcal{E}}})\bar{\bar{\mathrm{I}}} + 2\mu_\mathrm{s}\bar{\bar{\mathcal{E}}}, \tag{A.10}$$

la cual relaciona el segundo tensor de tensiones de Piola-Kirchhoff con el tensor de deformaciones de Green-Lagrange $\bar{\bar{\mathcal{E}}}$ por medio de las constantes de Lamé

λ_s y μ_s. EL tensor de deformaciones de Green-Lagrange es definido como

$$\bar{\bar{\mathcal{E}}} = \frac{1}{2}\left(\nabla \mathbf{z} + \nabla \mathbf{z}^T + \nabla \mathbf{z} \cdot \nabla \mathbf{z}^T\right) \tag{A.11}$$

el cual se puede escribir como

$$\bar{\bar{\mathcal{E}}} = \frac{1}{2}\left(\bar{\bar{F}}^T \bar{\bar{F}} - \bar{\bar{I}}\right) \tag{A.12}$$

A.2.4 Dinámica de mallas

Como fue mencionado en las secciones previas, en problemas de FSI el fluido interactúa con la estructura, la cual se deforma debido a las fuerzas producidas por el fluido, produciendo un cambio en el domino de fluido. En el problema discreto un cambio en el domino debe ser seguido por un cambio en la discretización. Esta nueva discretización puede ser realizada mediante un remallado o a través de una reposicionamiento de los nodos.

En ésta tesis se emplea un proceso de reposicionamiento para actualizar las coordenadas nodales de la malla del fluido, en respuesta a la deformación del dominio, mientras se mantiene la topología sin cambio. Existen varias técnicas para producir el reposicionamiento y la elección dependerá de cuan importante es la deformación. Una alternativa robusta es la aproximación elástico lineal, donde la malla del fluido obedece la ecuación de elasticidad lineal (Stein et al., 2004) para así obtener un campo de desplazamientos suave.

Las ecuaciones que describen un medio elástico bajo la hipótesis de pequeñas deformaciones y sin fuerzas externas son

$$\nabla \cdot \bar{\bar{\sigma}} = 0, \tag{A.13a}$$

$$\bar{\bar{\sigma}} = \lambda_s(\mathrm{tr}\bar{\bar{\mathrm{E}}})\bar{\bar{\mathrm{I}}} + 2\mu_s\bar{\bar{\mathrm{E}}}, \tag{A.13b}$$

$$\bar{\bar{E}} = \frac{1}{2}\left(\nabla \mathbf{x} + \nabla \mathbf{x}^T\right), \tag{A.13c}$$

donde $\mathbf{x}$ es el campo de desplazamiento y para las constantes λ_s y μ_s se puede escribir

$$\mu_s \nabla^2 \mathbf{x} + (\lambda_s + \mu_s)\nabla(\nabla \cdot \mathbf{x}) = 0. \tag{A.14}$$

En esta aproximación las constantes de Lamé dependen del módulo de Young y del coeficiente de Poisson, con lo cual se puede definir un módulo de Young variable a los fines de evitar severas deformaciones de la malla en regiones críticas. Esta alternativa con un módulo de elasticidad variable es la más empleada en lo ejemplos realizados en la tesis.

A.3 Estrategia de acople para FSI

A continuación se describirá brevemente las estrategias usadas para realizar el acople entre el fluido, la estructura y el movimiento de malla. Para llevar a cabo dicha tarea, se puede elegir entre diferentes estrategias, teniendo cada una de ellas sus pros y contras.

A.3.1 Estrategias de acople particionado y monolítico

Con el incremento de problemas de multifísica a ser resueltos, una gran variedad de estrategias de acople han sido propuestas, las cuales se pueden encontrar en diferentes publicaciones y libros Bungartz et al. (2006); Ohayon and Kvamsdal (2006); Galdi and Rannacher (2010); Bazilevs et al. (2011), pudiéndose clasificar en los siguiente grupos (Ver Figura (A.3)).

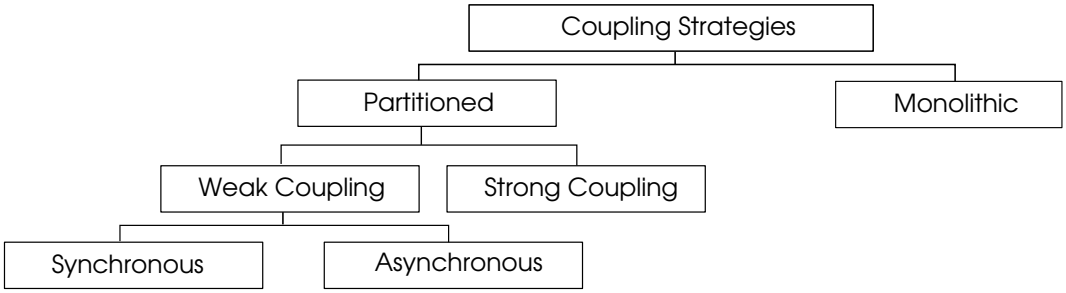

Figure A.3: Estrategia de acople.

En el tratamiento monolítico las ecuaciones que gobiernan el flujo de fluido y los desplazamientos son resueltas simultáneamente con un solver único (Michler et al., 2004; Idelsohn et al., 2009; Ryzhakov et al., 2010). Las ventajas de este tratamiento son la robustez y precisión, debido a que todas las componentes se

avanzan simultáneamente en el tiempo y aseguran la conservación de energía del sistema, pero la solución del sistema de ecuaciones discreto requiere resolvedores sofisticados para grandes sistemas no lineales, como se menciona en Hron and Turek (2006). Además, es muy difícil reutilizar códigos existentes, lo cual hace necesario el desarrollo de gran parte del código.

En el tratamiento particionado, resolvedores independientes son utilizados para resolver cada uno de los problemas involucrados (fluido, estructura y movimiento de malla) . El proceso de interacción es llevado a cabo mediante del intercambio de información a través de la interfaz fluido/estructura de una manera escalonada. El solver estructural establece la posición y velocidad de la interfaz, mientras el solver del fluido establece la presión y las fuerzas de corte en la interfaz. La principal ventaja del tratamiento particionado, por lo cual se volvió tan popular, es la existencia de solver optimizados para cada subproblema, pudiendo ser reutilizados y acoplados. Los sistemas de ecuaciones a ser resuelto son menores y mejor condicionados, pero no todas son ventajas, esta aproximación requiere de una cuidadosa implementación con el objetivo de no tener una seria degradación de la estabilidad y precisión.

A.3.2 Estrategia de acoplamiento particionado

A continuación se describirá el algoritmo temporal que realiza el acople entre la estructura y el fluido. Durante el proceso iterativo tres códigos CFD (Computational Fluid Dynamics), CSD (Computational Structure Dynamics) y CMD (Computational Mesh Dynamics), se están ejecutando simultáneamente.

El esquema básico de acople procede de la siguiente forma:

i) Transferir el movimiento de la interfaz del sólido al fluido.

ii) Actualizar la posición de los nodos del fluido, en base al desplazamiento de la interfaz.

iii) Avanzar temporalmente el fluido y calcular las nuevas presiones.

iv) Convertir las nuevas presiones en carga estructural.

v) Avanzar temporalmente la estructura bajo las nuevas cargas del fluido.

A partir de esta descripción básica se puede obtener diferentes esquemas de acople, en función a como se realice la predicción de los desplazamientos estructurales.

A.4 Ley de conservación geométrica

En esta sección se describe brevemente una nueva metodología para obtener formulaciones que cumplan con la DGCL, en el contexto de MEF para sistemas advectivo-difusivos generales en mallas móviles. Existe una gran cantidad de bibliografía referida al impacto de la DGCL en la estabilidad y precisión de los integradores temporales. Sin embargo, muy pocos trabajos proponen una metodología para obtener esquemas que cumplan con la DGCL. En esta tesis es presentado un esquema que cumple con la DGCL, basado en el promediado de Jacobianos (AJF). Esta nueva metodología es aplicada a la familia θ de integradores temporales.

A.4.1 Formulación con jacobianos promediados (AJF)

Se dice que una formulación discreta satisface la DGCL si resuelve exactamente un estado constante para un movimiento de malla general. Como se mencionó anteriormente, los efectos del cumplimiento de la DGCL es un tema abierto, pero es recomendado en diversos trabajos (Guillard and Farhat, 2000; Formaggia and Nobile, 2004) emplear esquemas que cumplan con la DGCL, ya que esto podría mejorar la estabilidad y precisión.

Reemplazando $U_j =$ por una constante y luego de algunas manipulaciones se puede mostrar que la DGCL se satisface si

$$\int_{\Omega^{n+1}} w \, \mathrm{d}\Omega - \int_{\Omega^n} w \, \mathrm{d}\Omega = \Delta t \int_{\Omega^{n+\theta}} v_k^* \, w_{,k} \, \mathrm{d}\Omega. \tag{A.15}$$

Una restricción similar se mantiene para los términos de contorno. Los términos de estabilización normalmente satisfacen la DGCL automáticamente, ya que involucran derivadas del vector de estados, los cuales son nulos para un campo constante.

Notar que en la ecuación previa la igualdad se mantiene si el término derecho es evaluado como una integral en vez de ser evaluado en $t^{n+\theta}$, p. ej. siempre se cumple que

$$\int_{\Omega^{n+1}} w \,\mathrm{d}\Omega - \int_{\Omega^n} w \,\mathrm{d}\Omega = \int_{t^n}^{t^{n+1}} \left\{ \int_{\Omega^t} v_k^* \, w_{,k} \,\mathrm{d}\Omega \right\} \mathrm{d}t. \tag{A.16}$$

Transformando el integrando del término derecho al dominio de referencia Ω^ξ obtenemos

$$\begin{aligned} \int_{t^n}^{t^{n+1}} \left\{ \int_{\Omega^t} v_k^* \, w_{,k} \,\mathrm{d}\Omega \right\} \mathrm{d}t &= \int_{t^n}^{t^{n+1}} \left\{ \int_{\Omega^\xi} v_k^* \frac{\partial w}{\partial \xi_l} \frac{\partial \xi_l}{\partial x_k} J \,\mathrm{d}\Omega^\xi \right\} \mathrm{d}t, \\ &= \int_{\Omega^\xi} v_k^* \frac{\partial w}{\partial \xi_l} \int_{t^n}^{t^{n+1}} \left(\frac{\partial \xi_l}{\partial x_k} J \right)^t \mathrm{d}t \,\mathrm{d}\Omega^\xi, \\ &= \int_{\Omega^\xi} v_k^* g_k^{n+\theta} J^{n+\theta} \,\mathrm{d}\Omega^\xi. \\ &= \int_{\Omega^{n+\theta}} v_k^* g_k^{n+\theta} \,\mathrm{d}\Omega, \end{aligned} \tag{A.17}$$

donde g_k es la *interpolación promediada de la función gradiente*

$$\begin{aligned} g_k^{n+\theta} &= (J^{n+\theta})^{-1} \bar{Q}_{lk}^{n+1/2} \frac{\partial w}{\partial \xi_l}, \\ \bar{Q}_{lk}^{n+1/2} &= \int_{t^n}^{t^{n+1}} Q_{lk}^t \,\mathrm{d}t, \\ Q_{lk}^t &= \left(J \frac{\partial \xi_l}{\partial x_k} \right)^t. \end{aligned} \tag{A.18}$$

El esquema propuesto es luego reemplazado en el operador correspondiente $A(w, U^{n+\theta})$

$$A^{\mathrm{GCL}}(w, U^{n+\theta}) = - \int_{\Omega^{n+\theta}} \left[\mathcal{F}_{jk}^c - v_k^* U_j - \mathcal{F}_{jk}^d \right]\Big|_{t^{n+\theta}} \, g_k^{n+\theta} \,\mathrm{d}\Omega, \tag{A.19}$$

Una modificación similar debe ser introducida en los términos de contorno $B(w, U)$.

A.4.2 Evaluación de la interpolación promediada de la función gradiente

Cada componente x_k es una función lineal del tiempo dentro de cada paso de tiempo, luego la derivada espacial ($\partial x_k/\partial \xi_l$) también son funciones lineales y los determinantes J son polinomios de grado n_d. También, las componentes de la transformación inversa $\boldsymbol{\xi} \rightarrow \mathbf{x}$ pueden ser determinadas desde la inversa de la transformación directa $\mathbf{x} \rightarrow \boldsymbol{\xi}$ como

$$\begin{aligned} \frac{\partial \xi_l}{\partial x_k} &= \left(\frac{\partial \mathbf{x}}{\partial \boldsymbol{\xi}}\right)^{-1}_{lk}, \\ J\frac{\partial \xi_l}{\partial x_k} &= (-1)^{k+l}\,\text{minor}\left(\frac{\partial \mathbf{x}}{\partial \boldsymbol{\xi}}\right)_{kl}, \end{aligned} \tag{A.20}$$

donde $\text{minor}(\mathbf{A})_{ij}$ es el determinante de la submatriz $\mathbf{A}$ cuando la fila i y la columna j han sido eliminadas, quedando polinomios de orden $n_d - 1$.

La metodología propuesta utiliza un esquema de integración de mayor orden para (A.18), de manera que la DGCL se satisface para cualquier valor de θ en cualquier dimensión. Este método puede ser fácilmente extendido a otro integradores temporales.

Para la evaluación de $g_k^{n+\theta}$ se podría emplear el método de integración de Gauss, pero normalmente los Jacobianos y determinantes son conocidos en t^n y t^{n+1} ya que son necesarios para el cálculo del término temporal, por lo tanto sería mas apropiado el método de integración de Gauss-Lobatto, el cual involucra solo los extremos del intervalo. Este método integra exactamente polinomios de hasta grado $2n-3$ donde n es el número de puntos de integración.

$$g_k^{n+\theta} = \begin{cases} \dfrac{\Delta t}{2J^{n+\theta}}\left[Q_{lk}^n + Q_{lk}^{n+1}\right]\dfrac{\partial w}{\partial \xi_l}, & \text{in 2D,} \\ \dfrac{\Delta t}{6J^{n+\theta}}\left[Q_{lk}^n + 4Q_{lk}^{n+1/2} + Q_{lk}^{n+1}\right]\dfrac{\partial w}{\partial \xi_l}, & \text{in 3D,} \end{cases} \tag{A.21}$$

siendo Q_{lk}^t definido en (A.18).

A.5 Discusión

En esta sección se presentarán las contribuciones y actividades de investigación llevadas a cabo durante el doctorado. Además, se realizará una breve discusión acerca de las simulaciones realizadas y los resultados obtenidos. Finalmente se describirán las líneas a seguir en el futuro, como el objetivo de continuar desarrollando la herramienta y para así poder abordar un amplio espectro de problemas de FSI.

A.5.1 Conclusiones

En los últimos años se ha puesto un gran esfuerzo en la resolución numérica de problemas multifísicos, en particular la interacción de un fluido con alguna estructura móvil o deformable ha sido de gran importancia práctica y debe ser considerada durante el diseño de muchos sistemas. Con lo cual, es de gran importancia poder realizar la simulación numérica de todo el sistema acoplado, permitiendo así probar una gran cantidad de parámetros de diseño y obtener resultados detallados tanto del fluido como de la estructura.

Por lo tanto, el objetivo general de esta tesis fue generar una herramienta de simulación numérica por medio del desarrollo e implementación de un algoritmo de acople que reutilice códigos existentes en PETSc-FEM, con la intensión de llevar a cabo simulaciones en el área de FSI, teniendo como foco las estabilidad numérica y un alto desempeño de la herramienta resultante. Los códigos existentes en PETSc-FEM fueron acoplados utilizando un algoritmo particionado (Ver sección A.3). Con esta estrategia los sistemas a ser resueltos son menores y mejor condicionados que en el caso monolítico, pero se requiere de una cuidadosa implementación a los fines de evitar una seria degradación de la estabilidad y la precisión. Éstas desventajas fueron superadas con el uso de un predictor estructural, el cual es suficiente para asegurar la estabilidad numérica en problemas de acoplamiento débil. En aquellos casos donde exista un acoplamiento fuerte, se pueden emplear varias etapas por paso de tiempo para así asegurar la estabilidad y precisión de método.

La utilización de una formulación tipo ALE permite el movimiento de la malla durante la simulación, pero son requeridas algunas modificaciones

en el código existente. Debido al cambio de volumen de los elementos en el tiempo se debe satisfacer una ley de conservación extra a los fines de no introducir errores numéricos provenientes del movimiento de la malla. Esta ley en conocida como la ley de conservación geométrica discreta DGCL y en esta tesis se ha desarrollado una nueva y original metodología para obtener esquemas que cumplan con la DGCL sin necesidad de cambiar el integrador temporal. Esta formulación esta basada en el promediado de los jacobianos (AJF) (Ver sección A.4) . Esta metodología asegura el cumplimiento de la DGCL en formulaciones ALE para sistemas generales advectivo-difusivo empleando integradores temporales clásicos y elementos símplices. Los costos adicionados debido a esta nueva metodología son despreciables, ya que solo involucra algunos cambios a nivel de la rutina elemental. Con respecto a los términos de estabilización, los jacobianos advectivos fueron transformados para asegurar que sean invariantes en formulaciones ALE y así obtener la misma solución para un dado problema, sin importar la velocidad de la malla.

Habiendo implementado todo lo referente al algoritmo de acople y a la formulación de jacobianos promediados para cumplir con la DGCL, se llevaron a cabo una serie de validaciones y pruebas sobre los distintos resolvedores, los cuales son la base de las simulaciones de FSI. El solver del fluido ha sido ampliamente utilizado en diferentes trabajos, por lo cual sólo se realiza una validación en estado estacionario. Mientras que para la estructura, se llevan a cabo tanto pruebas estáticas como dinámicas con grandes deformaciones. Luego fue resuelto el problema del pistón con el objetivo de verificar las cuestiones referentes a la conservación de energía en el algoritmo de acople. Este es un problema muy simple desde el punto de vista computacional y permite comprender la transferencia de energía a través de la interfaz fluido/estructura. Además permite verificar la mejora en la estabilidad numérica cuando se emplean predictores estructurales o varias etapas por paso de tiempo.

La metodología de AJF desarrollada en la sección A.4 fue validada mediante la resolución de un conjunto de pruebas numéricas, tanto en 2D como en 3D para diferentes tipos de problemas. Finalmente, el proceso desarrollado durante la ignición de un motor cohete fue analizado empleando el código desarrollado. Se realizó un análisis comparativo de las presiones parietales de varias toberas

con el objetivo de validar el flujo interno. Realizar un cálculo preciso del flujo en la tobera es muy importante ya que la distribución de presiones en la pared tiene un impacto directo en el cómputo de las frecuencias propias del problema acoplado.

Finalmente se dio un primer paso en la resolución de problemas de FSI con fluidos incompresibles, llevándose a cabo la caracterización y simulación de una microvalvula pasiva y de una activa. En el caso de la microvalvula pasiva, la deformación de la membrana se debe a un gradiente de presión, permitiendo así el drenaje del fluido. En el caso de la microvalvula activa la deformación es controlada, a los fines de obtener una dada caída de presión. El uso de técnicas de FSI permite modelar y analizar geometrías 3D complejas, para así obtener un diseño mejorado previo a la fabricación, reduciendo costos y tiempos. Además, al emplear el cálculo en paralelo se reducen significativamente los tiempos de simulación, pasando de días a minutos.

Bibliography

Acheson, D.J.: Elementary Fluid Dynamics. Oxford University Press (1990)

Ahn, H., Kallinderis, Y.: Strongly coupled flow/structure interactions with a geometrically conservative ALE scheme on general hybrid meshes. Journal of Computational Physics **219**, 671--693 (2006)

Aliabadi, S., Ray, S., Tezduyar, T.: Supg finite element computation of viscous compressible flows based on the conservation and entropy variables formulations. Computational Mechanics **11**, 300--312 (1993)

Aliabadi, S., Tezduyar, T.: Space-time finite element computation of compressible flows involving moving boundaries and interfaces. Computer Methods in Applied Mechanics and Engineering **107(1)**, 209--223 (1993)

Artlich, S., Mackens, W.: Newton-coupling of fixed point iterations. Numerical Treatment of Coupled Systems (1995)

Ascher, U.M.: Numerical Methods for Evolutionary Differential Equations. SIAM (2008)

Atkin, R.J., Fox, N.: An Introduction to the Theory of Elasticity. Dover Publications (2005)

Balay, S., Buschelman, K., Gropp, W.D., Kaushik, D., Knepley, M.G., McInnes, L.C., Smith, B.F., Zhang, H.: PETSc Web pag. (2011). URL `http://www.mcs.anl.gov/petsc`

Batchelor, G.K.: An Introduction to Fluid Dynamics. Cambridge, University Press. (1967)

Bathe, K., Zhang, H., Wang, M.: Finite element analysis of incompressible and compressible fluid flows with free surfaces and structural interactions. Computer & Structures **56**(2-3), 193--213 (1995)

Bathe, K.J., Ledezma, G.A.: Benchmark problems for incompressible fluid flows with structural interactions. Computers & Structures **85**, (11--14):628 -- 644 (2007)

Bazilevs, Y., Takizawa, K., Tezduyar, T. (eds.): Special issue on computational fluid mechanics and fluid-structure interaction. Springer Berlin (2011)

Boffi, D., Gastaldi, L.: Stability and geometric conservation laws for ALE formulations. Computer Methods in Applied Mechanics and Engineering **193**, 4717--4739 (2004)

Borland, C.J., Rizzetta, D.P.: Nonlinear transonic flutter analysis. AIAA Journal **20**, 1695--1615 (1982)

Brooks, A., Hughes, T.: Streamline upwind/petrov-galerkin formulations for convection dominated flows with particular emphasis on the incompressible navier-stokes equations. Computer Methods in Applied Mechanics and Engineering **32**, 199--259 (1982)

Bungartz, H.J., Mehl, M., Schäfer, M. (eds.): Fluid-structure Interaction: Modelling, Simulation, Optimization. Springer-Verlag (2006)

Cebral, J.: Loose coupling algorithms for fluid structure interaction. Ph.D. thesis, Institute for Computational Sciences and Informatics, George Mason University (1996)

Codina, R., Cervera, M.: Block-iterative algorithms for nonlinear coupled problems. Advanced Computational Methods in Structural mechanics, CIMNE, Barcelona. pp. 115--134 (1995)

Dadone, A., Grossman, B.: Fast convergence of inviscid fluid dynamic design problems. Computers & Fluids **32:(4)**, 607--627 (2003)

Degroote, J., Bruggeman, P., Haelterman, R., Vierendeels, J.: Stability of a coupling technique for partitioned solvers in fsi applications. Computers & Structures **86**, (23--24):2224--2234 (2008)

Donea, J.: Arbitrary lagrangian-eulerian finite elements method. Computational Methods for Transient Analysis pp. 474--516 (1983)

Donea, J., Huerta, A.: Finite Element Methods for Flow Problems. 1st edition edn. John Wiley and Sons. (2003)

Dooms, D.: Fluid-structure interaction applied to flexible silo constructions. Ph.D. thesis, Departement Burgerlijke Bouwkunde, Katholieke Universiteit Leuven (2009)

Farhat, C., Degand, C., Koobus, B., Lesoinne, M.: Torsional springs for two-dimensional dynamic unstructured fluid meshes. Computer Methods in Applied Mechanics and Engineering **163**, 231--245 (1998)

Farhat, C., Geuzaine, P.: Design and analysis of robust ale time-integrators for the solution of unsteady flow problems on moving grids. Computer Methods in Applied Mechanics and Engineering **193**, 4073--4095 (2004)

Farhat, C., Geuzaine, P., Grandmont, C.: The discrete geometric conservation law and the nonlinear stability of ALE schemes for the solution of flow problems on moving grids. Journal of Computational Physics **174**, 669--694 (2001)

Farhat, C., Lesoinne, M., Maman, N.: Mixed explicit/implicit time integration of coupled aeroelastic problems: Three-field formulation, geometric conservation and distributed solution. International Journal for Numerical Methods in Fluids **21:(10)**, 807--835 (1995)

Farhat, C., Van der Zee, K.G., Geuzaine, P.: Provably second-order time-accurate loosely-coupled solution algorithms for transient nonlinear computational aeroelasticity. Computer Methods in Applied Mechanics and Engineering **195:17-18**, 1973--2001 (2006)

Felippa C.A. Park, K.F.C.: Partitioned analysis of coupled mechanical systems. Computer Methods in Applied Mechanics and Engineering. **190**, 3247--3270 (1999)

Formaggia, L., Nobile, F.: Stability analysis of second-order time accurate schemes for ALE-FEM. Computer Methods in Applied Mechanics and Engineering. **193:39-41**, 4097--4116 (2004)

Franca, L., Frey, S., Hughes, T.: Stabilized finite element methods: I. application to the advective-diffusive. Computer Methods in Applied Mechanics and Engineering **95**, 253--276 (1992)

Förster, C., Wall, W.A., Ramm, E.: Artificial added mass instabilities in sequential staggered coupling of nonlinear structures and incompressible viscous flows. Computer Methods in Applied Mechanics and Engineering **196**, (7):1278--1293 (2007)

Galdi, G.P., Rannacher, R. (eds.): Fundamental Trends in Fluid-Structure Interaction. World Scientific Publishing (2010)

Garelli, L., Paz, R., Castro, H., Storti, M., Dalcin, L.: Computational Fluid Dynamics: Theory, Analysis and Applications, chap. Fluid Structure Interaction and Galilean Invariace, pp. 1--40. Nova Science Publishers (2011)

Garelli, L., Paz, R., Storti, M.: Interacción fluido estructura en flujo compresible en régimen supersónico. In: XVII Congreso sobre Métodos Numéricos y sus Aplicaciones (2008)

Garelli, L., Paz, R., Storti, M.: Geometric conservation law in ALE formulations. In: XVIII Congreso sobre Métodos Numéricos y sus Aplicaciones (2009)

Garelli, L., Paz, R., Storti, M.: Fluid-structure interaction study of the start-up of a rocket engine nozzle. Computers & Fluids **39:7**, 1208--1218 (2010)

Geuzaine, P., Grandmont, C., Farhat, C.: Design and analysis of ale schemes with provable second-order time-accuracy for inviscid and viscous flow simulations. Journal of Computational Physics **191-1**, 206--227 (2003)

Gnesin, V., Rzadkowski, R.: A coupled fluid structure analysis for 3-d inviscid flutter of IV standard configuration. Jornal of Sound and Vibration. **49**, 349--369 (2005)

Guarnieri, F.A.: Implantable ocular microapparatus to ameliorate glaucoma or an ocular overpressure causing disease (2007). URL `http://www.wipo.int/pctdb/en/wo.jsp?WO=2008084350`

Guillard, H., Farhat, C.: On the significance of the geometric conservation law for flow computations on moving meshes. Comput. Methods Appl. Mech. Engrg **190**, 1467--1482 (2000)

Guruswamy, G.P.: Development and applications of a large scale fluids/structures simulation process on clusters. Computers & Fluids **36**, 530--539 (2007)

Hirt, C., Amsden, A., Cook, J.: An Arbitrary Lagrangian-Eulerian computing method for all flow speeds. Journal of Computational Physics **14:3**, 227--253 (1974)

Hron, J., Turek, S.: A monolithic FEM/Multigrid solver for an ALE formulation of fluid-structure interaction with applications in biomechanics. Lecture Notes in Computational Science and Engineering **53**, 146--170 (2006)

Hughes, T.: The Finite Element Methods. Prentice-Hall, inc (1987a)

Hughes, T.: Recent progress in the development and understanding of supg methods with special reference to the compressible euler and navier-stokes equations. International Journal for Numerical Methods in Fluids **7**, 1261--1275 (1987b)

Hughes, T., Liu, W., Zimmermann, T.: Lagrangian-Eulerian finite elements formulations for incompressible viscous flows. In: US-Japan Interdisciplinary Finite Element Analysis. (1978)

Idelsohn, S.R., Del Pin, F., Rossi, R., Oñate, E.: Fluid-structure interaction problems with strong added-mass effect. International Journal for Numerical Methods in Engineering **80(10)**, 1261--1294 (2009)

Idelsohn, S.R., Oñate, E., del Pin, F., Calvo, N.: Fluid-structure interaction using the particle finite element method. Computer Methods in Applied Mechanics and Engineering **195:17-18**, 2100--2123 (2006)

Igra, O., Wang, L., Falcovitz, J., Amann, O.: Simulation of the starting flow in a wedge-like nozzle. Int. J. Shock Waves **8**, 235--242 (1998)

Johnson, A., Tezduyar, T.: Mesh update strategies in parallel finite element computations of flow problems with moving boundaries and interfaces. Computer Methods in Applied Mechanics and Engineering **119**, 73--94 (1994)

Kara, E., Kutlar, A.: Cfd analysis of the ahmed glaucoma valve and design of an alternative device. Computer Methods in Biomechanics and Biomedical Engineering **13(6)**, 655--662 (2010)

Kler, P.A., Berli, C., Guarnieri, F.A.: Modeling and high performance simulation of electrophoretic techniques in microfluidic chips. Microfluidics and Nanofluidics **10(1)**, 187--198 (2010)

Kler, P.A., López, E.J., Dalcín, L.D., Guarnieri, F.A., Storti, M.A.: High performance simulations of electrokinetic flow and transport in microfluidic chips. Computer Methods in Applied Mechanics and Engineering **198(30-32)**, 2360--2367 (2009)

Knupp, P.M.: Achieving finite element mesh quality via optimization of the jacobian matrix norm and associated quantities. part i - a framework for surface mesh optimization. International Journal for Numerical Methods in Engineering **48**, 401--420 (2000)

Koh, H., Kim, J., Park, J.: Fluid-structure interaction analysis of 3-d rectangular tanks with a variationally coupled BEM-FEM and comparison with test results. Earthquake Engng. and Structural Dynamics **27**, 109--124 (1998)

LabBiomens: (2011). URL `http://www.labbiomems.com`

Landau, L., Pitaevskii, L., Lifshitz, E., Kosevich, A.: Theory of Elasticity. Pergamon (1986)

Langhi, F.: Petsc-fem code validation in supersonic/hypersonic flows. Master's thesis, Universidad Nacional de Córdoba (2007)

Lefrancois, E.: Numerical validation of a stability model for a flexible over-expanded rocket nozzle. International Journal for Numerical Methods in Fluids. **49:4**, 349--369 (2005)

Lefrancois, E., Dhatt, G., Vandromme, D.: Fluid-structure interaction with application to rocket engines. International Journal for Numerical Methods in Fluids **30**, 865--895 (1999)

Lesoinne, M., Farhat, C.: Geometric conservation laws for flow problems with moving boundaries and deformable meshes, and their impact on aeroelastic computations. Computer Methods in Applied Mechanics and Engineering **134**, 71--90 (1996)

Lohner, R., Yang, C., Cebral, J., Baum, J., Luo, H., Pelessone, D., Charman, C.: Fluid-structure interaction using a loose coupling algorithm and adaptive unstructured grids. AIAA paper AIAA-98-2419 (1998)

Longatte, E., Bendjeddou, Z., Souli, M.: Application of arbitrary lagrange euler formulations to flow-induced vibration problems. Journal of Pressure Vessel Technology **125**, 411--417 (2003)

Longatte, E., Verreman, V., Souli, M.: Time marching for simulation of fluid-structure interaction problems. Journal of Fluid & Structures **25**, 95--111 (2009)

Lopez, E., Nigro, N., Storti, M., Toth, J.: A minimal element distortion strategy for computational mesh dynamics. International Journal for Numerical Methods in Engineering. **69:9**, 1898--1929 (2007)

Ludeke, H., Calvo, J., Filimon, A.: Fluid structure interaction at the ariane-5 nozzle section by advanced turbulence models. In: Wesseling, P., Onate, E., Periaux, J. (eds.) European Conference on Computational Fluid Dynamics ECCOMAS CFD 2006 (2006)

López, E., Nigro, N., Storti, M., Toth, J.: A minimal element distortion strategy for computational mesh dynamics. International Journal for Numerical Methods in Engineering **69**, 1898--1929 (2007)

López, E.J., Nigro, N.M., Storti, M.A.: Simultaneous untangling and smoothing of moving grids. International Journal for Numerical Methods in Engineering **76(7)**, 994--1019 (2008)

Löhner, R.: Applied CFD Techniques: An Introduction Based on Finite Element Methods. John Wiley & Sons Inc. (2008)

Löhner, R., Yang, C.: Improved ale mesh velocities for moving bodies. Communications in Numerical Methods in Engineering **12**, 599--608 (1996)

Marsden, J., Hughes, T.: Mathematical Foundations of Elasticity. Dover Publications (1983)

Mattiasson, K.: Numerical results from large deflection beam and frame problems analysed by means of elliptic integrals. International journal for numerical methods in engineering **17:(1)**, 145--153 (1981)

Mattingly, J., Ohain, H.V.: Elements of propulsion: gas turbines and rockets. 2nd edn. AIAA (2006)

Mavriplis, D.J., Yang, Z.: Achieving higher-order time accuracy for dynamic unstructured mesh fluid flow simulations: Role of the GCL. 17th AIAA Computational Flow Dynamics Conference pp. 1--16 (2005)

Michler, C., van Brummelen, E.H., Hulshoff, S.J., De Borst, R.: The relevance of conservation for stability and accuracy of the numerical methods for fluid-structure interaction. Comp. Meth. App. Mech. Engng. **192**, 4195--4215 (2003)

Michler, C., Hulshoff, S.J., van Brummelen, E.H., De Borst, R.: A monolithic approach to fluid-structure interaction. Computers & Fluids **33**, 839--848 (2004)

Moríñigo, J., Salvá, J.: Numerical study of the start-up process in an optimized rocket nozzle. Aerospace Science and Technology **12:6**, 485--486 (2008)

Murayama, M., Nakahashi, K., Matsushima, K.: Unstructured dynamic mesh for large movement and deformation. AIAA Paper **0122** (2002)

Nejat, A., Ollivier-Gooch, C.: A high-order accurate unstructured finite volume newton-krylov algorithm for inviscid compressible flows. Journal of Computational Physics **227:(4)**, 2582--2609 (2008)

Newmark, N.M.: A method of computation for structural dynamics. Journal of Engineering Mechanics, ASCE. **85(EM3)**, 67--94 (1959)

Nobile, F.: Numerical approximation of fluid-structure interaction problems with application to haemodynamics. Ph.D. thesis, Department of Mathematics, École Polytechnique Fédérale de Lausanne (2001)

Noh, W.: A time-dependent, two space dimensional, coupled Eulerian-Lagrange code. Methods in Computational Physics. **3**, 117--179 (1964)

Oates, G.: Aerothermodynamics of gas turbine and rocket propulsion. 3rd edn. AIAA (1997)

Ohayon, R., Kvamsdal, T. (eds.): Special issue on Fluid-Structure Interaction. Elsevier (2006)

OpenFOAM: Openfoam (2011). URL `http://www.openfoam.com/`

Park, K., Felippa, C.: A variational principle for the formulation of partitioned structural systems. International Journal for Numerical Methods in Engineering. **47**, 395--418 (2000)

Paz, R.R.: Domain decomposition techniques and parallel programming in computational fluid dynamics. Ph.D. thesis, Universidad Nacional del Litoral (2006)

Paz, R.R., Storti, M., Garelli, L.: Local absorbent boundary condition for nonlinear hyperbolic problems with unknown riemann invariants. Computers & Fluids, **40**, 52--67 (2010)

Pekkari, L.: Aeroelastic stability of supersonic nozzles with separated flow. In: AIAA, SAE, ASME, and ASEE, Joint Propulsion Conference and Exhibit, 29th, Monterey, CA, June 28-30, 1993, 12 p. (1993)

Pekkari, L.: Aeroelastic analysis of side-loads in supersonic nozzles with separated flow. In: AIAA, SAE, ASME, and ASEE, Joint Propulsion Conference and Exhibit (1994)

Piperno, R., Farhat, C.: Partitioned procedures for the transient solution of coupled aeroelastic problems. Part II: energy transfer analysis and three-dimensional applications. Computer Methods in Applied Mechanics and Engineering **190**, 3147--3170 (2001)

Piperno, S.: Simulation numérique de phénomènes d'interaction fluide-structure. Ph.D. thesis, L'ECOLE NATIONALE DES PONTS ET CHAUSSEES (1995)

Piperno, S.: Explicit/implicit fluid/structure staggered procedures with a structural predictor and fluid subcycling for 2d inviscid aeroelastic simulations. International Journal for Numerical Methods in Fluids **25(10)**, 1207--1226 (1997)

Prodromou, P., Hillier, R.: Computation of unsteady nozzle flows. In: Proceedings of the 18th. ISSW, Sendai, Japan, Vol. II (1992)

Rao, S.: Engineering optimization. Wiley and Sons (1996)

Romanelli, G., Serioli, E.: A "free" approach to the modern computational aeroelasticity. Ph.D. thesis, Politecnico di Milano (2008)

Romanelli, G., Serioli, E., Mantegazza, P.: A new accurate compressible inviscid solver for aerodynamic applications. In: 3rd OpenFOAM Workshop by Dipartimento di Energetica, Politecnico di Milano. (2008)

Ryzhakov, P.B., Rossi, R., Idelsohn, S.R., Oñate, E.: A monolithic lagrangian approach for fluid-structure interaction problems. Computational Mechanics **46(6)**, 883--899 (2010)

Ríos Rodriguez, G.A.: Refinamiento h-adaptativo de mallas no estructuradas en problemas estacionarios y transitorios de flujos compresibles. Ph.D. thesis, Universidad Nacional del Litoral (2009)

Sassetti, F., Guarnieri, F.A., Garelli, L., Storti, M.: Characterization and simulation of an active microvalve for glaucoma. Computer Methods in Biomechanics and Biomedical Engineering. **In press** (2011)

Shankar, V., Ide, H.: Aeroelastic computation of flexible configuration. Computers & Structures **30**, 15--28 (1988)

Shashi Bhushan Verma Ralf Stark, a.O.H.: Relation between shock unsteadiness and the origin of side-loads inside a thrust optimized parabolic rocket nozzle. Aerospace Science and Technology **10:6**, 474--483 (2006)

Stay, M., Pan, T., Brown, J., Ziaie, B., Barocas, V.: Thin-film coupled fluid-solid analysis of flow through the ahmed glaucoma drainage device. J. Biomech. Eng. **127(5)**, 776--781 (2005)

Stein, K., Tezduyar, T., Benney, R.: Automatic mesh update with the solid-extension mesh moving technique. Comput. Meth. Appl. Mech. Engrg. **192**, 2019--2032 (2004)

Storti, M., Garelli, L., Paz, R.R.: A finite element formulation satisfying the discrete geometric conservation law based on averaged jacobians. International Journal for Numerical Methods in Fluids **In press** (2011)

Storti, M., Nigro, N., Paz, R.: Dynamic boundary conditions in Computational Fluid Dynamics. Computer Methods in Applied Mechanics and Engineering **197(13-16)**, 1219--1232 (2008)

Storti, M., Nigro, N., Paz, R., Dalcin, L., Lopez, E.: Petsc-fem: A general purpose, parallel, multi-physics FEM program (1999-2010). http://www.cimec.org.ar/petscfem (2010). URL `http://www.cimec.org.ar/twiki/bin/view/Cimec/PETScFEM`

Storti, M., Nigro, N., Paz, R., Dalcín, D.: Strong coupling strategy for fluid structure interaction problems in supersonic regime via fixed point iteration. Journal of Sound and Vibration **30**, 859--877 (2009)

Storti, M., Nigro, N., Paz, R., Dalcín, L., Ríos Rodríguez, G., López, E.: Fluid structure interaction with a staged algorithm. In: XV Congreso sobre Métodos Numéricos y sus Aplicaciones, Santa Fe, Argentina, Mecánica Computacional, Vol. XXV, 887--905 (2006)

Sutton, G., Biblarz, O.: Rocket propulsion elements. 7th edn. John Wiley and Sons (2001)

Tang, C., Hafez, M.: Numerical simulation of steady compressible flows using a zonal formulation. part i: inviscid flows. Computers & Fluids **30:(7-8)**, 989--1001 (2001)

Taro Shimizu, M.K., Tsuboi, N.: Internal and external flow of rocket nozzle. Journal of the Earth Simulator **9**, 19--26 (2008)

Tezduyar, T.: Finite element methods for flow problems with moving boundaries and interfaces. Archives of Computational Methods in Engineering **08**(2) (2001)

Tezduyar, T., Osawa, Y.: Finite element stabilization parameters computed from element matrices and vectors. Computer Methods in Applied Mechanics and Engineering **190:3-4**, 411--430 (2000)

Tezduyar, T., Sathe, S.: Stabilization parameters in supg and pspg formulations. Journal of Computational and Applied Mechanics **4**, 71--88 (2003)

Tezduyar, T., Sathe, S., Keedy, R., Stein, K.: Space-time finite element techniques for computation of fluid-structure interactions. Computer Methods in Applied Mechanics and Engineering **195:17-18**, 2002--2027 (2006)

Tezduyar, T., Schwaab, M., Sathe, S.: Sequentially-coupled arterial fluid-structure interaction (SCAFSI) technique. Computers & Structures **198:45-46**, 3524--3533 (2009)

Tezduyar, T., Senga, M.: Determination of the shock-capturing parameters in supg formulation of compressible flows. In: Springler-Verlag, T.U.P.. (ed.) Computational Mechanics WCCM IV, Beijing, China 2004. (2004)

Tezduyar, T., Senga, M.: Stabilization and shock-capturing parameters in supg formulation of compressible flows. Computer Methods in Applied Mechanics and Engineering **195**, 1621--1632 (2006)

Tezduyar, T.E., Sathe, S., Schwaab, M., Conklin, B.S.: Arterial fluid mechanics modeling with the stabilized space-time fluid-structure interaction technique. International Journal for Numerical Methods in Fluids **57:7**, 601--609 (2008)

Thomas, P., Lombard, C.: Geometric conservation law and its applications to flow computations on moving grids. AIAA **17**, 1030--1037 (1979)

Timoshenko, S.P.: Theory of Elasticity. McGraw-Hill (1970)

Trepanier, J., Reggio, M., Zhang, H., Camarero, R.: A finite-volume method for the Euler equations on arbitrary Lagrangian-Eulerian grids. Computers and fluids. **20:4**, 399--409 (1991)

Tuković, v., Jasak, H.: Updated lagrangian finite volume solver for large deformation dynamic response of elastic body. Transactions of FAMENA **31:(1)**, 55--70 (2007)

Tuner, M.: Rockets and spacecraft propulsion. 2nd edn. Springer (2006)

Wang, T.S.: Transient three dimensional analysis of side load in liquid rocket engine nozzle. AIAA p. 3681 (2004)

Xu, Z., Accorsi, M.: Finite element mesh update methods for fluid-structure interaction simulations. Finite Elements in Analysis and Design **40:9-10**, 1259--1269 (2004)

Yang, Z., Mavriplis, D.J.: Unstructured dynamic meshes with higher-order time integration schemes for the unsteady Navier-Stokes equations. In: AIAA 2005-1222 (2005)

Zienkiewicz, O., Taylor, R.: The Finite Element Method for Solid and Structural Mechanics. Butterworth-Heinemann (2005)

Étienne, S., Garon, A., Pelletier, D.: Perspective on the geometric conservation law and finite element methods for ALE simulations of incompressible flow. Journal of Computational Physics **228:7**, 2313--2333 (2009)

Östlund, J.: Flow processes in rocket engine nozzle whit focus on flow separation and side-loads. Licentiate Thesis, Royal Institute of Technology (2002)

Östlund, J.: Side-load phenomena in highly overexpanded rocket nozzles. Journal of Propulsion and Power **20:2** (2004)

Doctorado en Ingeniería
mención mecánica computacional

Título de la obra:

Fluid Structure Interaction using an Arbitrary Lagrangian Eulerian Formulation

Autor: Luciano Garelli

Lugar: Santa Fe, Argentina

Palabras Claves:

Fluid Structure Interaction, ALE Formulation,
Geometric Conservation Law, Numerical Simulation,
Finite Element Method, Coupling Algorithm